

Promoting Molybdenum Carbide for Biofuels Upgrading

by

Sarah Wendy Paleg

A dissertation submitted in partial fulfillment
of the requirements for the degree of
Doctor of Philosophy
(Chemical Engineering)
in the University of Michigan
2019

Doctoral Committee:

Professor Levi T. Thompson, Chair
Professor Mark Barteau, Texas A&M University
Professor Johannes Schwank
Professor Angela Violi

Sarah W. Paleg

psarah@umich.edu

ORCID iD: 0000-0002-0844-9625

© Sarah W. Paleg 2019

Dedication

To my mom and my grandpa Walter, whose own doctorates inspired me.

Acknowledgements

Thank you to my advisor, Dr. Levi T. Thompson, who has mentored and guided me through my pursuit of this doctorate. I would also like to thank my dissertation committee – Professor Mark Barteau, Professor Johannes Schwank, and Professor Angela Violi – for their helpful comments and insight.

I would also like to express my appreciation for the support of the wonderful Thompson research group members who were by my side throughout my Ph. D. research. In particular, I would like to thank Dr. Yuan Chen, Dr. Brian Wyvrat, Dr. Tanya Breault, and Dr. Jason Gaudet, who welcomed me to the lab when I first joined and showed me the ropes. They coached me on performing fundamental synthesis and characterization techniques, and each demonstrated a robust passion for research that helped carry me through this doctoral experience. I would also like to thank the high school, undergraduate, and master's students who have worked with and helped me: Digna Vora, Gqwetha Ncube, and Jordan Jones.

Beyond my own research group, I am grateful to have worked with a great team of collaborators at the National Renewable Energy Laboratory (NREL). Dr. Josh Schaidle, himself an alumnus of Dr. Thompson's research group, has been a great mentor since I first interned with him at NREL in the summer of 2012. I feel very lucky that he continued to support and engage with my research during my Ph. D. Many thanks also to Connor P. Nash, who has been a great partner in this work.

I would also like to express supreme gratitude for the fellowships that have supported me and my work throughout this endeavor, the Rackham Merit Fellowship, National Science Foundation Graduate Research Fellowship, and the University of Michigan Dow Doctoral Fellowship. I would like to acknowledge the additional funding source that supported my work, the Department of Energy via the National Renewable Energy Laboratory (Contract DE-AC36-08GO28308).

Last, I would like to thank my family and my partner, Brad, for being such a source of love and strength throughout graduate school. My parents have set an unbeatable example of how to pursue a life of integrity and passion, and I so hope to follow their lead. My sister, a fountain of empathy and compassion, inspires me to put more positivity out into the world, which in turn makes me a better person. And my partner, Brad, makes life more fun to live because we get to do it together. I love you all so much.

Table of Contents

Dedication	ii
Acknowledgements	iii
List of Tables	ix
List of Figures.....	xi
Abstract.....	xv
CHAPTER 1 Introduction	1
1.1. Motivation	1
1.2. Biomass, bio-oil, and biofuel.....	4
1.3. Biofuel and model compound upgrading	10
1.4. Molybdenum carbide catalyst.....	13
1.5. Promoters for molybdenum carbide catalysts	16
1.6. Research goals and organization of the text	19
1.7. References	22
CHAPTER 2 Metal/Mo₂C catalysts for crotonaldehyde upgrading.....	29
2.1. Introduction	29
2.2. Experimental Methods.....	32
2.2.1 Catalyst Synthesis	32

2.2.2	Physical Catalyst Characterization.....	34
2.2.3	Activity and Selectivity Measurements.....	35
2.3.	Results	37
2.3.1	Physical Catalyst Characterization.....	37
2.3.2	Activity.....	38
2.3.3	Selectivity.....	45
2.4.	Discussion	48
2.5.	Summary	51
2.6.	References	52

CHAPTER 3 Selectivity of biomass model compound upgrading over K-promoted Mo₂C.....56

3.1.	Introduction	56
3.2.	Experimental Methods.....	57
3.2.1	Catalyst Synthesis	57
3.2.2	Physical Catalyst Characterization.....	58
3.2.3	Activity and Selectivity Measurements.....	58
3.3.	Results	60
3.3.1	Physical Catalyst Characterization.....	60
3.3.2	Activity.....	64
3.3.3	Selectivity.....	69
3.4.	Discussion	77
3.5.	Summary	80
3.6.	References	80

CHAPTER 4 Pathway of selectivity influence for transition versus alkali metals84

4.1.	Introduction	84
4.2.	Experimental Methods.....	88
4.2.1	Catalyst Synthesis	88
4.2.2	Catalyst Characterization	88
4.3.	Results	90
4.3.1	Evaluating TPD Dimensionless Numbers.....	90
4.3.2	Active Site Concentration Measurements	93
4.3.3	Linking Active Sites Concentrations to Selectivity	100
4.4.	Discussion	102
4.5.	Summary	108
4.6.	References	108

CHAPTER 5 Pathway of selectivity influence for transition versus alkali metals..113

5.1.	Introduction	113
5.2.	Experimental Methods.....	115
5.2.1	Catalyst Synthesis	115
5.2.2	Catalyst Characterization	116
5.3.	Results	116
5.3.1	Physical Catalyst Characterization.....	116
5.3.2	Active Site Concentrations.....	119
5.3.3	Activity.....	125
5.3.4	Selectivity.....	127
5.3.5	Linking Active Sites and Productivity	130
5.4.	Discussion	136
5.5.	Summary	141
5.6.	References	141

CHAPTER 6 Summary and Future Work.....	144
6.1. Summary and Conclusions	144
6.2. Future Work in Current Research Areas	146
6.3. Research Thrusts in New Areas	148
6.4. References	149

List of Tables

Table 1.1. Elemental composition and water content ranges of crude petroleum oils compared to pyrolysis bio-oils.....	9
Table 2.1. Target and measured metal loadings, and surface areas of catalysts.....	38
Table 2.2. Nonlinear regression models for catalyst activity decay.	42
Table 2.3. Results from nonlinear regression of activity data to four empirical decay rate laws.	43
Table 2.4. BET surface areas and apparent activation energies of Mo ₂ C catalysts.....	43
Table 2.5. Possible primary and secondary reaction pathways of crotonaldehyde.	46
Table 3.1. Reitveld refinement results for Mo ₂ C-based catalysts.....	63
Table 3.2. Measured metal content and surface area for all catalysts.....	63
Table 3.3. Regression results and R ² for GPL model fits for the deactivation data of acetic acid upgrading with Mo ₂ C-based catalysts.	65
Table 3.4. Regression results and R ² for GPL model fits for the deactivation data of crotonaldehyde upgrading with Mo ₂ C-based catalysts.....	65
Table 3.5. Consumption rates and conversions for acetic acid conversion at 350 °C and 3 h TOS for all catalysts.....	67
Table 3.6. Consumption rates and conversions of crotonaldehyde upgrading at 350 °C and 6 h TOS for all catalysts.....	67
Table 3.7. Possible primary and secondary reaction pathways of acetic acid.	70
Table 3.8. Carbon selectivities (%) for acetic acid conversion at 350 °C and 3 h TOS for all catalysts.....	71
Table 3.9. Carbon selectivities (%) of crotonaldehyde upgrading at 350 °C and 6 h TOS for all catalysts.	74
Table 4.1. Parameters used to analyze dimensionless parameters associated with temperature-programmed desorption, and their associated values for the experiments described in this work.	91
Table 4.2. Dimensionless numbers associated with temperature-programmed desorption, based on [1].....	92

Table 4.3. Residual RMS of recorded TPD vs the deconvolution pattern. RMSE% is a scale-independent error from residual RMS divided by the maximum value.	95
Table 4.4. Base and acid site concentrations for each deconvoluted peak.	95
Table 4.5. Base, acid, and H* site concentrations for the various catalysts.	98
Table 4.6. Ratios of catalyst active site concentrations.	98
Table 4.7. Correlations between productivity of each product and acid, H*, and base site concentrations for Mo ₂ C and K/Mo ₂ C catalysts.	102
Table 5.1 BET Surface area and DFT pore volumes for all catalysts.....	118
Table 5.2. Peak location (°C) of deconvoluted peaks for Fe/Mo ₂ C catalysts, and the correlation coefficient of the peak locations and the ML of Fe.	122
Table 5.3. Site concentrations of the deconvoluted base site types for the Fe/Mo ₂ C catalysts.	122
Table 5.4. Results from nonlinear regression of activity data to four empirical decay rate laws.	126
Table 5.5. Crotonaldehyde consumption rate and conversions for the Mo ₂ C and Fe/Mo ₂ C catalysts after 9 hr TOS at 350 °C.	127
Table 5.6. Correlations between rate of productivity of each product and site concentrations for Mo ₂ C and Fe/Mo ₂ C catalysts.	135
Table 5.7 Spread of active site type concentrations.	140

List of Figures

Figure 1.1 Annual global carbon emission changes over time [6].	2
Figure 1.2 Atmospheric CO ₂ emissions over the past 400 millennia by direct measurement (–) and ice core reconstruction (–).....	3
Figure 1.3. Bubbling fluid bed reactor with electrostatic precipitator [14].	8
Figure 1.4. Composition ranges of pyrolysis bio-oil oxygenate functionalities correlated according to their lignocellulosic biomass source. The weight ranges are based on bio-oil analysis data reported by Milne et al [16,19].....	10
Figure 1.5. Crystal structure of fcc α -MoC _{1-x} (left) and hexagonal β -Mo ₂ C (right).....	13
Figure 1.6. Selectivity of propanal with H ₂ over Mo ₂ C.....	15
Figure 1.7. Selectivity of guaiacol deoxygenation over metal-modified Mo ₂ C catalysts.	18
Figure 2.1. X-ray diffraction spectra of metal/Mo ₂ C and Mo ₂ C catalysts.....	38
Figure 2.2. Activity decay for crotonaldehyde conversion during initial time on stream for Mo ₂ C (•), Rh/Mo ₂ C (•), Co/Mo ₂ C (•), Pd/Mo ₂ C (•), Fe/Mo ₂ C (•), Cu/Mo ₂ C (•), Ni/Mo ₂ C (•), and K/Mo ₂ C (•).	41
Figure 2.3. Activity $a(t)$ data for Mo ₂ C (•) as a function of time on stream with line regression results for linear (–), exponential (–), hyperbolic (–), and reciprocal decay models (–).	41
Figure 2.4. Arrhenius plot for crotonaldehyde conversion of Mo ₂ C (•), Rh/Mo ₂ C (•), Co/Mo ₂ C (•), Pd/Mo ₂ C (•), Fe/Mo ₂ C (•), Cu/Mo ₂ C (•), Ni/Mo ₂ C (•), and K/Mo ₂ C (•). All conversion rates are normalized by catalyst surface areas.....	44
Figure 2.5. Arrhenius plot for crotonaldehyde conversion of Rh/Mo ₂ C (•), Co/Mo ₂ C (•), Pd/Mo ₂ C (•), Fe/Mo ₂ C (•), Cu/Mo ₂ C (•), Ni/Mo ₂ C (•), and K/Mo ₂ C (•). All conversion rates are normalized by moles of metal promoter on catalyst surface.	45
Figure 2.6. Crotonaldehyde conversion (■) and carbon selectivity of butyraldehyde, butene, 3-butenal, and butadiene for Mo ₂ C during deactivation period at 350 °C.	47
Figure 2.7. Carbon selectivity for ■butadiene, ■butene, ■butyraldehyde, and ■3-butenal, products from crotonaldehyde conversion at 350°C after 6 hr TOS on Mo ₂ C catalysts.....	48

Figure 3.1. X-ray diffraction patterns for (a) K(1.1ML)/Mo ₂ C, (b) K(0.7ML)/Mo ₂ C, (c) K(0.5ML)/Mo ₂ C, (d) K(0.3ML)/Mo ₂ C, (e) K(0.1ML)/Mo ₂ C, and (f) Mo ₂ C catalysts and peak positions for polycrystalline (g) orthorhombic β-Mo ₂ C (JCPDF 00035-0787) and (h) cubic α-MoC _{1-x} (JCPDF 00-015-0457).....	61
Figure 3.2. DFT pore volume distribution for Mo ₂ C (–), K(0.1ML)/Mo ₂ C (–), K(0.3ML)/Mo ₂ C (–), K(0.5ML)/Mo ₂ C (–), K(0.7ML)/Mo ₂ C (–), and K(1.1ML)/Mo ₂ C	63
Figure 3.3. Arrhenius plot with crotonaldehyde consumption rate normalized by surface area (top) and by weight of Mo ₂ C (bottom) of Mo ₂ C (•), K(0.1ML)/Mo ₂ C (•), K(0.3ML)/Mo ₂ C (•), K(0.5ML)/Mo ₂ C (•), K(0.7ML)/Mo ₂ C (•), and K(1.1ML)/Mo ₂ C (•).	68
Figure 3.4. Carbon selectivities (%) of AA upgrading for acetone (•), CO (•), acetaldehyde (•), and CO ₂ (•) at 350 °C with increasing K coverage of Mo ₂ C catalyst. Data were taken at 6 h time on stream. Error bars represent 95% confidence interval. ...	72
Figure 3.5. Molar productivity from acetic acid conversion of acetone (•), CO ₂ (•), acetaldehyde (•), and ethylene (•) at 350 °C with increasing K coverage of Mo ₂ C catalyst and (○) carbon balance. Data were taken at 6 h. Error bars represent 95% confidence interval.	72
Figure 3.6. TOS carbon selectivity and conversion of (a) Mo ₂ C and (b) K(1.1ML)/Mo ₂ C for acetic acid upgrading for acetone (•), CO ₂ (•), acetaldehyde (•), ethylene (•), and other (•). Error bars represent 95% confidence interval, based on the determined standard error of ±4%.....	73
Figure 3.7. Carbon selectivities (%) crotonaldehyde for 3-butenal (•), butyraldehyde (•), butenes (•), and butadiene (•) at 350 °C with increasing K coverage of Mo ₂ C catalyst. Data were taken at 6 h time on stream. Error bars represent 95% confidence interval. ...	75
Figure 3.8. Molar productivity from crotonaldehyde conversion of 3-butenal (•), butyraldehyde (•), butene (•), and butadiene (•) at 350 °C with increasing K coverage of Mo ₂ C catalyst and (○) carbon balance. Data were taken at 6 h. Error bars represent 95% confidence interval.....	75
Figure 3.9. TOS carbon selectivity of (c) Mo ₂ C and (d) K(1.1ML)/Mo ₂ C for crotonaldehyde upgrading for 3-butenal (•), butyraldehyde (•), butene (•), and butadiene (•). Error bars represent 95% confidence interval, based on the determined standard error of ±4%.....	76
Figure 4.1. CO ₂ -TPD (left) and NH ₃ -TPD (right) profiles of (a) MgO, (b) Mo ₂ C, (c) K(0.1ML)/ Mo ₂ C, (d) K(0.3ML)/ Mo ₂ C, (e) K(0.5ML)/Mo ₂ C Mo ₂ C (f) K(0.7ML)/ Mo ₂ C, and (g) K(1.1ML)/ Mo ₂ C catalysts where M.S. signal has been normalized by the surface area of the catalysts. Peak maxima temperatures are listed for strong and weak deconvoluted peaks for each TPD. Dash lines represent peak maxima temperature of deconvoluted peaks for Mo ₂ C.....	93
Figure 4.2. Deconvolution of CO ₂ -TPD (left) and NH ₃ -TPD profiles (right) of (a) MgO, (b) and (h) Mo ₂ C, (c) and (i) K(0.1ML)/Mo ₂ C, (d) and (j) K(0.4ML)/ Mo ₂ C, (e) and (k)	

K(0.5ML)/ Mo ₂ C, (f) and (l) K(0.7ML)/ Mo ₂ C, and (g) and (m) K(1.1ML)/ Mo ₂ C catalysts. Deconvoluted peaks (peak maxima are noted in °C with corresponding colors, and dashed lines represent the peak maxima of Mo ₂ C), background, and residual (difference between raw spectrum and fit) are shown for all the Mo ₂ C catalysts. The M.S. signal has been scaled so that the profiles are of the same height for ease of viewing (scaling factors are listed below figure labels).	97
Figure 4.3. Site concentrations of base (•), acid (•), and H* sites (•) on the surface of Mo ₂ C catalysts with increasing K coverage. Error bars represent 95% confidence interval.	99
Figure 4.4. H ₂ -TPD profiles of (a) Mo ₂ C, (b) K(0.1ML)/Mo ₂ C, (c) K(0.3ML)/Mo ₂ C, (d) K(0.5ML)/Mo ₂ C, (e) K(0.7ML)/Mo ₂ C, and (f) K(1.1ML)/Mo ₂ C catalysts where TCD signal has been normalized by the surface area of the catalysts. Dashed line marks the temperature of the peak maximum for Mo ₂ C. Some spectra have been scaled for ease of viewing; scaling factor is noted on the figure.	100
Figure 4.5. Correlations between site concentration of weak base (○), strong base (•), weak acid (○), strong acid (•), and H* sites (■) with the 3-butenal productivity.	101
Figure 4.6. Proposed reaction pathway for crotonaldehyde upgrading.	108
Figure 5.1. X-ray diffraction patterns for (a) Fe(1.1ML)/Mo ₂ C, (b) Fe(0.7ML)/Mo ₂ C, (c) Fe(0.5ML)/Mo ₂ C, (d) Fe(0.1ML)/Mo ₂ C, and (e) Mo ₂ C catalysts and peak positions for polycrystalline (f) orthorhombic β-Mo ₂ C (JCPDF 00035-0787) and (g) cubic α-MoC _{1-x} (JCPDF 00-015-0457).....	117
Figure 5.2. DFT pore volume distribution for Mo ₂ C (–), Fe(0.1ML)/Mo ₂ C (–), Fe(0.5ML)/Mo ₂ C (–), Fe(0.7ML)/Mo ₂ C (–), and Fe(1.1ML)/Mo ₂ C (–).....	118
Figure 5.3. Site concentrations of base (•) and acid sites (•) on the surface of Mo ₂ C catalysts with increasing Fe coverage. Error bars represent 95% confidence interval... ..	119
Figure 5.5. NH ₃ -TPD profiles of (a) Mo ₂ C, (b) Fe(0.1ML)/Mo ₂ C, (c) Fe(0.5ML)/Mo ₂ C Mo ₂ C (d) Fe(0.7ML)/Mo ₂ C, and (e) Fe(1.1ML)/Mo ₂ C catalysts where M.S. signal has been normalized by the surface area of the catalysts.	120
Figure 5.5. CO ₂ -TPD profiles of (a) Mo ₂ C, (b) Fe(0.1ML)/Mo ₂ C, (c) Fe(0.5ML)/Mo ₂ C Mo ₂ C (d) Fe(0.7ML)/Mo ₂ C, and (e) Fe(1.1ML)/Mo ₂ C catalysts where M.S. signal has been normalized by the surface area of the catalysts.	120
Figure 5.6. Site concentrations of weak (•), medium (•), strong (•), and total (•) base sites on the surface of Mo ₂ C catalysts with increasing Fe coverage. Error bars represent 95% confidence interval.....	123
Figure 5.7. Deconvoluted CO ₂ -TPD profiles of (a) Mo ₂ C, (b) Fe(0.1ML)/Mo ₂ C, (c) Fe(0.5ML)/Mo ₂ C (d) Fe(0.7ML)/Mo ₂ C, and (e) Fe(1.1ML)/Mo ₂ C catalysts. Deconvoluted peaks are shown in green, red, and blue, and residuals (difference between raw spectrum and fit) are displayed below each TPD. The M.S. signals have been scaled so that the profiles are of the same height for ease of viewing. Dashed lines represent the peak maxima of Mo ₂ C).....	124

Figure 5.8. Catalyst deactivation profiles for Mo ₂ C (-), Fe(0.1ML)/Mo ₂ C (-), Fe(0.5ML)/Mo ₂ C (-), Fe(0.7ML)/Mo ₂ C (-), and Fe(1.1ML)/Mo ₂ C (-).....	126
Figure 5.9. Carbon productivity for Mo ₂ C and Fe/Mo ₂ C catalysts at 350 °C after 9 hr TOS.....	128
Figure 5.10. Carbon selectivity for Mo ₂ C and Fe/Mo ₂ C catalysts at 350 °C after 9 hr TOS.....	129
Figure 5.11. Correlation plot between product productivity and weak, medium-strength, strong base sites and acid sites over Mo ₂ C and Fe/Mo ₂ C catalysts.....	131
Figure 5.12. Correlation plot between product productivity and weak, medium-strength, strong base sites and acid sites over Mo ₂ C and Fe/Mo ₂ C catalysts.....	132
Figure 5.13. Correlation plot between product productivity and weak, medium-strength, strong base sites and acid sites over Mo ₂ C and Fe/Mo ₂ C catalysts.....	133
Figure 5.14. Correlation plot between product productivity and weak, medium-strength, strong base sites and acid sites over Mo ₂ C and Fe/Mo ₂ C catalysts.....	134

Abstract

Pyrolysis biofuels are an attractive near-term solution for reducing carbon emissions from vehicles including automobiles and jets while still being compatible with current engine technology. However, in order to be used as a “drop-in” fuel, bio-oil must be upgraded into biofuel by removing oxygen, increasing hydrocarbon chain lengths, and increasing energy density. Current catalytic processes rely on expensive noble metal catalysts, and/or are not sufficiently selective in their upgrading. Molybdenum carbide (Mo_2C) is a low-cost, high surface area catalyst that is known to be active for hydrogenation and other relevant reactions and was identified as a promising candidate for use as a bio-oil upgrading catalyst. The research undertaken in this dissertation aims to investigate methods to control the activity and selectivity of the Mo_2C catalyst through adding promoter metals to the surface of the Mo_2C catalyst. Model compounds were selected to represent important properties of bio-oil; both acetic acid and crotonaldehyde were used as model compounds. Fe, Co, Ni, Cu, Ru, Rh, Pd, and K were screened as metal promoters of crotonaldehyde conversion. Rh, Pd, and Co did not significantly affect catalyst activity or selectivity. Ni, Cu, and K increased the selectivity to the isomerization product, while Fe increased the selectivity to the HDO products. K showed the highest selectivity to isomerization product, so it was selected for further study. A series of catalysts with increasing amounts of K promotion up to 1.1 equivalent monolayers on Mo_2C were

synthesized via incipient wetness and tested for their activity and selectivity in acetic acid and crotonaldehyde conversion. K promotion increased selectivity to ketonization and isomerization products, respectively, and reached a maximum effect at 0.5ML. Similarly, K increased base site concentration on the Mo₂C surface, and the change in base site concentration as found to correlate with the ketonization and isomerization products' productivities. Consequently, the base site, thought to be an exposed negatively charged C atom or an Mo-O species, was proposed as the active site for dominant product formation on Mo₂C. Additionally, K promotion was found to be an effective tool to control the base site density.

In initial screening, Fe showed highest selectivity to HDO products, so it was selected for further study and to compare with K promotion. A series of catalysts with increasing amounts of Fe promotion up to 1.1 equivalent monolayers on Mo₂C were synthesized via incipient wetness (because it allowed to higher Fe promotion) and tested for their activity and selectivity in crotonaldehyde conversion. Fe promotion was found to decrease both acid and base site concentrations with more than 0.5ML of Fe, as well as crotonaldehyde conversion rates. Productivity of much products decreased, but correlations between active site concentrations and productivities showed which active site types were most predictive of a given product. The weak base site concentration was found to be predictive of (correlate with) productivity of butenes and butyraldehyde, and strong base site concentration was predicative of C₈+ products. Though K and Fe promotion had opposite effects on the base site concentration, both sets of catalysts revealed that base sites were predictive of productivity of particular products. Overall, the contribution of this dissertation is that has shown how promoters (specifically, K and Fe) can be employed to

manipulate active site concentration on Mo₂C support to control selectivity of bio-oil model compound upgrading.

CHAPTER 1

Introduction

1.1. Motivation

Quality of life has increased dramatically over the past two centuries on a global scale, as measured by changes in GDP, adult literacy rate, and life expectancy; world GDP is estimated to have increased almost 18-fold from 1820 to 2015 [1], global adult literacy rate is estimated to have increase more than 7 times between 1800 and 2016 [2,3], and the highest reported life expectancy in any national population almost doubled between 1840 and 2010 [4]. These three indicators are used by the United Nations to estimate quality of life via their Human Development Index (HDI). At the same time, the United Nations estimated that the global population increased more than six times over between 1800 and 2000, from under one billion to just over six billion people [5]. During that time, the world's energy demands have, correspondingly, increased exponentially. Since virtually all the world's energy demands are met by fossil fuels, annual global carbon emissions have increased at an exponential rate, as shown in Figure 1.1.

Debate is ongoing regarding whether energy use is a cause of, or caused by, increased wellbeing and quality of life. Some scholars have theorized that increases in the quality of life were a direct consequence of the invention and adoption of energy-intensive technologies including steam engines, internal combustion engines, and electrical generators [6]. However, more recent analysis has shown that for industrial nations over

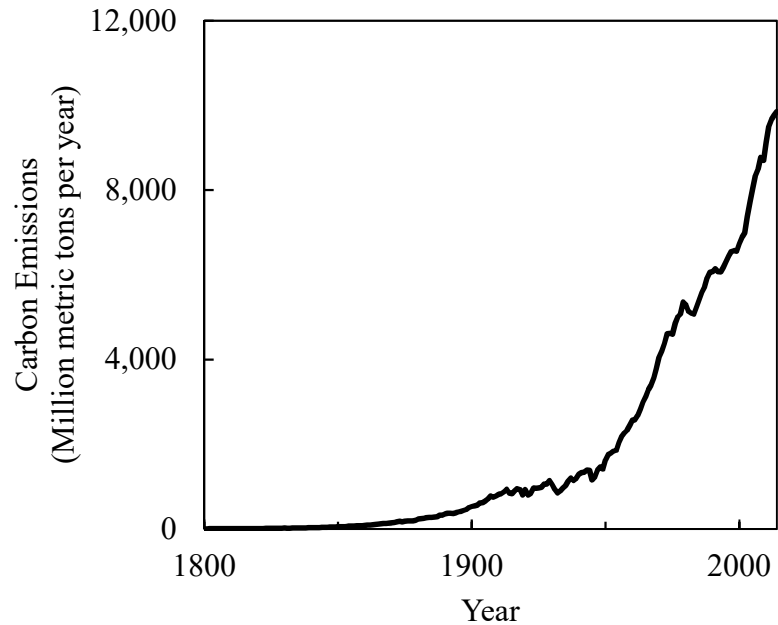


Figure 1.1 Annual global carbon emission changes over time [6].

the time period 1980 to 2006, increases in energy consumption per capita did not have a statistically significant correlation with increases to that nation's GDP per capita [7]. It may be that energy consumption aided, and aids, in improving quality of life as countries undergo drastic modernization of their economies, but that there are more marginal or no return on energy use in terms of quality of life improvements once an industrial economy is established.

Either way, despite the earth's natural carbon cycle having some carbon sinks, the emission of carbon has far outstripped the ability of the carbon sinks to manage (steady) the concentration of CO₂ and other greenhouse gases in our atmosphere. This can be seen in the rise of atmospheric CO₂ concentration since the onset of industrialization as shown in Figure 1.2. Human greenhouse gas emissions have been shown to be the cause of the increase in the CO₂ concentration [8]. The rise in atmospheric CO₂ concentrations has

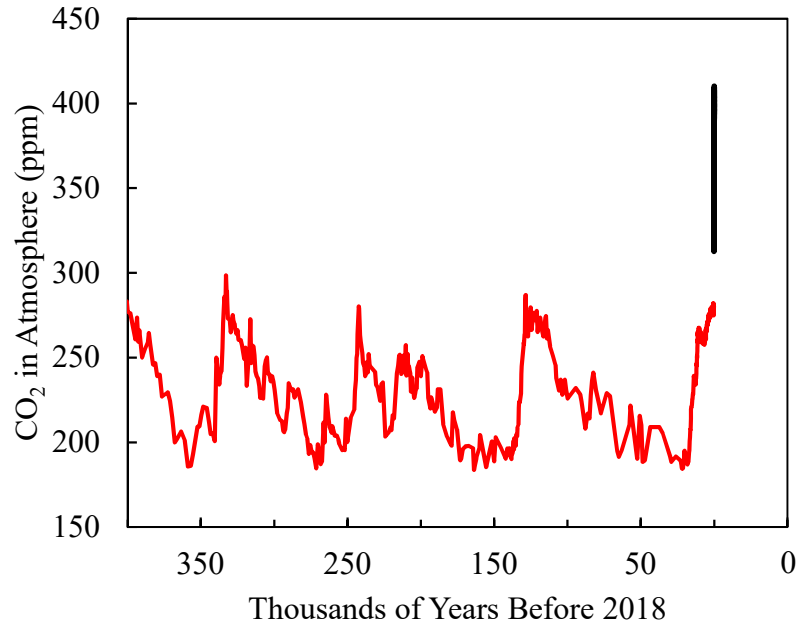


Figure 1.2. Atmospheric CO₂ emissions over the past 400 millennia by direct measurement (—) and ice core reconstruction (—).

induced the greenhouse effect, which has and will continue to wreak havoc on our planet via global climate change. Climate change will lead to increases in global temperatures, the frequency of natural disasters, sea levels, and more [9]. Consequently, our society needs immediate- and long-term plans to reduce the concentration of carbon in the atmosphere; first by dramatically reducing carbon emissions, and perhaps eventually by capturing and sequestering existing carbon in the atmosphere.

In the near-term, this functionally means that we have an imperative to decarbonize our society. One option is to reduce or stop using energy-intensive and carbon-intensive technologies, including electricity and gasoline-powered transportation, which accounted for 25 and 14%, respectively, of global greenhouse gas emissions in 2010 [10]. Another option is to find ways to decarbonize while maintaining the high quality of life that people

have come to expect. For example, developing low- or zero-carbon replacements for products already in use. In the realm of transportation, “drop-in” fuels refers to renewable, low-carbon fuels that can replace gasoline in current engine technologies such that they can “be added into the existing fuel infrastructure without any changes” [11]. Drop-in fuels fall under the broader category of “biofuels”, which is defined in the following section.

The research undertaken in this dissertation was done with the goal of contributing to the body of knowledge surrounding the upgrading of drop-in biofuels, so that they may be expediently brought to market to contribute to a decrease in global CO₂ emissions, and hopefully a slowing or reversal in the rate of increase of the atmospheric CO₂ concentration.

1.2. Biomass, bio-oil, and biofuel

Biofuel – or fuel made from living matter – production starts with its feedstock: biomass. Ultimately, biomass derives its energy from the sun. Photosynthesis converts light energy into chemical energy by producing carbohydrate molecules from water and CO₂, which release O₂ in the process. Consequently, all carbon (C) in biomass comes from CO₂ that was in the atmosphere at the time of the plant’s growth. This contrasts sharply with the C in fossil fuels, which has been sequestered and stored in the earth’s crust for a length of time on the order of millions of years, or even hundreds of millions, of years [12,13]. When biomass is combusted for use as a fuel, the C is released back into the atmosphere from which it was recently captured by the plant; when fossil fuels are combusted for use as a fuel, C is added back to the atmosphere for the first time since it was sequestered millions of years prior. Therefore, combustion of biomass “recycles” C already present in

the atmosphere, whereas combustion of fossil fuels adds more C to the atmosphere. In this way, replacing fossil fuels with biomass as an energy source is an attractive way to slow the growth of or stabilize the concentration of carbon in the atmosphere.

However, there are additional considerations when evaluating the attraction of biofuels as a sustainable fuel and as an alternative to petroleum-based transportation fuels. For one, the process of converting biomass into a fuel uses energy, and the associated C emissions must be considered through lifecycle analysis (LCA) or other methods [14–17]. For example, C emissions associated with growing the biomass, transporting it to the biorefinery, and powering the bio-refinery must be considered; the C emissions from transporting the bio-oil from the biorefinery to the points of use (e.g. gas stations) are similar to those from distribution of petroleum-based fuels. One LCA simulated the production process of bio-gasoline from hybrid poplar and found that the process offered ca. 50% reduction in GHG compared to conventional gasoline [17]. Another consideration must be the C emissions associated with direct and indirect land use changes induced by an increased demand for biomass. Direct changes occur when land is converted to use for growing biomass for biofuels (e.g. deforestation, or conversion from food crops to fuel crops), and indirect changes occur when food crops are displaced and induce additional land-use changes. The C emissions associated with these changes are very difficult to predict and quantify, but some studies have suggested that biofuel use thus far has increased C emissions compared to the business-as-usual case [14,18]. However, essentially all biofuel production to date has been from corn ethanol, whereas this work focuses on fast pyrolysis biofuel.

Biomass that is grown with the specific intent for use as a fuel is referred to as an

“energy crop.” An ideal energy crop will give a high yield per land area, be low energy and low cost to produce, and have low nutrient requirements. In the future, water will become a more limited natural resource, and it will become more important than an ideal energy crop be drought- and pest-resistant and have low water requirements [19]. There are a wide variety of biomass sources, and they can be generally divided into food, non-food, and aquatic crops (including algae). Biofuels made from these crops are referred to as “first generation,” “second generation,” and “third generation,” respectively. Currently, the most widely produced and used energy crops are food crops, or first-generation crops: corn (in the United States) and sugarcane (in Brazil). In 2000, crops grown for biofuel production accounted for ca. 3% of worldwide crop production by weight, and 1% of crop production by calories. Only 10 years later in 2010, just American maize and Brazilian sugarcane grown for biofuel production accounted for 6% of global crop production by weight and 4% by calories [20]. Second generation crops include non-food energy crops like miscanthus and short rotation coppice, forestry products, agricultural residues including straw, and waste materials including waste wood and municipal solid waste.

Biofuel production methods are generally divided into three categories: chemical, biochemical, and thermochemical. While all processes involve chemical transformations of the solid or liquid biomass into a liquid fuel, *biochemical* processes use the addition of biological organisms such as yeast, and *thermochemical* processes use heat (“thermo-” is the Greek prefix meaning “hot” or “heat”). Biodiesel is an example of a chemical biofuel, because the feedstock (typically vegetable oil) is converted via transesterification at or near ambient temperatures [21,22]. Bioethanol, the biofuel produced in the largest volume in the United States, is produced via a biochemical conversion process in which yeast is added

to convert the sugars and starches in the feedstock (typically cornstarch or sugarcane) to ethanol [23]. Pyrolysis biofuel is an example of a thermochemical biofuel that is produced at high temperature, atmospheric pressure, and in the complete absence of oxygen [24]. The work described herein focuses on the production of pyrolysis biofuel.

Before pyrolysis, the biomass must be prepared via drying and pulverization. To reduce water in the bio-oil product, the biomass is typically dried in order to have less than 10 wt% water. The particle size requirement depends on the reaction design, but must be on the order of magnitude of 1 mm [24]. An attractive aspect of fast pyrolysis is that it is very forgiving with the type of biomass feedstock; more than 100 different organic biomass types besides wood have been studied, including straw, olive pits, nut shells, miscanthus, sorghum, bark, sewage sludge, and leather waste [25].

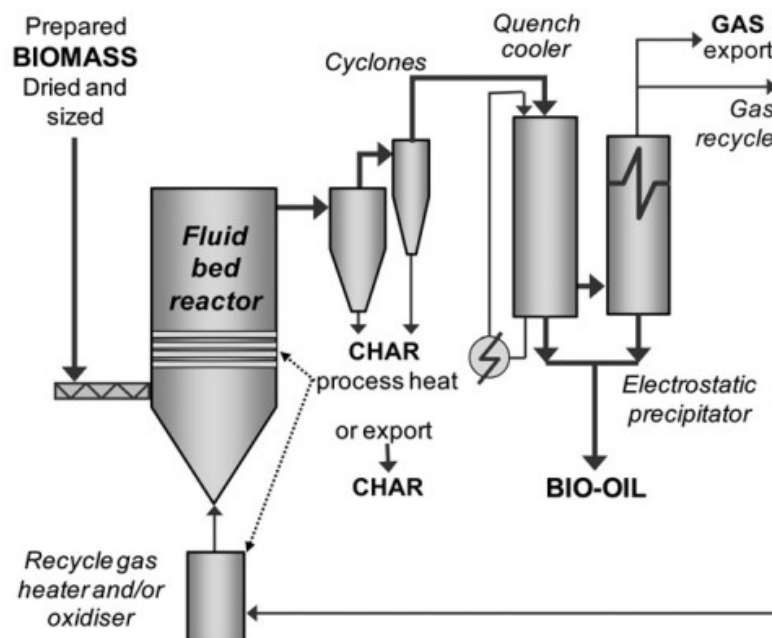


Figure 1.3. Bubbling fluid bed reactor with electrostatic precipitator [14].

After preparation, the biomass is fed to the reactor as show in Figure 1.3. In pyrolysis, three products are always produced: liquid, solids, and char. By manipulating the process conditions, including reaction time and temperature, the distribution of product types can be controlled. For “fast” pyrolysis, high temperature (near 500°C) and short residence time (~1 second) favors the production of liquid (75 wt%) over solids (12 wt%) and char (13 wt%) and minimizes secondary reactions [26]. After reaction, the char is immediately removed via cyclones to prevent further cracking. The collected char accounts for ca. 25% of the energy of the biomass feed and can be combusted to supplement the energy demands of the production process, or collected and exported. The gas stream is then quenched, and the liquid (“bio-oil”) is recovered. The remaining gas flows through an electrostatic precipitator to collect any remaining aerosols in the gas stream, which is then

added to the bio-oil. After, the gas stream can be recycled to the pyrolysis reactor.

The bio-oil that is collected from fast pyrolysis is an organic mixture of C, H, O, N, S, and water as shown in Table 1.1, taken from [27]; in comparison to petroleum crude oil, it contains more oxygen and water by weight at the expense of C and H, and is relatively devoid of N and S impurities. Those elements are arranged in a complex mixture of more than 400 unique compounds, including aldehydes, ketones, hetero-aromatics, aliphatics, methoxys, alcohols, alkenes, dibenzenes, esters, benzyls, esters, and carboxylic acids [28–30], as shown in Figure 1.4.

Bio-oil has a higher heating value of 16-19 MJ/kg and contains high water and oxygen contents of 15-30 wt% and 35-40 wt%, respectively. This compares unfavorably to heavy fuel oil, which typically has a higher heating value of 40 MJ/kg and 0.1 wt% and 1.0 wt% water and oxygen content, respectively. Also, bio-oil has high viscosity of 40-100 cP at 50 °C and low pH around 2.5 [31]. Its high viscosity makes the bio-oil difficult to store and process as a liquid, and the high acidity makes it corrosive and thermally unstable. Furthermore, the bio-oil will not mix with other hydrocarbon liquids, and therefore cannot

	Petroleum crude oil (wt%)	Pyrolysis bio-oil (wt%)
C	83-86	55-65
H	11-14	5-7
O	<1	30-50
N	<4	<0.1
S	<1	<0.05
Water	0.1	20-30

Table 1.1. Elemental composition and water content ranges of crude petroleum oils compared to pyrolysis bio-oils.

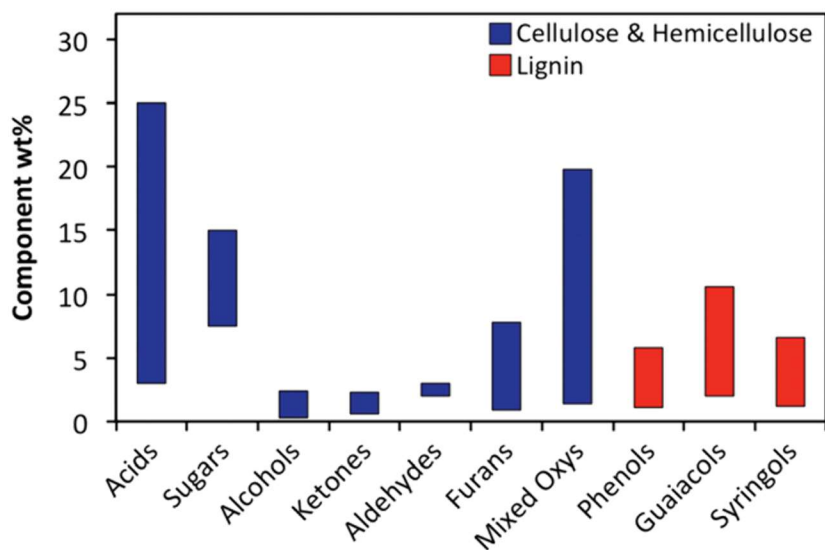


Figure 1.4. Composition ranges of pyrolysis bio-oil oxygenate functionalities correlated according to their lignocellulosic biomass source. The weight ranges are based on bio-oil analysis data reported by Milne et al [16,19].

be blended with gasoline (as ethanol is in today’s infrastructure).

Upon condensation and storage, the components of the bio-oil are in a non-equilibrium state and continue to react, resulting in changes to the density, acidity, viscosity, average molecular weight, and chemical composition, even at room temperature [32]. Additional potential changes include loss of volatiles and phase separation [26].

1.3. Biofuel and model compound upgrading

Due to the unfavorable properties described above, bio-oil cannot be used directly as a drop-in transportation fuel. For bio-oil to be upgraded to a biofuel for use as a drop-in fuel, the upgrading must accomplish three main goals; oxygen must be removed via deoxygenation, the energy density must be increased via selective hydrogenation, and the chain lengths must be increased via carbon-carbon coupling.

In addition to improving the stability, upgrading can be employed to increase heating value, improve miscibility with other fuels, and reduce corrosiveness and viscosity. To upgrade the bio-oil, several physical, chemical, and catalytic upgrading methods can be employed. Physical upgrading methods include char residue removal (filtration), solvent addition, or emulsification with the support of surfactant [26,27,32]. Several chemical upgrading options are available as well, including aqueous phase processing, aqueous phase reforming, and esterification [26]. Catalytic upgrading is the most diverse of these categories; catalytic upgrading can be *in-situ* (added to the pyrolysis step) or *ex-situ* (performed after the pyrolysis step), and *ex-situ* upgrading can be performed before condensation (on the vapor product) or after (on the liquid product). In a 2015 techno-economic report from the National Renewable Energy Laboratory and the Pacific Northwest National Laboratory, it was predicted that the both *in situ* and *ex situ* pyrolysis bio-oil could be produced for less than \$3.50 per gallon of gasoline equivalent by 2022 [33].

When re-heated after condensation, bio-oil reacts rapidly and separates into solid residue (ca. 50 wt%) and a liquid fraction containing volatile organic compounds and water [26]. Therefore, any studies of pyrolysis upgrading must generate the bio-oil vapors in the laboratory instead of being manufactured off-site, transported as a liquid, and then re-vaporized in the laboratory. An additional challenge of studying bio-oil upgrading is that, because of the immense number of molecules that are present in bio-oil, analysis techniques (predominantly gas chromatography) can generally only track changes in properties of the molecular components; for example, changes in the distribution of functional groups, average molecular size, energy density, and total acid number [34].

For catalyst studies, a model compound is often employed which replicates key important properties of the bio-oil and allows careful study of chemical transformation, while still enabling comparison of catalyst performance in a lab setting. A good model compound will contain one or more functional groups that are prevalent in bio-oil vapor so that the intramolecular selectivity of catalytic upgrading can be studied. In addition, multiple model compounds may be co-fed to study intermolecular interactions and selectivity, while also approaching the complexity of studying the upgrading of whole bio-oil. The most common model compounds that have been studied are lignin-derived phenolics including guaiacol, cresols, and anisole [35–41]. Other model compounds that have been studied include propanal and other C3 oxygenates [42], 1-octanol [43], and more. Ruddy et al. called for study of a wider array of model compounds, specifically citing acetic acid, hydroxyacetaldehyde, levoglucosan, and alkylated furans [27].

This work uses both crotonaldehyde and acetic acid as bio-oil compounds. Acetic acid and crotonaldehyde were chosen as model compounds as they represent the simplest carboxylic acid and a simple aldehyde, respectively. They also each possess multiple functionalities, and can undergo a variety of transformations, allowing for multiple reaction pathways to be probed. In addition, aldehydes and carboxylic acids are prevalent in pyrolysis vapors (up to 13 and 25 wt%, respectively) [29]. Last, acids and aldehydes are the main sources of some of the most undesirable properties of bio-oil; acids are significant contributors to the corrosiveness of bio-oils, and aldehydes are significant contributors to the instability of bio-oil [27,44].

1.4. Molybdenum carbide catalyst

Molybdenum carbide (Mo_2C) is an example of an early transition metal carbide, in which carbon sits in interstitial vacancies sites of the molybdenum crystal lattice. The crystal structure of carbide materials is governed by both geometric and electronic factors. The Hägg rule is the geometric governor and predicts that a mixture of a metal and a non-metal will form a simple structure if the ratio of the hard-ball radii of nonmetal to metal (r_x/r_M) is less than 0.59. This rule correctly predicts that Mo and C will form a simple structure since r_C/r_{Mo} is $70 \text{ pm} / 145 \text{ pm} = 0.48$ is less than 0.59 [45,46]. The electronic factor is governed by the Engel-Brewer theory of metals, which predicts that a mixture's structure depends on the s-p electron count, and therefore on the mixing of the s-p orbitals of the carbon and the s-p-d band of the metal [45].

Molybdenum carbide has two stable crystalline forms, commonly referred to as α - MoC_{1-x} and β - Mo_2C . α - MoC_{1-x} has an orthorhombic arrangement of metal atoms and carbon in the interstitial spaces, while β - Mo_2C has a hexagonal close packed arrangement of metal atoms also with carbon in the interstitial spaces [47]. These structures are shown in Figure 1.5, taken from [48]. Because of the carbon insertion in the lattice, the Mo host

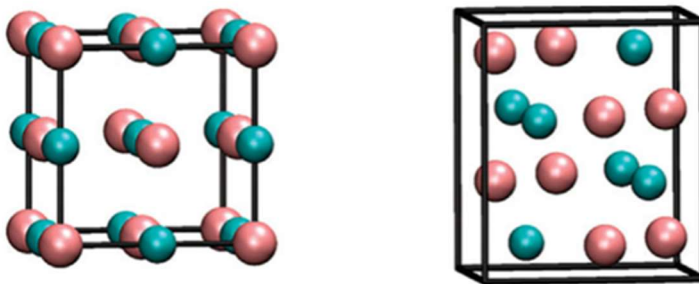


Figure 1.5. Crystal structure of fcc α - MoC_{1-x} (left) and hexagonal β - Mo_2C (right).

lattice experiences an expansion, and the Mo₂C structures have a larger metal-metal bond distances than metallic Mo.

Catalysis interest in transition-metal carbides as catalytic materials arose from a 1973 report by Levy and Boudart which found that tungsten carbide (WC) catalyzed the formation of water from hydrogen and oxygen at room temperature and the isomerization of 2,2-dimethylpropane to 2-methylbutane [49]. Previously, these reactions were only known to be catalyzed by Pt, Au, and Ir, which are all expensive noble metal catalysts, and neither are catalyzed by metallic tungsten. Levy and Boudart theorized that the noble-metal-like catalytic properties of WC arose from changes to the electron distribution of W caused by the insertion of C, and its corresponding increased electronegativity.

The WC that Levy and Boudart tested for the initial study of transition metal carbides was only 5 m²/g. Since then, synthesis techniques based on temperature-programmed reaction have been developed that enable synthesis of high surface area early transition metal carbides including Mo₂C with surface area greater around 100 m²/g. [50,51]. Generally, a reductive carburizing gas source (often CH₄/H₂) flows over a metal oxide precursor as it is heated at a constant rate from room temperature to some target temperature. Because the structure of the parent metal oxide remains intact (the transformation is topotactic), the removal of the oxygen from the lattice leaves a significant micropore structure [45]. With such high surface area, early-transition metal carbides are a good candidate for use a catalyst support for other metals [51,52].

Since their discovery as a catalytic material, early transition-metal carbides have been studied for their catalytic activity for reactions including hydrogenation of C₂+ organics [53–55], dehydrogenation [56,57], isomerization [58], hydrodeoxygenation

[41,59], Fischer Tropsch reaction [60–62], and water-gas shift reaction [45].

For bio-oil model compound upgrading, Mo₂C has been studied for selective deoxygenation of aldehyde and alcohol model compounds (propanal, 1-propanol, furfural, and furfuryl alcohol) [42,63]. Ren et. al. found that hydrodeoxygenation (HDO) of propanal over Mo₂C gave high (ca. 60%), stable selectivity to propylene during 300 min TOS. Their findings, taken from [42], are shared in Figure 1.6.

Chen et. al. reported that a mixture of anisole, m-cresol, guaiacol, and 1-2-dimethoxybenzene had yields higher than 90% to the completely deoxygenated aromatics over Mo₂C [41]. Mortensen et. al. found that Mo₂C/ZrO₂ gave decent selectivity for HDO for 1-octanol and phenol (70% and 37%, respectively) but that the catalyst deactivated during 76 time on stream (TOS) and selectivity decreased (to 37% and 19%, respectively) [43]. However, these selectivities are insufficient for cost-effective bio-oil upgrading, and higher selectivity needs to be achieved to encourage widespread adoption. One possibility is to develop selectivity control methods for controlling the selectivity of Mo₂C catalysts.

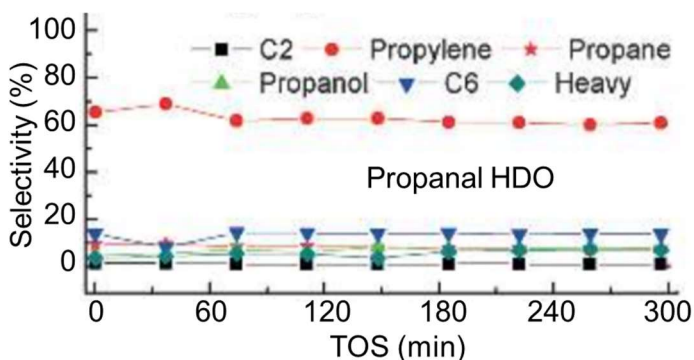


Figure 1.6. Selectivity of propanal with H₂ over Mo₂C.

1.5. Promoters for molybdenum carbide catalysts

Mo₂C was identified as a good candidate for a catalyst support because it can be synthesized with high surface area and has unique catalytic properties. Supporting metal promoters on the Mo₂C support has been used as a technique to control activity and selectivity. In an early report, Dubois et. al. found that supporting Cu on Mo₂C decreased CO₂ hydrogenation activity by ca. 10% but increased selectivity to methanol by ca. 100% [64]. Soon after, Ledoux et. al. examined Co, Rh, Pd, Ru, Pt, and Ir for their effect on the *n*-hexane reaction with Mo₂C and found that Pt, Ir, and Ru increased Mo₂C activity up to ca. 3.5 times [65]. Woo et. al. applied the concept of alkali promotion, which had previously been shown effective for conventional Fischer Tropsch catalysts, to be an effective method for increasing Fischer Tropsch selectivity to linear alcohols with Mo₂C [66]. Also for Fischer Tropsch reaction, Griboval-Constant et. al. reported that Co and Ru increased activity of Mo₂C [67]. They found that Ru decreased the selectivity to alcohols, while Co increased the selectivity to higher hydrocarbons. However, Schaidle et. al. suggested these results may be due more to intrinsic activity of the Ru and Co than to synergistic interactions between the metal and support [68]. In all these cases, passivated Mo₂C was used as the support, so the metals interacted with the oxide surface layer and not the native carbide surface.

In other findings, metals were mechanically mixed with the Mo precursor before carburization, so a mixed carbide phase was created. Xiang et. al. found that Fe, Ni, and Co mixed with K/Mo₂C shifted the selectivity of Fischer Tropsch reaction [69]. All three metals increased selectivity to hydrocarbons at the expense of alcohols, and the authors noted a corresponding decrease in the apparent activation energies of alcohol formation for

Ni and Co modified K/Mo₂C. Of the hydrocarbons produced, the modifier metals decreased selectivity to methane and increased the selectivity to C₂+ hydrocarbons. Similarly, of the alcohols produced, the metals decreased the selectivity to methanol and ethanol and increased the selectivity to C₃+ alcohols.

Another method of supporting metals on Mo₂C catalysts was pioneered in our group. The metal promoter is supported on the native Mo₂C support by aqueous wet impregnation of the native Mo₂C, and then the supported metal catalyst is subjected to passivation [52,70]. Materials prepared by this method have been studied for their performance in methanol steam reforming [70,71], water gas shift (WGS) [72–75], Fischer Tropsch reaction [68], CO₂ hydrogenation [76], deoxygenation [40], and more. For these reactions, metal addition to Mo₂C by wet impregnation was found to affect the activity and selectivity of the catalysts and offers a promising way to tune the performance of Mo₂C for particular applications.

For WGS, wet impregnation of Mo₂C with Pt was found to produce the highest rates compared to other Pt catalysts including Pt/Al₂O₃, Pt/TiO₂, and Pt/CeO₂ [73]. Schweitzer et. al. reported that there was a strong interaction between the Pt and Mo₂C, and showed through a combination of extended X-ray absorption fine structure (EXAFS), X-ray absorption near edge structure (XANES), and density functional theory (DFT) results that the Pt formed “raft-like” particles on the Mo₂C. In addition, for a series of Pt/Mo₂C catalysts with increasing Pt loading, the perimeter sites of the Pt particles were found to be more highly predicative of the WGS rate than the surface sites. Consequently, the interface of the Pt particles and the Mo₂C was identified as the location of the WGS active sites.

Wyvratt et. al. found that for WGS, Mo₂C whose native surface had been impregnated with Pt gave TOF of an order of magnitude higher than catalyst whose passivated surface had been impregnated, and was not significantly different than the TOF of unpromoted Mo₂C [72]. Using SEM, impregnation on the native surface was found to give rise to well-dispersed nanoscale Pt particles, while impregnation on the passivated surface gave large Pt particles with diameter of $19 \pm 6 \mu\text{m}$. In addition, the passivation layer was shown to inhibit the redox chemistry that typically governs the uptake of Pt onto Mo₂C during wet impregnation. These two effects – particle size and redox behavior – were identified as the source of the activity differences between the catalysts.

Baddour et. al. examined deoxygenation of a bio-oil model compound, guaiacol. They found that for Mo₂C, wet impregnation of Pd, Ni, and Pt increased the selectivity to the fully hydrogenated product, cyclohexane [40]. The largest effect was seen for Pt as shown in Figure 1.7 (taken from [40]), and the enhancement in hydrogenation selectivity

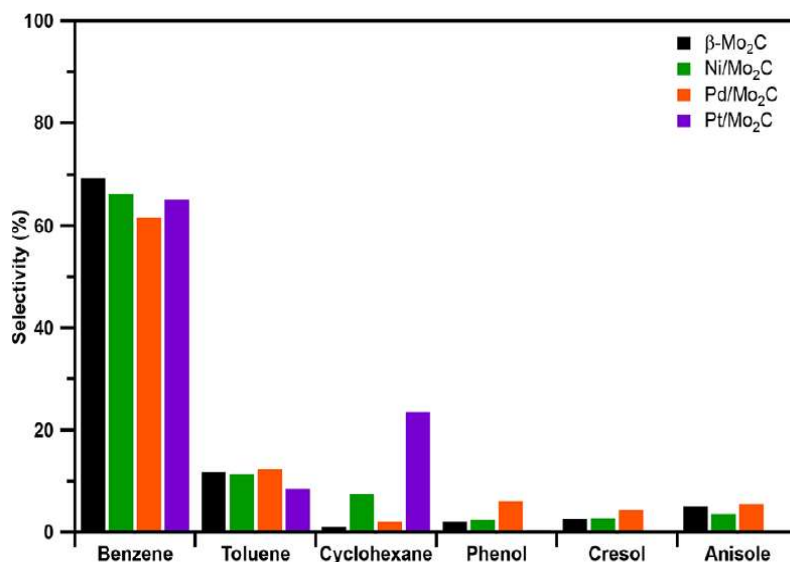


Figure 1.7. Selectivity of guaiacol deoxygenation over metal-modified Mo₂C catalysts.

was attributed to the increase in H* sites and a decrease in the acid-/H*-site ratio.

1.6. Research goals and organization of the text

The goal of this dissertation was to study the interplay between properties and performance of promoted molybdenum carbide catalysts for conversion reactions of bio-oil model compounds, and to identify the mechanisms by which the promoter metals generated changes to the activity, selectivity, and stability. The three main goals were as follows:

1. Evaluate a series of metals (Fe, Co, Ni, Cu, Rh, Pd, and K) for their promotion effects on Mo₂C catalyst for bio-oil model compound conversion and to find periodic and group trends, and identify metals for further investigation
2. Develop relationships between the amount of metal promotion (K and Fe) and the activity and selectivity for conversion of bio-oil model compounds with Mo₂C
3. Identify the role of active site densities in modulating the selectivity of metal-modified (K and Fe) Mo₂C catalysts for bio-oil model compound upgrading

This dissertation is organized into six chapters, and brief descriptions of each chapter are given below:

Chapter 1: Introduction

This chapter explains the motivation for this work and introduces the reader to

critical concepts that form the basis of the research including the process of converting biomass to bio-oil, the upgrading of that bio-oil into biofuel, catalysis and molybdenum carbide catalysts specifically, and the manner in which promoter metals are used to modify catalysts to control the upgrading of bio-oil into biofuel.

Chapter 2: Metal/Mo₂C catalysts for crotonaldehyde upgrading

Some promoter metals (Ni, Cu, Fe, and K) were found to shift the selectivity of crotonaldehyde conversion when supported on Mo₂C catalysts. In particular, Ni, Cu, and K increased the selectivity to the isomerization product, while Fe increased the selectivity to the HDO products. Meanwhile, Rh, Pd, and Co did not significantly affect catalyst activity or selectivity. K/Mo₂C and Fe/Mo₂C gave very low selectivity for butyraldehyde, suggesting that they have a high affinity for hydrogenation of the C=O bond.

Chapter 3: Selectivity of biomass model compound upgrading over K-promoted Mo₂C

Since K was found to create the largest shift in selectivity to the isomerization product, it was investigated more carefully for its effect as a promoter for upgrading with Mo₂C catalyst. For both acetic acid and crotonaldehyde model compounds, K promotion up to 0.5ML was found to shift selectivity to the ketonization and isomerization products, respectively. Beyond this amount of promotion, the effect of K was incremental and reversed for acetic acid and crotonaldehyde conversion, respectively. It was theorized that the change in effect of K promotion beyond 0.5ML up to 1.1ML was due to the difference in the way that K dispersed on the catalyst surface at high loadings compared to low

loadings.

Chapter 4: Linking active site types and selectivity for K-promoted Mo₂C

Base, acid, and H* site concentrations on Mo₂C and K/Mo₂C catalysts were measured via temperature-programmed desorption (TPD) of CO₂, NH₃, and H₂ probe molecules. K addition to Mo₂C created base sites and eliminated acid and H* sites. Via deconvolution of the TPD spectra, the base and acid sites were further separated into weak and strong sites. The active site concentrations were correlated to the productivity of each product for acetic acid and crotonaldehyde conversion on K/Mo₂C catalysts with K promotion from 0 to 1.1ML. Strong correlations suggested that active site was responsible for the formation of that product; base sites were identified as the active site for the dominant product at high K loadings (acetone for acetic acid conversion; 3-butenal for crotonaldehyde conversion).

Chapter 5: Pathway of selectivity influence for transition versus alkali metals

Iron, identified in chapter 2 as a promoter that shifted selectivity to HDO products, was investigated to determine the mechanism of promotion. Mo₂C was promoted with Fe up to 1.1ML via incipient wetness, since wet impregnation does not allow for high loadings of Fe. Incipient wetness of small loadings of Fe was found to shift selectivity,

Chapter 6: Summary and future work

In this chapter, the work presentation in the dissertation is summarized and synthesized. Areas of future research are proposed that would deepen and strengthen the

results from this work.

1.7. References

- [1] M. Roser, Economic Growth, *Our World in Data* (n.d.). <https://ourworldindata.org/economic-growth#globally-over-the-last-two-millennia-until-today>.
- [2] M. Roser, O.-O. Esteban, Literacy, *Our World in Data* (n.d.). <https://ourworldindata.org/literacy>.
- [3] Education: Literacy rate, UNESCO Institute for Statistics, n.d. <http://data.uis.unesco.org/>.
- [4] Global Health and Aging, *National Institute on Aging* (n.d.). https://www.nia.nih.gov/sites/default/files/2017-06/global_health_aging.pdf.
- [5] The World at Six Billion, (n.d.). <https://www.un.org/esa/population/publications/sixbillion/sixbilpart1.pdf>.
- [6] V. Smil, *Creating the Twentieth Century: Technical Innovations of 1867–1914*, Oxford University Press, New York, 2005.
- [7] A. Mazur, Does Increasing Energy or Electricity Consumption Improve Quality of Life in Industrial Nations?, *Energy Policy* 39 (2011) 2568–2572. doi:10.1016/j.enpol.2011.02.024.
- [8] P. Ghosh, W. A. Brand, Stable Isotope Ratio Mass Spectrometry in Global Climate Change Research, *International Journal of Mass Spectrometry* 228 (2003) 1–33. doi:10.1016/S1387-3806(03)00289-6.
- [9] A. Stips, D. Macias, C. Coughlan, E. Garcia-Gorriz, X. S. Liang, On the Causal Structure between CO₂ and Global Temperature, *Scientific Reports* 6 (2016) 1–9. doi:10.1038/srep21691.
- [10] Global Greenhouse Gas Emissions Data, United States Environmental Protection Agency, n.d. <https://www.epa.gov/ghgemissions/global-greenhouse-gas-emissions-data#Sector>.
- [11] K. Ever, “Drop-In” Biofuels Solve Integration Issues?, *National Renewable Energy Institute* (n.d.). https://www.nrel.gov/continuum/sustainable_transportation/biofuels.html.

- [12] D. S. Macgregor, Factors Controlling the Destruction or Preservation of Giant Light Oilfields, *Petroleum Geoscience* 2 (1996) 197–217. doi:10.1144/petgeo.2.3.197.
- [13] P. Mann, L. Gahagan, M. B. Gordon, Tectonic Setting of the World's Giant Oil and Gas Fields, in: M.T. Halbouty (Ed.), *Giant Oil and Gas Fields of the Decade, 1990-1999*, AAPG Memoir 78, 2003: pp. 15–105.
- [14] J. M. DeCicco, D. Y. Liu, J. Heo, R. Krishnan, A. Kurthen, L. Wang, Carbon Balance Effects of U.S. Biofuel Production and Use, *Climatic Change* 138 (2016) 667–680. doi:10.1007/s10584-016-1764-4.
- [15] J. Han, A. Elgowainy, J. B. Dunn, M. Q. Wang, Life Cycle Analysis of Fuel Production from Fast Pyrolysis of Biomass, *Bioresource Technology* 133 (2013) 421–428. doi:10.1016/j.biortech.2013.01.141.
- [16] D. D. Hsu, Life Cycle Assessment of Gasoline and Diesel Produced via Fast Pyrolysis and Hydroprocessing, *Biomass and Bioenergy* 45 (2012) 41–47. doi:10.1016/j.biombioe.2012.05.019.
- [17] J. F. Peters, D. Iribarren, J. Dufour, Simulation and Life Cycle Assessment of Biofuel Production via Fast Pyrolysis and Hydrougrading, *Fuel* 139 (2015) 441–456. doi:10.1016/j.fuel.2014.09.014.
- [18] T. Searchinger, R. Heimlich, R. A. Houghton, F. Dong, A. Elobeid, J. Fabiosa, S. Tokgoz, D. Hayes, T.-H. Yu, Use of U.S. Croplands for Biofuels Increases Greenhouse Gases Through Emissions from Land-Use Change, *Science* 319 (2008) 1238–1240. doi:10.1126/science.1151861.
- [19] P. McKendry, Energy Production from Biomass (Part 1): Overview of Biomass, *Bioresource Technology* 83 (2002) 37–46. doi:10.1016/S0960-8524(01)00118-3.
- [20] E. S. Cassidy, P. C. West, J. S. Gerber, J. A. Foley, Redefining Agricultural Yields: From Tonnes to People Nourished per Hectare, *Environmental Research Letters* 8 (2013) 034015. doi:10.1088/1748-9326/8/3/034015.
- [21] M. Canakci, J. Van Gerpen, Biodiesel Production from Oils and Fats with High Free Fatty Acids, *Transactions of the ASAE* 44 (2001). doi:10.13031/2013.7010.
- [22] Y. Zhang, Biodiesel Production from Waste Cooking Oil: 1. Process Design and Technological Assessment, *Bioresource Technology* 89 (2003) 1–16. doi:10.1016/S0960-8524(03)00040-3.
- [23] C. E. Wyman, ed., *Handbook on Bioethanol: Production and Utilization*, Taylor & Francis, Washington, DC, 1996.
- [24] A. V. Bridgwater, D. Meier, D. Radlein, An Overview of Fast Pyrolysis of Biomass, *Organic Geochemistry* 30 (1999) 1479–1493. doi:10.1016/S0146-6380(99)00120-5.

- [25] D. Mohan, C. U. Pittman, P. H. Steele, Pyrolysis of Wood/Biomass for Bio-Oil: A Critical Review, *Energy & Fuels* 20 (2006) 848–889. doi:10.1021/ef0502397.
- [26] A. V. Bridgwater, Review of Fast Pyrolysis of Biomass and Product Upgrading, *Biomass and Bioenergy* 38 (2012) 68–94. doi:10.1016/j.biombioe.2011.01.048.
- [27] D. A. Ruddy, J. A. Schaidle, J. R. Ferrell III, J. Wang, L. Moens, J. E. Hensley, Recent Advances in Heterogeneous Catalysts for Bio-Oil Upgrading via “Ex Situ Catalytic Fast Pyrolysis”: Catalyst Development Through the Study of Model Compounds, *Green Chemistry* 16 (2014) 454–490. doi:10.1039/C3GC41354C.
- [28] C. Branca, P. Giudicianni, C. Di Blasi, GC/MS Characterization of Liquids Generated from Low-Temperature Pyrolysis of Wood, *Industrial & Engineering Chemistry Research* 42 (2003) 3190–3202.
- [29] T. Milne, F. Agblevor, M. David, S. Deutch, D. Johnson, Developments in Thermochemical Biomass Conversion, Blackie Academic and Professional, London, U.K., 1997.
- [30] C. A. Mullen, G. D. Strahan, A. A. Boateng, Characterization of Various Fast-Pyrolysis Bio-Oils by NMR Spectroscopy, *Energy Fuels* 23 (2009) 2707–2718. doi:10.1021/ef801048b.
- [31] Q. Zhang, J. Chang, T. Wang, Y. Xu, Review of Biomass Pyrolysis Oil Properties and Upgrading Research, *Energy Conversion and Management* 48 (2007) 87–92. doi:10.1016/j.enconman.2006.05.010.
- [32] Z. Yang, A. Kumar, R. L. Huhnke, Review of Recent Developments to Improve Storage and Transportation Stability of Bio-Oil, *Renewable and Sustainable Energy Reviews* 50 (2015) 859–870. doi:10.1016/j.rser.2015.05.025.
- [33] A. Dutta, A. Sahir, E. Tan, D. Humbird, L. J. Snowden_Swan, P. Meyer, J. Ross, D. Sexton, R. Yap, J. Lukah, Process Design and Economics for the Conversion of Lignocellulosic Biomass to Hydrocarbon Fuels: Thermochemical Research Pathways with In Situ and Ex Situ Upgrading of Fast Pyrolysis Vapors, National Renewable Energy Laboratory, 2015.
- [34] A. Oasmaa, D. C. Elliott, J. Korhonen, Acidity of Biomass Fast Pyrolysis Bio-Oils, *Energy & Fuels* 24 (2010) 6548–6554. doi:10.1021/ef100935r.
- [35] M. V. Bykova, D. Y. Ermakov, V. V. Kaichev, O. A. Bulavchenko, A. A. Saraev, M. Y. Lebedev, V. a. Yakovlev, Ni-Based Sol–Gel Catalysts as Promising Systems for Crude Bio-Oil Upgrading: Guaiacol Hydrodeoxygenation Study, *Applied Catalysis B: Environmental* 113–114 (2012) 296–307. doi:10.1016/j.apcatb.2011.11.051.
- [36] T. M. Sankaranarayanan, A. Berenguer, C. Ochoa-Hernández, I. Moreno, P. Jana, J. M. Coronado, D. P. Serrano, P. Pizarro, Hydrodeoxygenation of Anisole as Bio-Oil

- Model Compound over Supported Ni and Co Catalysts: Effect of Metal and Support Properties, *Catalysis Today* 243 (2015) 163–172. doi:10.1016/j.cattod.2014.09.004.
- [37] M. Saidi, F. Samimi, D. Karimipourfard, T. Nimmanwudipong, B. C. Gates, M. R. Rahimpour, Upgrading of Lignin-Derived Bio-Oils by Catalytic Hydrodeoxygenation, *Energy & Environmental Science* 7 (2014) 103–129. doi:10.1039/C3EE43081B.
- [38] V. A. Yakovlev, S. A. Khromova, O. V. Sherstyuk, V. O. Dundich, D. Y. Ermakov, V. M. Novopashina, M. Y. Lebedev, O. Bulavchenko, V. N. Parmon, Development of New Catalytic Systems for Upgraded Bio-Fuels Production from Bio-Crude-Oil and Biodiesel, *Catalysis Today* 144 (2009) 362–366. doi:10.1016/j.cattod.2009.03.002.
- [39] H. Y. Zhao, D. Li, P. Bui, S. T. Oyama, Hydrodeoxygenation of Guaiacol as Model Compound for Pyrolysis Oil on Transition Metal Phosphide Hydroprocessing Catalysts, *Applied Catalysis A: General* 391 (2011) 305–310. doi:10.1016/j.apcata.2010.07.039.
- [40] F. G. Baddour, V. A. Witte, C. P. Nash, M. B. Griffin, D. A. Ruddy, J. A. Schaidle, Late-Transition-Metal-Modified β - Mo_2C Catalysts for Enhanced Hydrogenation during Guaiacol Deoxygenation, *ACS Sustainable Chemistry & Engineering* 5 (2017) 11433–11439. doi:10.1021/acssuschemeng.7b02544.
- [41] C.-J. Chen, W.-S. Lee, A. Bhan, Mo_2C Catalyzed Vapor Phase Hydrodeoxygenation of Lignin-Derived Phenolic Compound Mixtures to Aromatics under Ambient Pressure, *Applied Catalysis A: General* 510 (2016) 42–48. doi:10.1016/j.apcata.2015.10.043.
- [42] H. Ren, W. Yu, M. Saliccioli, Y. Chen, Y. Huang, K. Xiong, D. G. Vlachos, J. G. Chen, Selective Hydrodeoxygenation of Biomass-Derived Oxygenates to Unsaturated Hydrocarbons Using Molybdenum Carbide Catalysts, *ChemSusChem* 6 (2013) 798–801. doi:10.1002/cssc.201200991.
- [43] P. M. Mortensen, H. W. P. de Carvalho, J.-D. Grunwaldt, P. A. Jensen, A. D. Jensen, Activity and Stability of $\text{Mo}_2\text{C}/\text{ZrO}_2$ as Catalyst for Hydrodeoxygenation of Mixtures of Phenol and 1-Octanol, *Journal of Catalysis* 328 (2015) 208–215. doi:10.1016/j.jcat.2015.02.002.
- [44] G. W. Huber, S. Iborra, A. Corma, Synthesis of Transportation Fuels from Biomass: Chemistry, Catalysts, and Engineering, *Chemical Reviews* 106 (2006) 4044–4098. doi:10.1021/cr068360d.
- [45] S. T. Oyama, Preparation and Catalytic Properties of Transition Metal Carbides and Nitrides, *Catalysis Today* 15 (1992) 179–200. doi:10.1016/0920-5861(92)80175-M.
- [46] J. C. Slater, Atomic Radii in Crystals, *The Journal of Chemical Physics* 41 (1964) 3199–3204. doi:10.1063/1.1725697.

- [47] E. Parthé, V. Sadogopan, The Structure of Dimolybdenum Carbide by Neutron Diffraction Technique, *Acta Crystallographica* 16 (1963) 202–205. doi:10.1107/S0365110X63000487.
- [48] P. A. Alaba, A. Abbas, J. Huang, W. M. A. W. Daud, Molybdenum Carbide Nanoparticle: Understanding the Surface Properties and Reaction Mechanism for Energy Production towards a Sustainable Future, *Renewable and Sustainable Energy Reviews* 91 (2018) 287–300. doi:10.1016/j.rser.2018.03.106.
- [49] R. B. Levy, M. Boudart, Platinum-Like Behavior of Tungsten Carbide in Surface Catalysis, *Science* 181 (1973) 547–549. <http://www.jstor.org/stable/1736506>.
- [50] J. Lee, S. T. Oyama, M. Boudart, Molybdenum Carbide Catalysts I. Synthesis of Unsupported Powders, *Journal of Catalysis* 106 (1987) 125–133. doi:10.1016/0021-9517(87)90218-1.
- [51] J. A. Schaidle, A. C. Lausche, L. T. Thompson, Effects of Sulfur on Mo₂C and Pt/Mo₂C Catalysts: Water Gas Shift Reaction, *Journal of Catalysis* 272 (2010) 235–245. doi:10.1016/j.jcat.2010.04.004.
- [52] J. A. Schaidle, N. M. Schweitzer, O. T. Ajenifujah, L. T. Thompson, On the Preparation of Molybdenum Carbide-Supported Metal Catalysts, *Journal of Catalysis* 289 (2012) 210–217. doi:10.1016/j.jcat.2012.02.012.
- [53] J. S. Lee, M. H. Yeom, K. Y. Park, I.-S. Nam, J. S. Chung, Y. G. Kim, S. H. Moon, Preparation and Benzene Hydrogenation Activity of Supported Molybdenum Carbide Catalysts, *Journal of Catalysis* 128 (1991) 126–136. doi:10.1016/0021-9517(91)90072-C.
- [54] M.-L. Frauwallner, F. López-Linares, J. Lara-Romero, C. E. Scott, V. Ali, E. Hernández, P. Pereira-Almao, Toluene Hydrogenation at Low Temperature Using a Molybdenum Carbide Catalyst, *Applied Catalysis A: General* 394 (2011) 62–70. doi:10.1016/j.apcata.2010.12.024.
- [55] X. Liu, K. J. Smith, Acidity and Deactivation of Mo₂C/HY Catalysts Used for the Hydrogenation and Ring Opening of Naphthalene, *Applied Catalysis A: General* 335 (2008) 230–240. doi:10.1016/j.apcata.2007.11.028.
- [56] M. K. Neylon, S. Choi, H. Kwon, K. E. Curry, L. T. Thompson, Catalytic Properties of Early Transition Metal Nitrides and Carbides: N-Butane Hydrogenolysis, Dehydrogenation and Isomerization, *Applied Catalysis A: General* 183 (1999) 253–263. doi:10.1016/S0926-860X(99)00053-8.
- [57] T. G. Kelly, J. G. Chen, Controlling C–O, C–C and C–H Bond Scission for Deoxygenation, Reforming, and Dehydrogenation of Ethanol Using Metal-Modified Molybdenum Carbide Surfaces, *Green Chem.* 16 (2014) 777–784.

doi:10.1039/C3GC41259H.

- [58] J. Han, J. Duan, P. Chen, H. Lou, X. Zheng, H. Hong, Nanostructured Molybdenum Carbides Supported on Carbon Nanotubes as Efficient Catalysts for One-Step Hydrodeoxygenation and Isomerization of Vegetable Oils, *Green Chemistry* 13 (2011) 2561–2568. doi:10.1039/c1gc15421d.
- [59] S. Liu, H. Wang, K. J. Smith, C. S. Kim, Hydrodeoxygenation of 2-Methoxyphenol over Ru, Pd, and Mo₂C Catalysts Supported on Carbon, *Energy & Fuels* 31 (2017) 6378–6388. doi:10.1021/acs.energyfuels.7b00452.
- [60] J. A. Schaidle, L. T. Thompson, Fischer–Tropsch Synthesis over Early Transition Metal Carbides and Nitrides: CO Activation and Chain Growth, *Journal of Catalysis* 329 (2015) 325–334. doi:10.1016/j.jcat.2015.05.020.
- [61] I. Kojima, E. Miyazaki, Catalysis by Transition Metal Carbides: V. Kinetic Measurements of Hydrogenation of CO over TaC, TiC, and Mo₂C Catalyst, *Journal of Catalysis* 89 (1984) 168–171.
- [62] P. Patterson, Carbon Monoxide Hydrogenation over Molybdenum and Tungsten Carbides, *Applied Catalysis A: General* 251 (2003) 449–455. doi:10.1016/S0926-860X(03)00371-5.
- [63] K. Xiong, W. Yu, J. G. Chen, Selective Deoxygenation of Aldehydes and Alcohols on Molybdenum Carbide (Mo₂C) Surfaces, *Applied Surface Science* 323 (2014) 88–95. doi:10.1016/j.apsusc.2014.06.100.
- [64] J.-L. Dubois, K. Sayama, H. Arakawa, CO₂ Hydrogenation over Carbide Catalysts, *Chemistry Letters* (1992) 5–8.
- [65] M. J. Ledoux, C. P. Huu, J. Guille, H. Dunlop, Compared Activities of Platinum and High Specific Surface Area Mo₂C and WC Catalysts for Reforming Reactions I. Catalyst Activation and Stabilization: Reaction of n-Hexane, *Journal of Catalysis* 134 (1992) 383–398. doi:10.1016/0021-9517(92)90329-G.
- [66] H. C. Woo, K. Y. Park, Y. G. Kim, I.-S. Namau]Jong Shik Chung, J. S. Lee, Mixed Alcohol Synthesis from Carbon Monoxide and Dihydrogen over Potassium-Promoted Molybdenum Carbide Catalysts, *Applied Catalysis* 75 (1991) 267–280. doi:10.1016/S0166-9834(00)83136-X.
- [67] A. Griboval-Constant, J.-M. Giraudon, G. Leclercq, L. Leclercq, Catalytic Behaviour of Cobalt or Ruthenium Supported Molybdenum Carbide Catalysts for FT Reaction, *Applied Catalysis A: General* 260 (2004) 35–45. doi:10.1016/j.apcata.2003.10.031.
- [68] J. A. Schaidle, Carbide and Nitride Based Catalysts for Synthesis Gas Conversion, Ph. D. Thesis, University of Michigan, 2011.

- [69] M. Xiang, D. Li, H. Xiao, J. Zhang, H. Qi, W. Li, B. Zhong, Y. Sun, Synthesis of Higher Alcohols from Syngas over Fischer–Tropsch Elements Modified K/ β -Mo₂C Catalysts, *Fuel* 87 (2008) 599–603. doi:10.1016/j.fuel.2007.01.041.
- [70] W. Setthapun, S. K. Bej, L. T. Thompson, Carbide and Nitride Supported Methanol Steam Reforming Catalysts: Parallel Synthesis and High Throughput Screening, *Topics in Catalysis* 49 (2008) 73–80. doi:10.1007/s11244-008-9070-7.
- [71] A. C. Lausche, J. A. Schaidle, L. T. Thompson, Understanding the Effects of Sulfur on Mo₂C and Pt/Mo₂C Catalysts: Methanol Steam Reforming, *Applied Catalysis A: General* 401 (2011) 29–36. doi:10.1016/j.apcata.2011.04.037.
- [72] B. M. Wyvratt, J. R. Gaudet, L. T. Thompson, Effects of Passivation on Synthesis, Structure and Composition of Molybdenum Carbide Supported Platinum Water–Gas Shift Catalysts, *Journal of Catalysis* 330 (2015) 280–287. doi:10.1016/j.jcat.2015.07.023.
- [73] N. M. Schweitzer, J. A. Schaidle, O. K. Ezekoye, X. Pan, S. Linic, L. T. Thompson, High Activity Carbide Supported Catalysts for Water Gas Shift, *Journal of the American Chemical Society* 133 (2011) 2378–2381. doi:10.1021/ja110705a.
- [74] Y. Chen, S. Choi, L. T. Thompson, Low-Temperature CO₂ Hydrogenation to Liquid Products via a Heterogeneous Cascade Catalytic System, *ACS Catalysis* 5 (2015) 1717–1725. doi:10.1021/cs501656x.
- [75] G. Wang, J. A. Schaidle, M. B. Katz, Y. Li, X. Pan, L. T. Thompson, Alumina Supported Pt–Mo₂C Catalysts for the Water–Gas Shift Reaction, *Journal of Catalysis* 304 (2013) 92–99. doi:10.1016/j.jcat.2013.04.007.
- [76] Y. Chen, S. Choi, L. T. Thompson, Low Temperature CO₂ Hydrogenation to Alcohols and Hydrocarbons over Mo₂C Supported Metal Catalysts, *Journal of Catalysis* 343 (2016) 147–156. doi:10.1016/j.jcat.2016.01.016.

CHAPTER 2

Metal/Mo₂C catalysts for crotonaldehyde upgrading

2.1. Introduction

The purpose of this chapter was to evaluate promoter metals for the effects they had on the activity, selectivity, and stability of Mo₂C for crotonaldehyde conversion. The goal was also to identify possible periodic trends in these effects. Previous literature was used as a guide for the selection of which promoter metals to evaluate. Fe [1–4], Co [1,3–6], Ni [3,4,7], Cu [1,4,7–10], Ru [5,6,11], Rh [6,11], and Pd [1,4,11] were selected because they have been studied as promoter metals on Mo₂C and because they gave the chance to study both periodic and group trends. K [2,3,12–15] was selected as a representative promoter of alkali metal promoters, and because it has been studied extensively for dramatically shifting selectivity of other organic upgrading reactions including Fischer Tropsch reaction and WGS.

Fe has been studied as both modifier and promoter of Mo₂C. As a “modifier”, a substance is physically mixed with a catalyst or catalyst support, such that it is present in the bulk of the catalyst and not solely on the surface; this is in contrast to a “promoter” which is solely added to the catalyst or catalyst support surface. As a modifier, reports on the effects of Fe addition to K/Mo₂C have been conflicting. Xiang et. al. reported that Fe addition (Fe/Mo=1/8) shifted selectivity from alcohols to hydrocarbons for the Fischer Tropsch reaction [3]; Wang et. al. reported that Fe addition to K/Mo₂C improved selectivity

to alcohols while decreasing selectivity to hydrocarbons, and that the optimal ratio for this modification was Fe/Mo=1/14 [2]. Xiang only tested on Fe/Mo ratio, and Wang did not test ratios as large as 1/8, so this may explain the discrepancy. Fe/Mo₂C prepared via wet impregnation was found to not appreciably change the rate or selectivity for Fischer Tropsch reaction [4]. Chen et. al prepared Fe(0.38ML)/Mo₂C by incipient wetness of the native (unpassivated) Mo₂C surface and showed that Fe promotion increased C₂+ productivity for CO₂ hydrogenation [1]. They proposed that the changes are due to Fe increasing the concentration of associative adsorption sites. A more thorough exploration of Fe promotion is given in Chapter 5.

Co-modified K/Mo₂C increased selectivity to C₂+ alcohols and hydrocarbons for the Fischer Tropsch reaction [3]. Wet impregnation of 1 wt% Co on passivated Mo₂C increased Fischer Tropsch activity and also was found to increase formation of C₂+ hydrocarbons. [5]. The Mo₂C and Co/Mo₂C had very low BET surface areas (<10 m² g⁻¹) though, and therefore likely had minimal pore structures. Chen et. al reported that .39ML of Co added to Mo₂C by incipient wetness increased C₂+ productivity for CO₂ hydrogenation, but slightly less than Fe did [1]. Schaidle reported that Co added to Mo₂C by wet impregnation was the only promoter in the series tested that was found to change rate and selectivity for Fischer Tropsch reaction; it depressed the product formation rate but increased selectivity to hydrocarbons and alcohols [6]. Wyvratt reported similar changes in Fischer Tropsch selectivity with wet impregnation of Mo₂C with Co, but highlighted that the changes in selectivity are much less than expected, given that Co/SiO₂ is highly active for Fischer Tropsch reaction [16].

Ni/Mo₂C prepared via wet impregnation was found to not appreciably change the

rate or selectivity for Fischer Tropsch reaction [4]. Ni deposited on a Mo₂C/Mo(110) substrate decreased total activity compared to C/Mo(110), but shifted selectivity from decomposition and methanation to reforming for ethanol reaction [7]. 1.4ML of Ni gave a bigger reduction in total activity and shift in selectivity than 0.7ML of Ni.

Cu/Mo₂C prepared via wet impregnation was found to not appreciably change the rate or selectivity for Fischer Tropsch reaction [4]. Cu deposited on a Mo₂C/Mo(110) substrate shifted selectivity from decomposition and methanation to acetaldehyde formation for ethanol conversion [7]. 1.0ML of Cu did not shift the selectivity more than 0.5ML, but it did reduce the total activity compared to Mo₂C and 0.5ML of Cu addition.

Ru/Mo₂C prepared by incipient wetness of the passivated Mo₂C surface increased rate and yield for n-hexane reforming compared to Mo₂C, which was attributed to Ru enabling Mo reduction metallic Mo [11]. This is an insufficient justification, since Mo metal is not known to be active for this reaction. Ru/Mo₂C prepared via wet impregnation was found to not appreciably change the rate or selectivity for Fischer Tropsch reaction [4]. Ru(1 wt%)/Mo₂C prepared by wet impregnation of passivated Mo₂C was observed to increase rate but decrease alcohol formation for Fischer Tropsch reaction [5]. The increase in rate was less than the change observed with Co promotion in the same study. However, Wyvratt found that Ru/Mo₂C prepared by wet impregnation of native Mo₂C did not increase rate or selectivity of Fischer Tropsch reaction up to 20 wt% Ru, which he attributed to deactivation of Ru when it is pretreated at high temperatures [16].

Incipient wetness of Mo₂C with Rh was found to substantially reduce the rate of n-hexane reforming [11]. It was unclear whether the incipient wetness was performed on the native or passivated Mo₂C surface; it was very likely the passivated surface. Rh

[6,11]/Mo₂C prepared via wet impregnation was found to not appreciably change the rate or selectivity for Fischer Tropsch reaction [4].

Wet impregnation of Mo₂C with Pd was found to increase CO₂ conversion rate and production of methanol for liquid-phase CO₂ hydrogenation, even though active sites (as measured by CO chemisorption) decreased [1]. Pd promotion of Mo₂C by incipient wetness of the passivated Mo₂C surface reduced the rate and yield for n-hexane reforming [11].

A thorough investigation of K promotion is given in Chapter 3.

The results from this chapter were used as a basis for selecting which promoter metals warranted further investigation in Chapters 3-5 with regard to the extent of the selectivity effects and the mechanism by which these selectivity effects occurred.

2.2. Experimental Methods

2.2.1 Catalyst Synthesis

The Mo₂C was synthesized by a previously reported temperature-programmed reaction (TPR) method [4]. Briefly, the ammonium paramolybdate precursor, (NH₄)₆Mo₇O₂₄·4H₂O (Alfa Aesar, 81-83% as MoO₃), was sieved to yield particles between 125–250 μm. Then, 1.3 g of precursor was loaded into a vertical quartz reactor tube and supported on quartz wool, and then enclosed in a vertical programmable furnace. The precursor was heated in 400 mL min⁻¹ of H₂ gas from room temperature (RT) to 350 °C at 5 °C min⁻¹ and followed by a 12 h soak. The gas was then changed to 400 mL min⁻¹ 15% CH₄/H₂ and the precursor was heated to 590 °C at 2.7 °C min⁻¹ followed by a 2 h soak. The reactor tube was then removed from the furnace and quenched to room temperature. For the preparation of Mo₂C catalyst with no supported metal, the material was passivated in

20 mL/min of 1% O₂/He flowed through the reactor for at least 6 hrs.

Mo₂C catalysts promoted with Fe, Co, Rh, and Pd were prepared via wet impregnation. Previous work has shown Mo₂C can be promoted by wet impregnation with metal precursors that have high standard reduction potentials, that nitrate precursors tend to produce loadings closer to the nominal loading, and that electrostatic interactions may play a role in the promotion process [4,6]. Consequently, the metal precursors used were Cu(NO₃)₂•3H₂O, Co(NO₃)₂•6H₂O (Johnson Matthey), RhCl₃ (Johnson Matthey), Ni(NO₃)₂•6H₂O (Fisher Scientific, 99.0%), and Pd(NH₃)₄(NO₃)₂. First, 70 mL of deionized water was added to a glass container. Argon gas was bubbled through the water for at least 15 min to remove any dissolved oxygen. Then, the target amount of metal precursor salt was added to the water, and Ar was bubbled through the water for at least 15 min. The target amount of metal precursor corresponded to a surface coverage of 10% of a monolayer of the Mo₂C support, which has a surface area of 110 ± 20 m² g⁻¹ and is assumed to have 10¹⁹ sites m⁻² [17]. Prior to passivation, the Mo₂C catalyst (0.75 g) was transferred under Ar to the metal precursor solution. The powder was left in the solution overnight and Ar was continuously bubbled through the solution. Next, the material was transferred back into the vertical packed bed synthesis reactor without exposure to air. The samples were dried at 110°C for 2 hrs in 400 mL min⁻¹ H₂, and then reduced in 400 mL min⁻¹ H₂ at 450°C for 4 hrs. After being quenched to RT in flowing H₂, the material was passivated in 20 mL min⁻¹ of 1% O₂/He for at least 6 hrs.

Mo₂C catalysts promoted with K, Fe, and Ru were prepared via incipient wetness because they are known to not deposit well onto Mo₂C via wet impregnation [4,6]. The metal precursors were K₂CO₃ (Sigma Aldrich, 99.0%), RuCl₃•3H₂O (Alfa Aesar, 99.9%),

and $\text{Fe}(\text{NO}_3)_3 \cdot 9\text{H}_2\text{O}$ (Fisher Scientific). First, approximately 25 mL of deionized water was added to a small glass vial. Argon or nitrogen gas was bubbled through the water for at least 15 min to remove any dissolved oxygen. Then, the target amount of metal precursor salt was placed in a separate glass vial. The target amount of metal precursor corresponded to a surface coverage of 10% of a monolayer of the Mo_2C support. Prior to passivation, the Mo_2C powder was transferred under CH_4/H_2 blanket to an oxygen-free glovebox, along with the de-aerated water and the metal precursor salt. An amount of water equal to the pore volume of the Mo_2C sample ($130.4 \mu\text{L g}^{-1}$) was added to the metal salt, and the solution was shaken until the salt dissolved. The metal salt solution was added dropwise to the Mo_2C with substantial stirring and agitation between each addition. Then, the powder was dried at 110°C for at least one hour in the oxygen-free environment. The material was transferred back into the vertical packed bed synthesis reactor in an oxygen-free environment and transferred back to the programmable furnace under an Ar blanket. The catalyst was dried at 110°C for 2 hrs in $400 \text{ mL min}^{-1} \text{ H}_2$, and then reduced in $400 \text{ mL min}^{-1} \text{ H}_2$ at 450°C for 4 hrs. After being quenched to RT in flowing H_2 , the samples were passivated in 20 mL min^{-1} of 1% O_2/He for at least 6 hrs. Catalysts will be referred to as $\text{M}/\text{Mo}_2\text{C}$, where the M denotes the metal promoter.

2.2.2 Physical Catalyst Characterization

Powder X-ray diffraction (XRD) patterns were collected using a Rigaku MiniFlex600 diffractometer with a $\text{Cu K}\alpha$ ($\lambda = 1.54 \text{ nm}$) radiation source (40 kV, 15 mA) and a Ni filter. Diffraction patterns were collected in the 2θ range of $10\text{-}90^\circ$ with a scan rate of 5° min^{-1} and a step size of 0.02° . The materials were supported on a glass sample

holder with a 0.2 mm recessed sample area and were pressed into the recession with a glass slide to obtain a uniform z-axis height. Rietveld refinement was performed in JADE using reference patterns for orthorhombic β -Mo₂C (JCPDF 00035-0787) and cubic α -MoC_{1-x} (JCPDF 00-015-0457).

The catalyst surface areas were measured by N₂ physisorption using a Micromeritics ASAP 2020 Surface Area and Porosity Analyzer. Before these measurements, the materials were degassed under vacuum (<5 mmHg) at 350 °C for 4 h. The surface areas were determined using the Brunauer-Emmett-Teller (BET) method.

Relative metal loading was determined using Inductively Coupled Plasma-Optical Emission Spectroscopy (ICP-EOS) with a Varian 710-ES. For each sample, 15 mg of catalyst material was dissolved in 3 mL of aqua regia (3:1 HCl:HNO₃) for at least 24 hrs. Then, 1 mL of the solution was diluted with 13 mL of deionized water. The solution was analyzed by a Varian 710-ES ICP Optical Emission Spectrometer and compared to standard samples of Mo, Fe, Co, Rh, Pd, K, and Ni.

2.2.3 Activity and Selectivity Measurements

The crotonaldehyde conversion rate and selectivity measurements were carried out in a 10 mm O.D. quartz U-tube fixed bed reactor. For each experimental run, ca. 100 mg of catalyst sample was diluted with 200 mg of low surface area silicon carbide and supported on a quartz wool plug (~35mg) inside the reactor. The catalyst was diluted with inactive silicon carbide to maintain a constant bed height, minimize temperature gradients in the bed, and to avoid problems with axial dispersion. The reactor was maintained at atmospheric pressure throughout pre-treatment and reaction measurements.

Prior to the experiments, the catalysts were pretreated in 15% CH₄/H₂ at 590 °C for 4 h. Previous work has shown that this pretreatment removes the passivation layer on the surface of the catalyst and activates the catalyst [18]. The catalysts were then cooled to 150 °C before being heated to 350 °C in UHP N₂. Once at the initial reaction temperature, the feed gas mixture was introduced to the reactor. The catalyst was maintained at the initial temperature for 6 hrs to accommodate for catalyst deactivation, and then maintained at each sequential temperature (275°C, 325°C, 300°C, 350°C) for 3 hrs to allow the catalyst to stabilize.

For the reactant mixture, H₂ and N₂ both passed through mass flow controllers (Brooks 5850 and Omega FMA5400/5500 mass flow controllers, respectively) and then were mixed and passed through two sequential bubblers kept at 0°C. The first bubbler contained crotonaldehyde and the second was empty, in order to maintain a constant concentration of crotonaldehyde in the reactant mixture. The reactant mixture consisted of 0.7 mol% crotonaldehyde, 4.2 mol% H₂, and 95.1% N₂ (50 mL min⁻¹ total flow). The H₂/carbon molar ratio (6) was chosen to achieve approximately 2 times the stoichiometric amount of H₂ required for complete saturation and deoxygenation of crotonaldehyde to butane. The reactant mixture then flowed to the reactor, which was enclosed in a programmable furnace.

The feed lines to the reactor and to the gas chromatograph were heated to 200°C to ensure that all feed and product components remained in the gas phase. The concentration of feed components and products were analyzed using an SRI 8610C gas chromatograph (GC) equipped with a thermal conductivity detector and a flame ionization detector.

Selectivity, S_i , was defined as:

$$S_i = \frac{C_i}{\sum_j C_j}$$

where C_i was the concentration of the product in the reactor effluent stream as measured by GC, and j is the total number of products detected. Since the carbon number was the same for all products (4), the carbon selectivity is equal to the selectivity.

2.3. Results

2.3.1 Physical Catalyst Characterization

X-ray diffractions results shown in Figure 2.1 indicate that all catalysts were confirmed to be of a mixture of α -MoC_{1-x} and β -Mo₂C carbide phases, with no detectable bulk oxide phase. Also, no peaks corresponding to the metal promoters were detected, suggesting they did not crystallize on the catalyst surface. This likely indicates that the metal promoters are well-dispersed on the catalyst surface, consistent with other findings [4]. BET surface area as determined with N₂ physisorption measurements and the measured metal content from ICP are shown in Table 2.1.

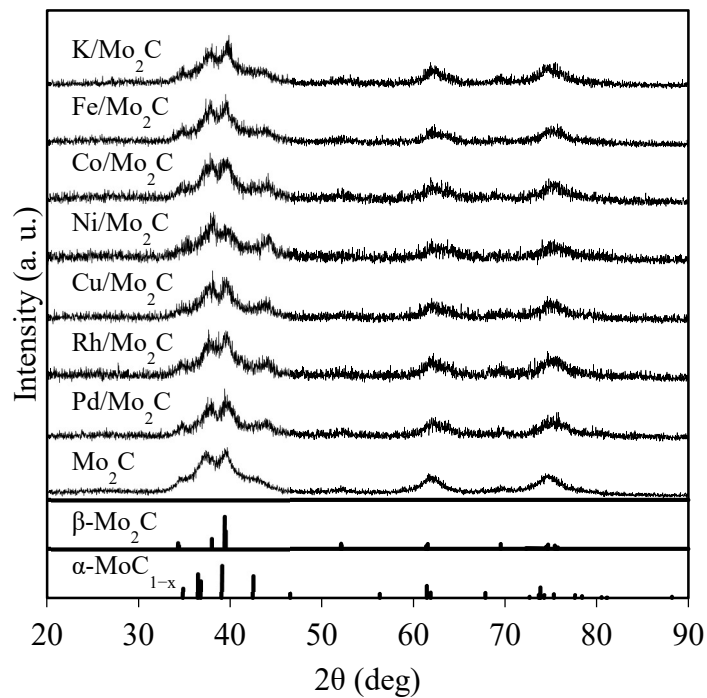


Figure 2.1. X-ray diffraction spectra of metal/Mo₂C and Mo₂C catalysts.

Table 2.1. Target and measured metal loadings, and surface areas of catalysts.

Catalyst	Monolayer Coverage (%)	Target Loading (wt%)	Measured Loading (wt%)	Surface Area (m ² /g)
K/Mo ₂ C	10	0.7		135
Fe/Mo ₂ C	10	0.9		69
Co/Mo ₂ C	10	1.0	1.0 ± 0.1	115
Ni/Mo ₂ C	10	1.0		117
Cu/Mo ₂ C	10	1.1	0.8 ± 0.1	129
Rh/Mo ₂ C	10	1.7	0.6 ± 0.1	85
Pd/Mo ₂ C	10	1.8		114
Mo ₂ C	N/A	N/A		104

2.3.2 Activity

First, the Mears criterion Weisz-Prater criterion were evaluated to determine

whether the effects of mass transfer and diffusion could be neglected. The Mears criterion is a dimensionless number which characterizes the effects of external mass transfer, and is a function of the measured rate of reaction, $-r'_A(obs)$, the bulk density of the catalyst, ρ_b , the catalyst particle radius, R , the reaction order, n , the mass transfer coefficient, k_C , and the bulk reactant concentration, C_{Ab} :

$$MR = \frac{-r'_A(obs)\rho_b R n}{k_C C_{Ab}}$$

In 1974, Mears suggested that when $MR < 0.15$, the effects of external mass transfer can be neglected [19]. $-r'_A(obs)$ was experimentally observed; ρ_b , R , and C_{Ab} were experimentally measured. k_C is a function of the Sherwood number, Sh , the diffusivity, D_{AB} , and the catalyst particle radius, R . D_{AB} was calculated by the Fuller semi-empirical method [20]. Sh is a function of the Colburn J factor, J_D , Reynolds number, Re , and Schmidt number, Sc :

$$Sh = (J_D)(Re)(Sc)^{1/3}$$

And J_D can be determined from a correlation for mass transfer to a packed bed [21]:

$$\phi J_D = 0.453 Re^{0.453}$$

The fluid viscosity was estimated as a mixture of H₂ and N₂ [22], since it was expected that the effects of crotonaldehyde (<1 mol %) would be negligible. For the experimental conditions studied, $MR < 10^{-5}$ for $n < 2$, and thus, it can be assumed that the effects of external mass transfer are negligible.

The Weisz-Prater criterion was calculated to determine whether the effects of internal diffusion could be neglected. The dimensionless number is a function of the measured rate of reaction, $-r'_A(obs)$, the catalyst pellet density, ρ_C , the catalyst particle

radius, R , the effective diffusivity, D_e , and the surface reactant concentration, C_{As} :

$$C_{WP} = \frac{-r'_A(obs)\rho_c R^2}{D_e C_{As}}$$

If the Weisz-Prater criterion is significantly less than 1, the effects of internal diffusion can be neglected [23]. $-r'_A(obs)$ was experimentally observed; ρ_c and R were experimentally measured; C_{As} was approximated as C_{Ab} since the Mears criterion showed that external mass transfer effects were negligible. D_e can be calculated from ε , the void fraction, D_{AB} , the diffusivity, and τ , the tortuosity:

$$D_e = \frac{\varepsilon D_{AB}}{\tau}$$

where ε is experimentally measured by N_2 physisorption and τ is estimated from typical values for catalysts. For the experimental conditions studied, $C_{WP} < 10^{-5}$ for all cases, so it can be assumed that the effects of internal diffusion are negligible.

Catalyst deactivation was analyzed for 6 hr TOS at 350 °C. Normalized activity profiles for each catalyst were compared where:

$$a(t) = \frac{rate(t)}{initial\ rate}$$

All catalysts showed significant deactivation during the deactivation period, losing 63-82% of their initial activity, as shown in **Figure 2.2**. Mo_2C , Rh/Mo_2C , Co/Mo_2C , and Pd/Mo_2C all showed the least amount of deactivation, while Cu/Mo_2C , Ni/Mo_2C , and K/Mo_2C showed the most significant deactivation. Each catalyst deactivation profile was fit to several known deactivation models in order to determine the applicability of various

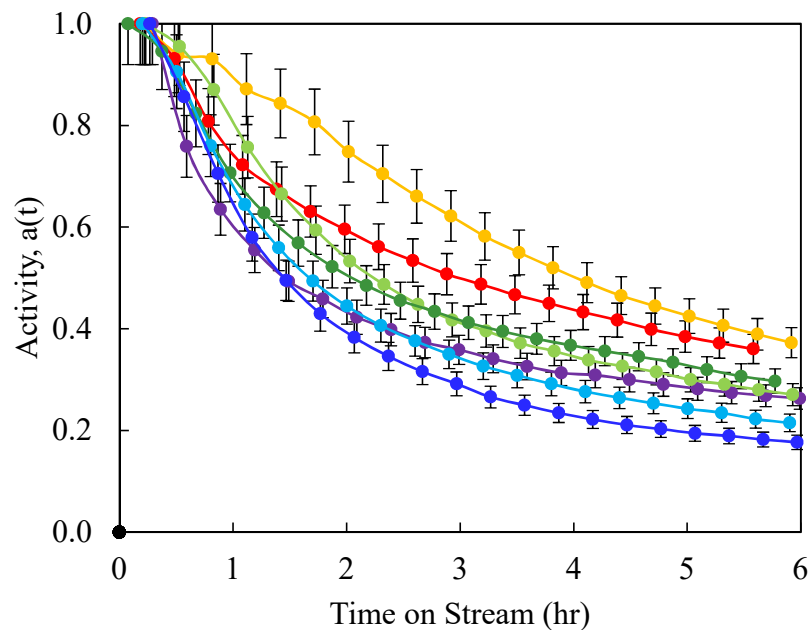


Figure 2.2. Activity decay for crotonaldehyde conversion during initial time on stream for Mo_2C (\bullet), $\text{Rh}/\text{Mo}_2\text{C}$ ($\color{red}\bullet$), $\text{Co}/\text{Mo}_2\text{C}$ ($\color{orange}\bullet$), $\text{Pd}/\text{Mo}_2\text{C}$ ($\color{green}\bullet$), $\text{Fe}/\text{Mo}_2\text{C}$ ($\color{lightgreen}\bullet$), $\text{Cu}/\text{Mo}_2\text{C}$ ($\color{cyan}\bullet$), $\text{Ni}/\text{Mo}_2\text{C}$ ($\color{blue}\bullet$), and $\text{K}/\text{Mo}_2\text{C}$ ($\color{purple}\bullet$).

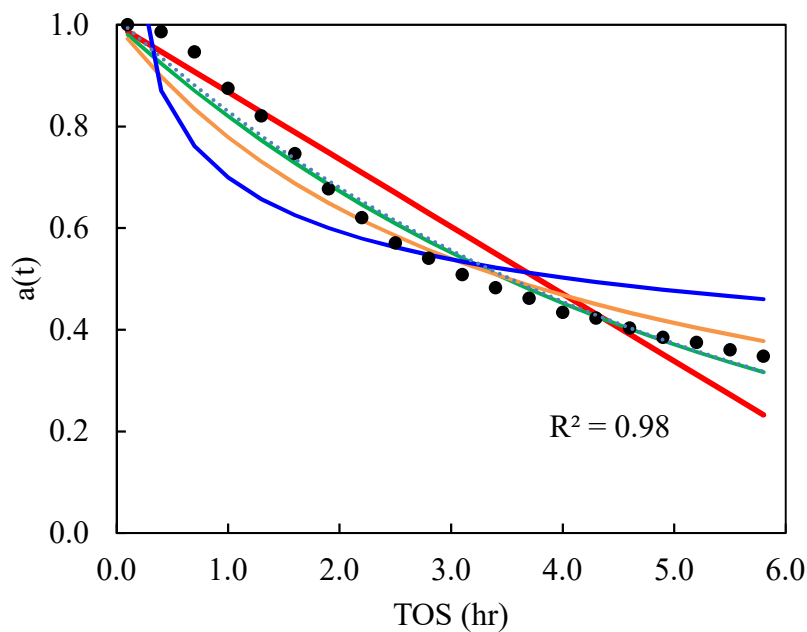


Figure 2.3. Activity $a(t)$ data for Mo_2C (\bullet) as a function of time on stream with line regression results for linear ($-$), exponential ($-$), hyperbolic ($-$), and reciprocal decay models ($-$).

deactivation mechanisms including linear, exponential, hyperbolic, and reciprocal models.

An example for Mo₂C is shown in Figure 2.3. The forms of these models are given in Table 2.2, and R²_{adj} and the fitted parameters are shown in Table 2.3. Here, k_d is the specific decay constant and t is the time on stream. The exponential model was the best fit for the most catalysts (four), but hyperbolic gave the best fit overall, with R²_{adj} > 0.925 for all catalysts. Exponential decay has been attributed to deactivation by poisoning [24], while hyperbolic decay has been attributed to deactivation by sintering [21], and it is likely that both decay mechanisms play a role in the deactivation of all catalysts. For the catalysts that had stronger correlations with the exponential decay model (Mo₂C, Co/Mo₂C, Ni/Mo₂C, and Pd/Mo₂C) than the hyperbolic decay model, it may be that sintering is not as prevalent or significant as compared to the sintering of the other metals (K/Mo₂C, Fe/Mo₂C, Cu/Mo₂C, and Rh/Mo₂C). In particular, Cu and Fe are known to be sensitive to sintering above 300 °C [1,6,25]. Interestingly, the only catalyst for which the best fit was not hyperbolic or exponential was K/Mo₂C; the best fit for this catalysts was the reciprocal model, which is consistent with deactivation by carbon deposition, or coking [26,27]. This is surprising because potassium has previously been observed to stabilize Ni/Al₂O₃ catalysts for steam reforming and Fe_xO_y catalysts for styrene synthesis by reducing coke formation [28–30].

Table 2.2. Nonlinear regression models for catalyst activity decay.

Type	Linear	Exponential	Hyperbolic	Reciprocal
Differential Form	$-\frac{da}{dt} = k_d a$	$-\frac{da}{dt} = k_d a$	$-\frac{da}{dt} = k_d a^2$	$-\frac{da}{dt} = k_d A_0^{\frac{1}{5}} a^m$
Integral Form	$a = 1 - k_d t$	$a = d^{-k_d t}$	$a = \frac{1}{1 + k_d t}$	$a = A_0 t^{-k_d}$

Table 2.4. BET surface areas and apparent activation energies of Mo₂C catalysts.

Catalyst	Surface Area (m ² /g)	Apparent Activation Energy (kcal/mol)
Mo ₂ C	104	11 ± 2
Rh/Mo ₂ C	85	14 ± 2
Co/Mo ₂ C	115	15 ± 2
Pd/Mo ₂ C	114	11 ± 2
Fe/Mo ₂ C	69	12 ± 5
Cu/Mo ₂ C	129	12 ± 2
Ni/Mo ₂ C	117	12 ± 2
K/Mo ₂ C	125	12 ± 2

Table 2.3. Results from nonlinear regression of activity data to four empirical decay rate laws.

Catalyst	Linear		Exponential		Hyperbolic		Reciprocal		
	R ² _{adj}	k _d (hr ⁻¹)	R ² _{adj}	k _d (hr ⁻¹)	R ² _{adj}	k _d (hr ⁻¹)	R ² _{adj}	k _d (hr ⁻¹)	A ₀
Mo ₂ C	0.91	0.13	0.97	0.20	0.94	0.28	0.70	0.24	0.70
K/Mo ₂ C	0.04	0.16	0.77	0.32	0.95	0.57	1.00	0.44	0.59
Fe/Mo ₂ C	0.60	0.15	0.91	0.27	0.98	0.44	0.81	0.26	0.59
Co/Mo ₂ C	0.98	0.12	0.98	0.16	0.93	0.22	0.76	0.27	0.78
Ni/Mo ₂ C	0.42	0.18	0.94	0.39	0.93	0.71	0.94	0.54	0.55
Cu/Mo ₂ C	0.55	0.17	0.94	0.33	0.96	0.58	0.90	0.43	0.58
Rh/Mo ₂ C	0.70	0.14	0.93	0.21	0.98	0.33	0.91	0.29	0.68
Pd/Mo ₂ C	0.76	0.15	0.96	0.26	0.94	0.42	0.86	0.39	0.66

Crotonaldehyde conversion rates were used to construct the Arrhenius plot shown in Figure 2.4 for Mo₂C and Mo₂C-based catalysts. Rh/Mo₂C is the most active catalyst per surface area, and Ni/Mo₂C and K/Mo₂C are the least active catalysts per surface area. The apparent activation energies of the catalysts are approximately equal for all catalysts, as shown in

Table 2.4. Pd/Mo₂C and Mo₂C have the smallest apparent activation energies, while Rh/Mo₂C and Co/Mo₂C have the highest apparent activation energies. These values are

small but compare well to literature; Ammari et. al reported activation energy of 5.0 kcal/mol for crotonaldehyde hydrogenation at 80°C on Pt/ZnO catalyst, and Raab and Lercher reported activation energies between 3.3 and 18.2 kcal/mol for crotonaldehyde hydrogenation with Pt-Ni/TiO₂ catalysts also at 80°C [31,32].

Rates were also analyzed when normalized by total catalyst weight, moles of Mo₂C support, and moles of metal promoter. In all cases, there was still a range between all rates of at least two orders of magnitudes. Crotonaldehyde conversion rates normalized per mole of metal on catalyst surface is shown in Figure 2.5.

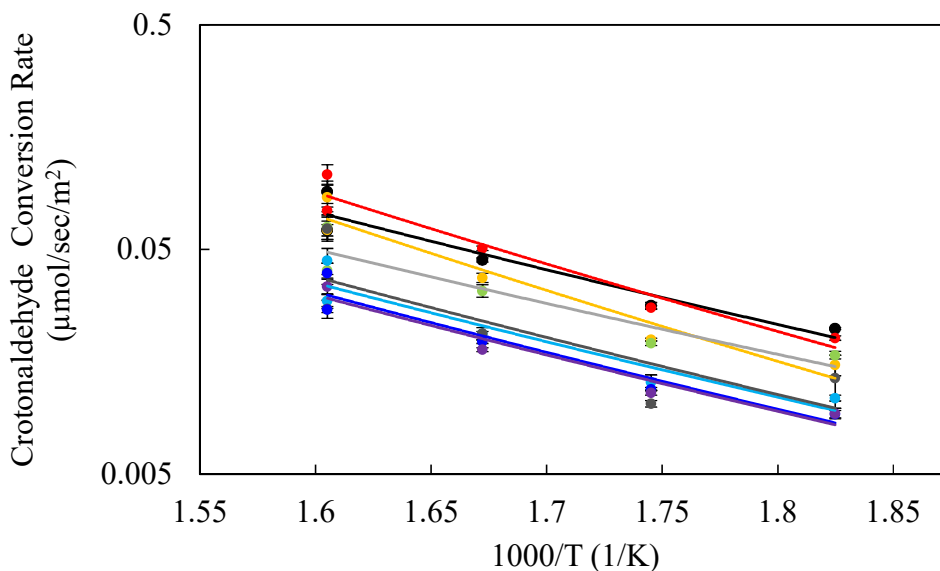


Figure 2.4. Arrhenius plot for crotonaldehyde conversion of Mo₂C (•), Rh/Mo₂C (•), Co/Mo₂C (•), Pd/Mo₂C (•), Fe/Mo₂C (•), Cu/Mo₂C (•), Ni/Mo₂C (•), and K/Mo₂C (•). All conversion rates are normalized by catalyst surface areas.

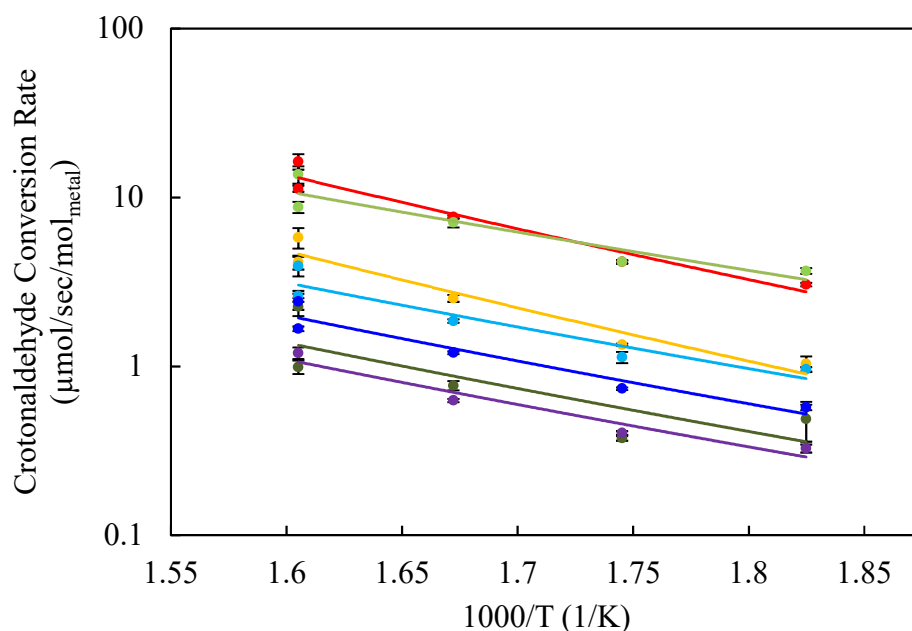


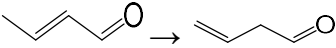
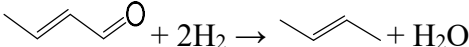
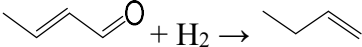
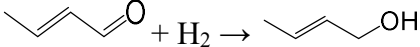
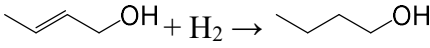
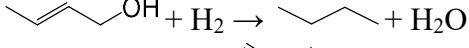
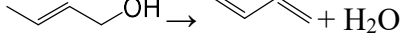
Figure 2.5. Arrhenius plot for crotonaldehyde conversion of Rh/Mo₂C (•), Co/Mo₂C (◐), Pd/Mo₂C (◑), Fe/Mo₂C (◒), Cu/Mo₂C (◔), Ni/Mo₂C (◕), and K/Mo₂C (◖). All conversion rates are normalized by moles of metal promoter on catalyst surface.

2.3.3 Selectivity

For all catalysts, four distinct products were observed via GC: butadiene, butene, butyraldehyde, and 3-butenal. Possible reaction pathways for observed and expected products are shown in Table 2.5. Butadiene and butene (both in blue) will be called HDO products because the overall reaction from crotonaldehyde to these products is HDO; butyraldehyde is referred to as a hydrogenation product; and 3-butenal is named as an isomerization product. Selectivity changed substantially during the initial TOS, as shown in the example for Mo₂C in Figure 2.6. Butyraldehyde and 3-butenal undergo an induction

period, and selectivity increases during the deactivation phase, even as catalyst activity is decreasing. Meanwhile, butene and butadiene activity decrease during initial TOS in a similar trend as the overall conversion. A similar induction period was observed for all catalysts.

Table 2.5. Possible primary and secondary reaction pathways of crotonaldehyde.

Primary Reaction Pathways	Reaction Class	Equation
	Isomerization	(17)
	Hydrodeoxygenation (HDO)	(18)
	Hydrogenation	(19)
	Hydrogenation	(20)
Secondary Reaction Pathways		
	Hydrogenation	(21)
	Hydrodeoxygenation (HDO)	(22)
	Dehydration	(23)

Comparison of selectivity between different catalysts was made using the selectivity measured at 350°C after 6 hr TOS, computed from the average of the last three GC measurements taken. The selectivity results are shown in Figure 2.7 by increasing size of transition metal promoters with the alkali promoter added at the end. Rh/Mo₂C, Pd/Mo₂C, and Co/Mo₂C did not give significantly different selectivity than Mo₂C. Ni/Mo₂C and Cu/Mo₂C gave slightly increased selectivity for isomerization, while Fe/Mo₂C gave increased selectivity for isomerization and HDO and very low selectivity to hydrogenation. K/Mo₂C gave very increased selectivity for isomerization and hydrogenation while suppressing HDO. Overall, for each product type, Mo₂C gave the

highest selectivity to hydrogenation, Fe/Mo₂C gave the highest selectivity to HDO products, and K/Mo₂C gave the highest selectivity to isomerization products.

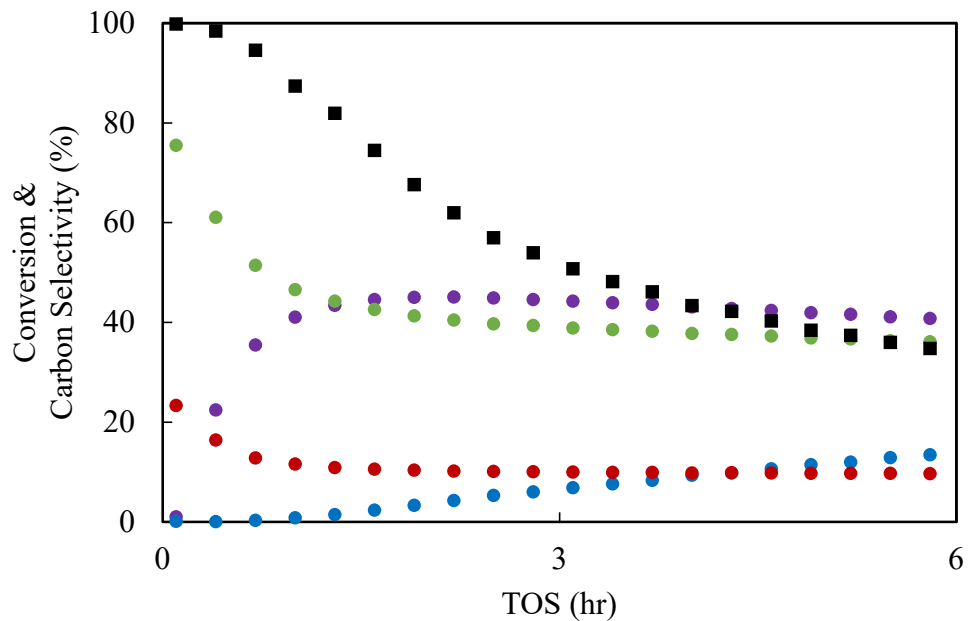


Figure 2.6. Crotonaldehyde conversion (■) and carbon selectivity of butyraldehyde, butene, 3-butenal, and butadiene for Mo₂C during deactivation period at 350 °C.

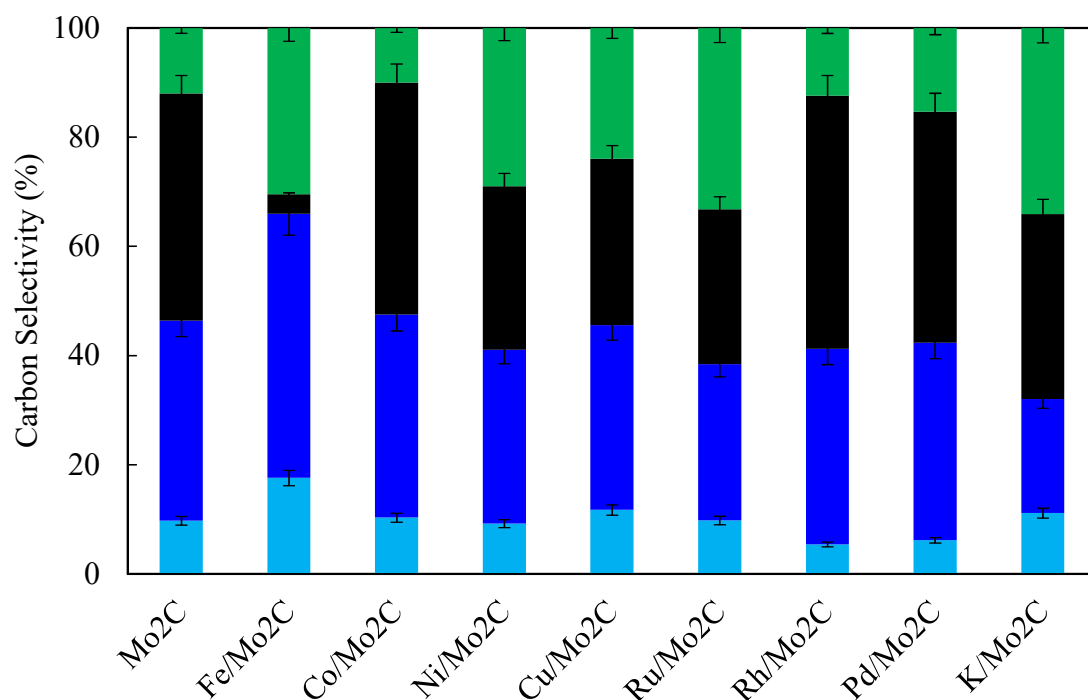


Figure 2.7. Carbon selectivity for ■butadiene, ■butene, ■butyraldehyde, and ■3-butenal, products from crotonaldehyde conversion at 350°C after 6 hr TOS on Mo₂C catalysts.

2.4. Discussion

For K, Co, Ni, Cu, and Pd promotion, the BET surface area was not statistically significantly different than the surface area of Mo₂C, given the known range of BET surface area for Mo₂C produced from the synthesis methods. Wyvratt similarly reported that low loadings of Co and Ni promotion of Mo₂C did not change the surface area [16]. For Fe and Rh, the small amount of promoter metal (.1 ML) reduced the surface area of Mo₂C by ca. 20%. Fe promotion and its effects on surface area will be explored further in Chapter 5.

Analysis of the deactivation profiles suggested that sintering and poisoning may each be sources of deactivation. Sintering is of particular concern because it is effectively

irreversible, and the initial activity cannot be regenerated. From the deactivation data, the mechanism of sintering cannot be determined, but would be a useful area for further research. Self-poisoning has been reported as a source of deactivation for crotonaldehyde hydrogenation over clay-supported Pt catalysts, and also for cinnamaldehyde (another α,β -unsaturated aldehyde) hydrogenation over supported Cu catalysts [33,34]. In these cases, selectivity of products also changed drastically during initial deactivation, suggesting a buildup of an intermediate on the catalyst surface. Similar substantial changes are seen in the selectivity during deactivation of the Mo_2C -supported catalysts, as shown in the example in Figure 2.6, strengthening the conclusion that self-poisoning is a source of deactivation for these catalysts. HDO products are initially formed at higher selectivities, so oxygen may be building up on the surface and preventing access to HDO sites, and in turn shifting the selectivity to non-deoxygenated products. Specifically, the HDO active sites may undergo self-poisoning by oxygen, allowing for increased productivity of hydrogenation and isomerization products over time.

Changes in crotonaldehyde conversion rate, when normalized by surface area, were all within one order of magnitude. All promoter metals depressed the conversion rate, with the rates for Rh/ Mo_2C within error of the rates for Mo_2C . In general, the period 5 promoter metals (Rh and Pd) experienced less reduction in conversion rate than the smaller promoter metals. This could be because the period 5 metals are physically larger than the period 4 promoter metals, and either disperse differently on the surface or preferentially settle in larger pores. Though the period 5 metals are approximately twice as large as the period 4 metals by molecular weight, recent work by Cordero et. al. suggests that the covalent atomic radius of Rh (1.42 Å) and Pd (1.39 Å) are only ca. 10% larger than Fe (1.32 Å i.s.,

1.52 Å h.s.¹), Co (1.26 Å l.s., 1.50 Å h.s.), and Ni (1.24 Å). Of course, the metals do not necessarily exist in their atomic state on the catalyst surface, and most likely exist in clusters or particles instead of as individual atoms. For the case of Pt/Mo₂C, Pt was found to deposit in “raft-like” particle structures, mostly 20-40 Å in size [35]. And for low surface area Mo₂C, it was hypothesized that large, heterogeneous Co particles form on the surface and reduce to metallic Co during pre-treatment [5]. The most obvious exception to the periodic trend was Co/Mo₂C, which had rates with magnitude between Rh/Mo₂C and Pd/Mo₂C. Co and Fe may each exist in either low or high spin states, and this result is consistent with Co being predominantly in the h.s. state with larger radius, and Fe being predominantly in the l.s. state with smaller radius. Co(II) is known to be dominated by h.s. complexes.

One reason that promoter metals may decrease the crotonaldehyde conversion rate is because they eliminate active sites on the surface of the catalyst; an increase in conversion rate would have instead suggested the promoter metals create new active sites on the surface. If promoter metals selectively eliminated or poisoned active sites, the selectivity would be different for the metal-promoted Mo₂C catalysts compared to the base case, Mo₂C catalyst.

In fact, selectivity did change for some of the promoted catalysts. First, Co/Mo₂C, Rh/Mo₂C, and Pd/Mo₂C did not have significantly different selectivities than Mo₂C. This is a similar trend to that found for conversion rates, for which these three promoted catalysts

¹ Low spin state (l.s.) and high spin state (h.s.)

had the most similar crotonaldehyde conversion rates to Mo₂C. Together, this suggests that Co, Rh, and Pd do not synergistically interact with Mo₂C to change the activity or selectivity. It is consistent with the hypothesis that these metals unselectively block active sites on the surface but do not contribute to any activity on the Mo₂C surface. However, the metals themselves as Co/SiO₂ [36], Rh/SiO₂ [37], and Pd/SiO₂ [38] are active for gas-phase crotonaldehyde hydrogenation. When studied on various supports, Pd selectivity was very support-sensitive, giving highest selectivity to dibutyl ether and *n*-butyl alcohol depending on the support [38]. Consequently, it would be expected that these metals would, at the very least, provide additive activity, since they are known to be active. Further investigation is warranted to understand how these metals deposit on the Mo₂C and what role (if any) they play in this reaction.

Ni/Mo₂C, Cu/Mo₂C, and Ru/Mo₂C, and K/Mo₂C had increased selectivity to isomerization, mostly at the expense of hydrogenation selectivity. Fe/Mo₂C showed very low selectivity to hydrogenation, with increased isomerization and HDO selectivity. Both K/Mo₂C and Fe/Mo₂C gave very low selectivity for butyraldehyde, suggesting that they have a high affinity for hydrogenating the C=O bond.

2.5. Summary

Selectivity was measured at four temperatures: 275°C, 300°C, 325°C, and 350°C. For most catalysts, the selectivity at different temperatures was not significantly different, so comparison of selectivity across catalysts was made for the initial selectivity at 350°C after 6 hrs TOS. Rh/Mo₂C, Pd/Mo₂C, and Co/Mo₂C did not give significantly different selectivity than Mo₂C. For Rh and Co, this agrees with other analysis, since deactivation

and rate data for these catalysts were also very similar to Mo₂C. Ni/Mo₂C and Cu/Mo₂C gave slightly increased selectivity for 3-butenal, while Fe/Mo₂C gave increased selectivity for 3-butenal and butene, and K/Mo₂C gave very high selectivity for 3-butenal. K/Mo₂C and Fe/Mo₂C gave very low selectivity for butyraldehyde, suggesting that they have a high affinity for hydrogenation of the C=O bond.

2.6. References

- [1] Y. Chen, S. Choi, L. T. Thompson, Low Temperature CO₂ Hydrogenation to Alcohols and Hydrocarbons over Mo₂C Supported Metal Catalysts, *Journal of Catalysis* 343 (2016) 147–156. doi:10.1016/j.jcat.2016.01.016.
- [2] N. Wang, K. Fang, M. Lin, D. Jiang, D. Li, Y. Sun, Synthesis of Higher Alcohols from Syngas over Fe/K/ β -Mo₂C Catalyst, *Catalysis Letters* 136 (2010) 9–13. doi:10.1007/s10562-010-0288-1.
- [3] M. Xiang, D. Li, H. Xiao, J. Zhang, H. Qi, W. Li, B. Zhong, Y. Sun, Synthesis of Higher Alcohols from Syngas over Fischer–Tropsch Elements Modified K/ β -Mo₂C Catalysts, *Fuel* 87 (2008) 599–603. doi:10.1016/j.fuel.2007.01.041.
- [4] J. A. Schaidle, N. M. Schweitzer, O. T. Ajenifujah, L. T. Thompson, On the Preparation of Molybdenum Carbide-Supported Metal Catalysts, *Journal of Catalysis* 289 (2012) 210–217. doi:10.1016/j.jcat.2012.02.012.
- [5] A. Griboval-Constant, J.-M. Giraudon, G. Leclercq, L. Leclercq, Catalytic Behaviour of Cobalt or Ruthenium Supported Molybdenum Carbide Catalysts for FT Reaction, *Applied Catalysis A: General* 260 (2004) 35–45. doi:10.1016/j.apcata.2003.10.031.
- [6] J. A. Schaidle, Carbide and Nitride Based Catalysts for Synthesis Gas Conversion, Ph. D. Thesis, University of Michigan, 2011.
- [7] T. G. Kelly, J. G. Chen, Controlling C–O, C–C and C–H Bond Scission for Deoxygenation, Reforming, and Dehydrogenation of Ethanol Using Metal-Modified Molybdenum Carbide Surfaces, *Green Chem.* 16 (2014) 777–784. doi:10.1039/C3GC41259H.
- [8] X. Zhang, X. Zhu, L. Lin, S. Yao, M. Zhang, X. Liu, X. Wang, Y.-W. Li, C. Shi, D. Ma, Highly Dispersed Copper over β -Mo₂C as an Efficient and Stable Catalyst for the Reverse Water Gas Shift (RWGS) Reaction, *ACS Catalysis* 7 (2017) 912–

918. doi:10.1021/acscatal.6b02991.

- [9] S. Posada-Pérez, P. J. Ramírez, R. A. Gutiérrez, D. J. Stacchiola, F. Viñes, P. Liu, F. Illas, J. A. Rodríguez, The Conversion of CO₂ to Methanol on Orthorhombic β-Mo₂C and Cu/β-Mo₂C Catalysts: Mechanism for Admetal Induced Change in the Selectivity and Activity, *Catalysis Science & Technology* 6 (2016) 6766–6777. doi:10.1039/C5CY02143J.
- [10] J.-L. Dubois, K. Sayama, H. Arakawa, CO₂ Hydrogenation over Carbide Catalysts, *Chemistry Letters* (1992) 5–8.
- [11] M. J. Ledoux, C. P. Huu, J. Guille, H. Dunlop, Compared Activities of Platinum and High Specific Surface Area Mo₂C and WC Catalysts for Reforming Reactions I. Catalyst Activation and Stabilization: Reaction of n-Hexane, *Journal of Catalysis* 134 (1992) 383–398. doi:10.1016/0021-9517(92)90329-G.
- [12] K. Y. Park, W. K. Seo, J. S. Lee, Selective Synthesis of Light Olefins from Syngas over Potassium-Promoted Molybdenum Carbide Catalysts, *Catalysis Letters* 11 (1991) 349–356. doi:10.1007/BF00764327.
- [13] J. S. Lee, S. Kim, Y. G. Kim, Electronic and Geometric Effects of Alkali Promoters in CO Hydrogenation over K/Mo₂C Catalysts, *Topics in Catalysis* 2 (1995) 127–140.
- [14] C. Pistonesi, A. Juan, A. P. Farkas, F. Solymosi, Effects of Potassium on the Adsorption of Methanol on β-Mo₂C(001) Surface, *Surface Science* 604 (2010) 914–919. doi:10.1016/j.susc.2010.02.020.
- [15] A. Kotarba, G. Adamski, W. Piskorz, Z. Sojka, C. Sayag, G. Djéga-Mariadassou, Modification of Electronic Properties of Mo₂C Catalyst by Potassium Doping: Impact on the Reactivity in Hydrodenitrogenation Reaction of Indole, *The Journal of Physical Chemistry B* 108 (2004) 2885–2892. doi:10.1021/jp037105j.
- [16] B. M. Wyvratt, Examination of Property-Reactivity Relationships of Early Transition Metal Carbides and Nitrides as Catalysts and Catalytic Supports, Ph. D. Thesis, University of Michigan, 2016.
- [17] C. N. Satterfield, Heterogeneous catalysis in industrial practice, 2nd ed, McGraw-Hill, New York, 1991.
- [18] T. E. King, Carbide and nitride supported water-gas shift catalysts, Ph. D. Thesis, University of Michigan, 2007.
- [19] D. E. Mears, Tests for Transport Limitations in Experimental Catalytic Reactors, *Industrial & Engineering Chemistry Research Process Design and Development* 10 (1971) 541–547.

- [20] E. N. Fuller, P. D. Schettler, J. C. Giddings, New Method for Prediction of Binary Gas-Phase Diffusion Coefficients, *Industrial & Engineering Chemistry* 58 (1966) 19–27.
- [21] H. S. Fogler, *Elements of Chemical Reaction Engineering*, 5th ed., Prentice Hall, New Jersey, 2016.
- [22] C. R. Wilke, A Viscosity Equation for Gas Mixtures, *The Journal of Chemical Physics* 18 (1950) 517–519. doi:10.1063/1.1747673.
- [23] P. B. Weisz, C. D. Prater, Interpretation of Measurements in Experimental Catalysis, in: *Advances in Catalysis*, Elsevier, 1954: pp. 143–196. doi:10.1016/S0360-0564(08)60390-9.
- [24] C. H. Bartholomew, R. J. Farrauto, *Fundamentals of Industrial Catalytic Processes*, 2nd ed., John Wiley & Sons, New Jersey, 2006.
- [25] R. Farrauto, S. Hwang, L. Shore, W. Ruettinger, J. Lampert, T. Giroux, Y. Liu, O. Ilinich, New Material Needs for Hydrocarbon Fuel Processing: Generating Hydrogen for the PEM Fuel Cell, *Annual Review of Materials Research* 33 (2003) 1–27. doi:10.1146/annurev.matsci.33.022802.091348.
- [26] C. G. Rudershausen, C. C. Watson, Variables Affecting Activity of Molybdena-Alumina Hydroforming Catalyst in Aromatization of Cyclohexane, *Chemical Engineering Science* 3 (1954) 110–121. doi:10.1016/0009-2509(54)80016-9.
- [27] A. Voorhies, Carbon Formation in Catalytic Cracking, *Industrial & Engineering Chemistry* 37 (1945) 318–322. doi:10.1021/ie50424a010.
- [28] T. Borowiecki, A. Denis, M. Rawski, A. Gołębiowski, K. Stołecki, J. Dmytrzyk, A. Kotarba, Studies of Potassium-Promoted Nickel Catalysts for Methane Steam Reforming: Effect of Surface Potassium Location, *Applied Surface Science* 300 (2014) 191–200. doi:10.1016/j.apsusc.2014.02.053.
- [29] D. H. Choi, J. E. Park, D. H. Kim, E. D. Park, Steam Reforming of Ethylene Glycol over Ni-Based Catalysts: The Effect of K, *Research on Chemical Intermediates* 42 (2016) 223–235. doi:10.1007/s11164-015-2322-9.
- [30] O. Shekhah, R. Wolfgang, R. Schlögl, Styrene Synthesis: In Situ Characterization and Reactivity Studies of Unpromoted and Potassium-Promoted Iron Oxide Model Catalysts, *Journal of Catalysis* 225 (2004) 56–68. doi:10.1016/j.jcat.2004.03.024.
- [31] F. Ammari, J. Lamotte, R. Touroude, An Emergent Catalytic Material: Pt/ZnO Catalyst for Selective Hydrogenation of Crotonaldehyde, *Journal of Catalysis* 221 (2004) 32–42. doi:10.1016/S0021-9517(03)00290-2.

- [32] C. G. Raab, J. A. Lercher, Activity and Selectivity of PtNi/TiO₂ Catalysts for Hydrogenation of Crotonaldehyde, *Catalysis Letters* 18 (1992) 99–109.
- [33] A. Chambers, S. David Jackson, D. Stirling, G. Webb, Selective Hydrogenation of Cinnamaldehyde over Supported Copper Catalysts, *Journal of Catalysis* 168 (1997) 301–314. doi:10.1006/jcat.1997.1683.
- [34] I. Kun, G. Szöllösi, M. Bartók, Crotonaldehyde Hydrogenation over Clay-Supported Platinum Catalysts, *Journal of Molecular Catalysis A: Chemical* 169 (2001) 235–246. doi:10.1016/S1381-1169(00)00566-5.
- [35] N. M. Schweitzer, J. A. Schaidle, O. K. Ezekoye, X. Pan, S. Linic, L. T. Thompson, High Activity Carbide Supported Catalysts for Water Gas Shift, *Journal of the American Chemical Society* 133 (2011) 2378–2381. doi:10.1021/ja110705a.
- [36] E. L. Rodrigues, J. M. C. Bueno, Co/SiO₂ Catalysts for Selective Hydrogenation of Crotonaldehyde II: Influence of the Co Surface Structure on Selectivity, *Applied Catalysis A: General* 232 (2002) 147–158. doi:10.1016/S0926-860X(02)00090-X.
- [37] P. Reyes, M. C. Aguirre, J. L. G. Fierro, G. Santori, O. Ferretti, Hydrogenation of Crotonaldehyde on Rh-Sn/SiO₂ Catalysts Prepared by Reaction of Tetrabutyltin on Prereduced Rh/SiO₂ Precursors, *Journal of Molecular Catalysis A: Chemical* 184 (2002) 431–441. doi:10.1016/S1381-1169(02)00031-6.
- [38] N. Iwasa, M. Takizawa, M. Arai, Palladium-Based Alloy and Monometallic Catalysts for Gas Phase Hydrogenation of Crotonaldehyde: Effects of Alloying and Alloy Crystallite Size, *Applied Catalysis A: General* 283 (2005) 255–263. doi:10.1016/j.apcata.2005.01.015.

CHAPTER 3

Selectivity of biomass model compound upgrading over K-promoted Mo₂C

3.1. Introduction

As demonstrated in the first chapter, some metal promoters of Mo₂C can be used to manipulate the selectivity of bio-oil upgrading. Still, more highly selective catalysts are desired. To design more highly selective catalysts, this chapter seeks to understand the mechanism by which K changes the selectivity of upgrading. Then, this mechanistic understanding can be exploited to increase or repress that effect. The addition of alkali metals has been reported to significantly shift the selectivities of early transition metal carbide and nitride catalysts [1–3]. For several hydrogenation reactions, K addition to Mo₂C has been shown to shift the selectivity from paraffins to olefins and reduce methane selectivity from >40% to ca. 20% at similar extents of conversion for CO hydrogenation at atmospheric pressure [1]. Solymosi and Bugyi reported that K addition to a Mo₂C/Mo(100) surface increased the rate of adsorption and binding energy of CO₂, a proxy for measuring the base site concentration [2]. Vo et al. also found that K addition to Mo₂C/Al₂O₃ increased base site concentration; the extent of this increase was greater than that for Na, Ce, or Co dopants [3]. Potassium addition has also been broadly evaluated as a modifier for other catalytic materials [4–6]. For example, alkali addition to an MgO catalyst increased the activity for 2-propanol conversion and shifted the selectivities for

dehydration and dehydrogenation products.

Mo₂C catalysts have been demonstrated to selectively deoxygenate biomass pyrolysis model compounds (e.g., alcohols, acids, and oxygenated aromatics) [7–15], but very little research has focused on modifying Mo₂C to target selective hydrogenation and C-C bond formation.

The focus of research described in this chapter was to determine the effect of K modification on the selectivity of Mo₂C for reactions relevant to biomass pyrolysis vapor upgrading. Acetic acid and crotonaldehyde were chosen as model compounds as they represent a simple carboxylic acid and aldehyde, respectively, possess multiple functionalities, and can undergo a variety of transformations, allowing for multiple reaction pathways to be probed. In addition, aldehydes and carboxylic acids are prevalent in pyrolysis vapors (up to 13 and 25 wt%, respectively) [16] and contribute to the degradation and instability of bio-oils [9]. Here, we observed that the addition of K to Mo₂C narrowed the product distributions for AA and CR upgrading in the presence of excess H₂.

3.2. Experimental Methods

3.2.1 Catalyst Synthesis

The Mo₂C was synthesized by the methods described in Section 2.2.1. To avoid oxidation prior to K impregnation, the Mo₂C was transferred in a 15% CH₄/H₂ atmosphere to a water-tolerant, oxygen-free glovebox (N₂ atmosphere). Potassium was added to the Mo₂C by incipient wetness using K₂CO₃ (Sigma Aldrich, 99%) solutions. The amount of K₂CO₃ was adjusted to correspond to the equivalent of 0.1, 0.3, 0.5, 0.7, and 1.1 equivalent monolayers (ML) of surface coverage, assuming a total site concentration of 10¹⁹ sites m⁻²

[17]. The catalyst was transferred back to the synthesis reactor under an Ar atmosphere. The resulting catalyst was dried at 110 °C for 2 h in H₂, then reduced in H₂ at 450 °C for 4 h. After quenching to room temperature, the catalyst was passivated using a 1% O₂/He mixture for at least 6 h. The catalysts were named based on the nominal amount of K addition (in terms of ML), so K(1.1ML)/Mo₂C represents a Mo₂C catalyst with 1.1 ML of K addition.

MgO material (Sigma-Aldrich, ≥99% trace metal basis, 325 mesh) was crushed, and sieved to 125–250 μm.

3.2.2 Physical Catalyst Characterization

Powder X-ray diffraction (XRD) patterns and relative metal loadings were collected using the same methods described in Section 2.2.2.

Nitrogen physisorption isotherms were collected on a Micromeritics 3Flex after degassing the sample at 350 °C for 4 hours, and the free space was measured after analysis. Pore distributions were determined using non-local density functional theory for slit pore geometry based on the *Heterogeneous Surface – 2D – Nonlocal Density Functional Theory* model [18,19] by applying the algorithm in Micromeritics' MicroActive software. The DFT data was fitted by LOESS, a generalization of the locally weighted scatterplot smoothing (LOWESS) method with $\alpha = 0.05$.

3.2.3 Activity and Selectivity Measurements

Crotonaldehyde conversion experiments were performed in the same manner as described in Section 2.2.3.

The acetic acid conversion experiments were performed by Connor P. Nash at the National Renewable Energy Laboratory. These experiments were also performed in a flow reactor system equipped with a bubbler to introduce acetic acid vapor, and the reactor effluent was analyzed with a gas chromatograph. Ca. 50 mg of catalyst was mixed with ca. 200 mg of quartz chips (300-425 μm , calcined prior to use in air at 500 $^{\circ}\text{C}$ for 12 h) and supported on a quartz wool plug in a quartz u-tube reactor. The diluent was used to mitigate axial dispersion and localized thermal effects, and to prevent channeling. Prior to the upgrading experiments, the Mo_2C catalysts were pretreated in 15% CH_4/H_2 at 590 $^{\circ}\text{C}$ for 4 h while the MgO was pretreated in 1% O_2/He at 500 $^{\circ}\text{C}$ for 2 h. The catalysts were then cooled to 150 $^{\circ}\text{C}$ before being heated to 350 $^{\circ}\text{C}$ in 2.5% H_2/He . The reaction mixture consisted of 0.4 mol% acetic acid, 2.4 mol% H_2 , and 97.2% He (ca. 55 mL min^{-1} total flow). The H_2/carbon molar ratio (6) was chosen to achieve approximately 2 times the stoichiometric amount of H_2 required for complete saturation and deoxygenation of acetic acid to ethane. The reactor was maintained at 350 $^{\circ}\text{C}$ for 6 h.

The selectivities are reported as carbon selectivities:

$$\textit{Selectivity}_j = \frac{(\textit{carbon \#}) * (\textit{molar rate of production})_j}{\sum_{\textit{all products}} (\textit{carbon \#}) * (\textit{molar rate of production})} \quad (3.1)$$

The rates, including conversion rates and product formation rates, were normalized by the surface areas. Conversion rates were calculated by the difference in the concentration of the model compound before reaction versus during reaction:

$$\textit{Conversion rate} = \frac{(X) * (\dot{n}_{in})}{(m_{cat}) * (SA_{cat})} \quad (3.2)$$

where X is the conversion of the model compound; \dot{n}_{in} is the molar flowrate of the model compound in the feed, as determined by vapor-liquid equilibrium; m_{cat} is the catalyst

loading in the reactor; and SA_{cat} is the surface area of the catalyst. Product formation rates were calculated by the amount of product detected via GC:

$$\text{Product formation rate} = \frac{C_{out} * \dot{V}}{m_{cat} * SA_{cat}} \quad (3.3)$$

where C_{out} is the concentration of the model compound in the reactor outlet; \dot{V} is the total volumetric flowrate through the reactor. Previous reports with the acetic acid reactor system have suggested the systematic standard error in selectivity values to be $\pm 2\%$ [7]; however, based on deviation from stoichiometric ratios of acetone/ CO_2 , the data in this study may be as high as $\pm 4\%$, as there were no significant quantities of CO detected to suggest reverse water gas shift reactions influenced the expected stoichiometric yields of acetone and CO_2 . Error bars represent 95% confidence interval, based on the determined standard error.

3.3. Results

3.3.1 Physical Catalyst Characterization

X-ray diffraction patterns for the as-synthesized materials are shown in Figure 3.1. Rietveld refinement indicated that the catalysts were comprised of nearly equal amounts of cubic α - MoC_{1-x} ($x = ca. 0.5$) and orthorhombic β - Mo_2C (

Table 3.1). There are no apparent oxide peaks, indicating complete carburization of the precursor. Additionally, the handling and passivation procedures avoided bulk oxidation of the carbide during transfers between the reactor and the glovebox. The XRD patterns and the relative amounts of α - MoC_{1-x} and β - Mo_2C are comparable to those reported for catalysts produced using similar synthesis procedures [20,21]. Given the Mo:C

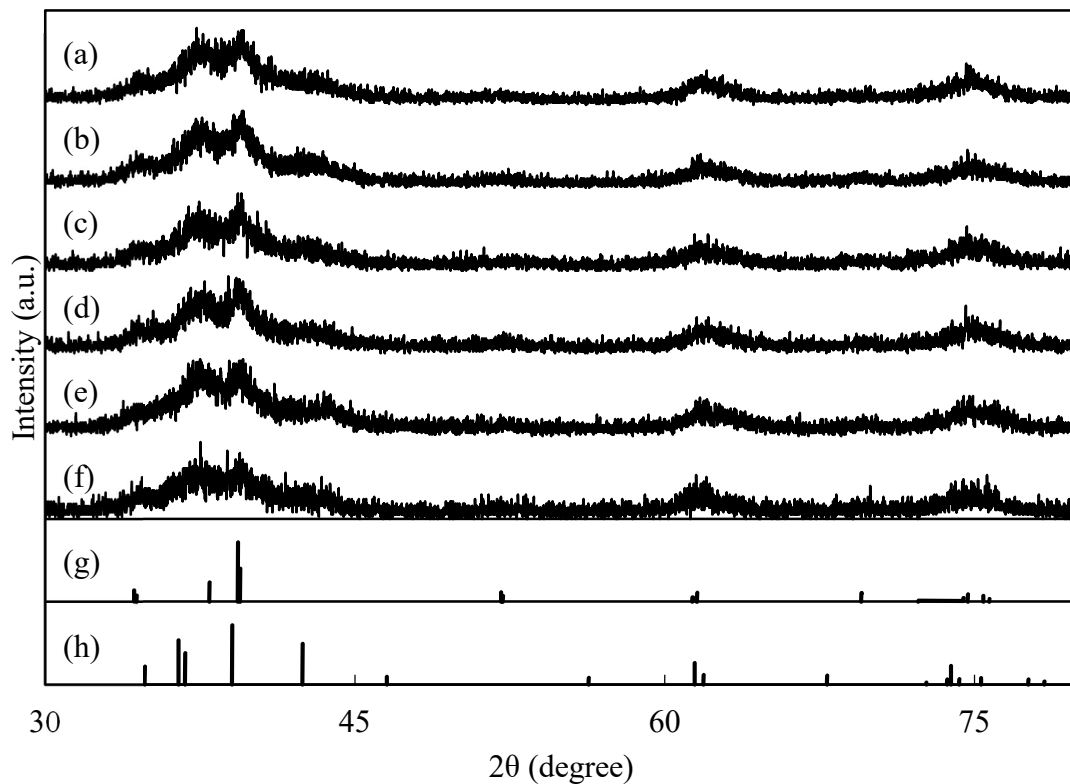


Figure 3.1. X-ray diffraction patterns for (a) K(1.1ML)/Mo₂C, (b) K(0.7ML)/Mo₂C, (c) K(0.5ML)/Mo₂C, (d) K(0.3ML)/Mo₂C, (e) K(0.1ML)/Mo₂C, and (f) Mo₂C catalysts and peak positions for polycrystalline (g) orthorhombic β-Mo₂C (JCPDF 00035-0787) and (h) cubic α-MoC_{1-x} (JCPDF 00-015-0457).

ratio, these materials will be referred to as Mo₂C.

The surface area of the parent Mo₂C material was 108 m² g⁻¹ (**Table 3.2**). The addition of K caused a decrease in the surface area to as low as 31 m² g⁻¹ for the K(1.1ML)/Mo₂C material. This decrease can be attributed almost entirely to a reduction in the micropore structure, as evidenced by the decreased in micropore volume and surface area shown in **Table 3.2**; the mesopore volume and surface areas are relatively similar across all K loadings. The pore volume distribution shown in Figure 3.2 elucidates that the main region for reduction in surface area is from the reduction in pores in the 10-20 Å

region.

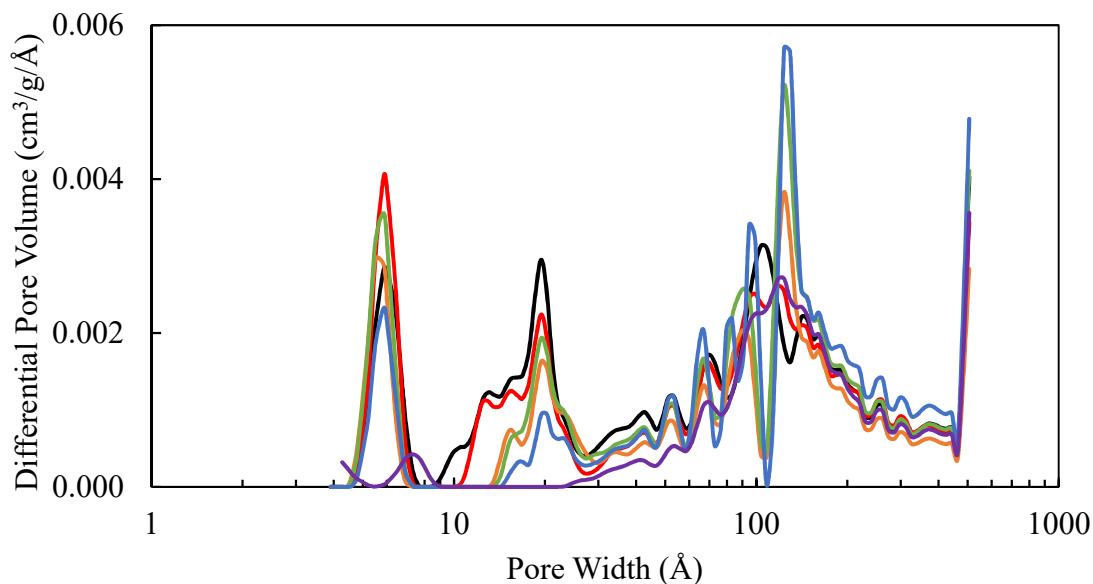


Figure 3.2. DFT pore volume distribution for Mo₂C (–), K(0.1ML)/Mo₂C (–), K(0.3ML)/Mo₂C (–), K(0.5ML)/Mo₂C (–), K(0.7ML)/Mo₂C (–), and K(1.1ML)/Mo₂C (–).

Table 3.1. Reitveld refinement results for Mo₂C-based catalysts.

Catalyst	α -MoC _{1-x} (wt %)	β -Mo ₂ C (wt %)
Mo ₂ C	58.8	41.2
K(0.1ML)/Mo ₂ C	47.2	52.8
K(0.3ML)/Mo ₂ C	55.2	44.8
K(0.5ML)/Mo ₂ C	47.3	52.8
K(0.7ML)/Mo ₂ C	56.9	43.1
K(1.1ML)/Mo ₂ C	58.5	41.5

Table 3.2. Measured metal content and surface area for all catalysts.

	BET Surface Area (m ² g ⁻¹)	DFT Micropore Surface Area (m ² g ⁻¹)	DFT Mesopore Surface Area (m ² g ⁻¹)	DFT Micropore Volume (cm ³ g ⁻¹)	DFT Mesopore Volume (cm ³ g ⁻¹)
MgO	130				
Mo ₂ C	125	80	25	0.037	0.095
K(0.1ML)/ Mo ₂ C	113	85	21	0.035	0.088
K(0.3ML)/ Mo ₂ C	76	59	20	0.021	0.077
K(0.5ML)/ Mo ₂ C	88	67	23	0.024	0.097
K(0.7ML)/ Mo ₂ C	58	39	21	0.013	0.102
K(1.1ML)/ Mo ₂ C	24	10	13	0.003	0.074

3.3.2 Activity

Activity data for the first 6 hr TOS was fit to generalized power law expressions to better characterize the deactivation of the catalysts for both acetic acid and crotonaldehyde conversion. The generalized power law expressions model assumes that as the activity decays, it asymptotically approaches a non-zero value. As outlined by Fuentes [22], the model seeks to fit the deactivation data with the following equation:

$$-\frac{da}{dt} = Q(T, C)(a - a_s)^n$$

where a is an activity parameter; $Q(T, C)$ is a global kinetic term that is a function of T , temperature and C , reactant concentration; a_{ss} is the steady-state catalyst activity; and n is the deactivation order. For a catalyst operated in a flow reactor under differential conditions in the kinetic regime with $n = 1$:

$$\ln(X - X_S) = \ln\left(\left[\frac{W}{F}\right]N - X_S\right) - Qt$$

where X is a measure of conversion; X_S is the steady-state measure of conversion; W is a measure of the amount of catalyst; and F is the molar flowrate of the limiting reactant (here, the model compound). For $n = 2$:

$$(X - X_S)^{-1} = \left(\left[\frac{W}{F}\right]N - X_S\right)^{-1} + \left(\left[\frac{W}{F}\right]N\right)^{-1} Qt$$

which leads to, for $n = 1$:

$$X = \left(\left[\frac{W}{F}\right]N - X_S\right) \exp(-Qt) + X_S$$

and for $n = 2$:

$$X = \left[\left(\left[\frac{W}{F} \right] N - X_s \right)^{-1} + \frac{Qt}{\left[\frac{W}{F} \right] N} \right]^{-1} + X_s$$

Linear regression was performed to minimize the residuals of the data and the model for n=1 and n=2 for each catalyst. Results are shown in Table 3.4.

Other studies with Mo₂C catalysts have found varying results for long-term stability; Mortenson et. al. [23] found 1-octanol and phenol HDO conversion to decrease by ca. 50% after 76 hr TOS, while Ren et. al. [24] found acetone HDO activity and selectivity to have negligible changes after 18 hr TOS. Mo₂C stability is often related to oxidation of the surface and bulk to MoO₂, and additional investigations of the reaction

Table 3.3. Regression results and R² for GPL model fits for the deactivation data of acetic acid upgrading with Mo₂C-based catalysts.

	n=1				n=2			
	[W/F]N	X _s	Q ₁	R ²	[W/F]N	X _s	Q ₂	R ²
Mo ₂ C	0.9	0.25	0.005	0.96	0.3	0.25	0.000	-0.96
K(0.1ML)/Mo ₂ C	0.9	0.19	0.014	0.97	0.5	0.19	0.011	0.76
K(0.3ML)/Mo ₂ C	0.4	0.03	0.024	0.90	0.1	0.03	0.001	0.66
K(0.5ML)/Mo ₂ C	0.4	0.09	0.011	0.89	0.1	0.09	0.003	0.19
K(0.7ML)/Mo ₂ C	0.4	0.15	0.005	0.97	0.2	0.15	0.000	-1.54
K(1.1ML)/Mo ₂ C	0.7	0.4	0.005	0.93	0.5	0.4	0.008	-1.23

Table 3.4. Regression results and R² for GPL model fits for the deactivation data of crotonaldehyde upgrading with Mo₂C-based catalysts.

	n=1				n=2			
	[W/F]N	X _s	Q ₁	R ²	[W/F]N	X _s	Q ₂	R ²
Mo ₂ C	1.00	0.23	0.012	0.95	1.00	0.23	0.04	0.74
K(0.1ML)/Mo ₂ C	0.61	0.14	0.014	0.90	1.00	0.17	0.16	0.83
K(0.3ML)/Mo ₂ C	0.23	0.06	0.014	0.82	0.49	0.07	0.25	0.96
K(0.5ML)/Mo ₂ C	0.23	0.10	0.012	0.89	1.00	0.11	0.58	0.90

conditions that promote or inhibit this oxidation are required.

The consumption rates of acetic acid and H₂ and acetic acid conversions over each catalyst at 6 h time on stream (TOS) at 350 °C are presented in

Table 3.5. Minima in the rates and conversions were observed for the K(0.3ML)/Mo₂C catalyst, while the K(1.1ML)/Mo₂C catalyst displayed the highest acetic acid consumption rate and an acetic acid conversion equal to the parent Mo₂C catalyst. All the conversions over the Mo₂C catalysts were less than 25%.

Table 3.5. Consumption rates and conversions for acetic acid conversion at 350 °C and 3 h TOS for all catalysts.

	AA consumption rate ($\mu\text{mol m}^{-2} \text{min}^{-1}$)	H ₂ consumption rate ($\mu\text{mol m}^{-2} \text{min}^{-1}$)	H ₂ :AA consumption rate ratio	Conversion (%)
MgO	0.84	0.000	0.0	64
Mo ₂ C	0.34	0.97	2.8	23
K(0.1ML)/Mo ₂ C	0.37	0.035	1.0	17
K(0.3ML)/Mo ₂ C	0.025	0.065	2.6	1
K(0.5ML)/Mo ₂ C	0.23	0.087	0.4	9
K(0.7ML)/Mo ₂ C	0.60	0.000	0.0	21
K(1.1ML)/Mo ₂ C	1.2	0.047	0.0	23

^aSum of the carbon selectivity to CO, CH₄, ethane, propane, and propylene.

Table 3.6. Consumption rates and conversions of crotonaldehyde upgrading at 350 °C and 6 h TOS for all catalysts.

Catalyst	CR Consumption rate ($\mu\text{mol m}^{-2} \text{min}^{-1}$)	Estimated H ₂ consumption rate ($\mu\text{mol m}^{-2} \text{min}^{-1}$)	H ₂ :CR consumption ratio	Conversion (%)
MgO	0.61	0.17	0.28	16
Mo ₂ C	3.2	0.5	0.16	23
K(0.1ML)/Mo ₂ C	3.1	1.2	0.39	15
K(0.3ML)/Mo ₂ C	1.5	0.2	0.13	7
K(0.5ML)/Mo ₂ C	2.3	0.2	0.09	10
K(0.7ML)/Mo ₂ C	3.1	0.3	0.10	12
K(1.1ML)/Mo ₂ C	9.2	1.2	0.13	19

The crotonaldehyde and H₂ consumption rates, and crotonaldehyde conversions are listed in Table 3.6. A minimum in the crotonaldehyde consumption rate was observed for the K(0.3ML)/Mo₂C catalyst, while the maximum consumption rate occurred for the K(1.1ML)/Mo₂C catalyst. This is the same trend that was observed for acetic acid upgrading. The H₂ consumption rate could not be measured directly in this experimental setup but was estimated by accounting for the H₂ needed to produce the products. The

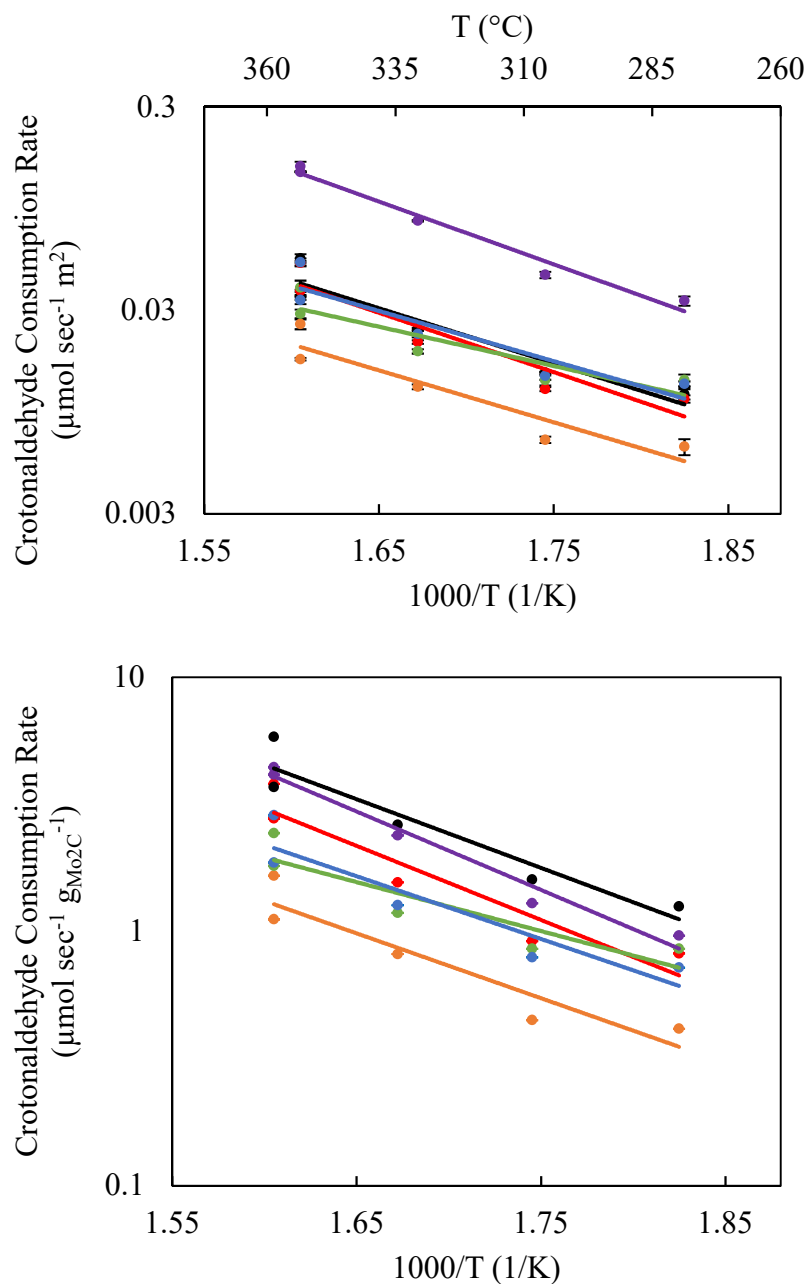


Figure 3.3. Arrhenius plot with crotonaldehyde consumption rate normalized by surface area (top) and by weight of Mo_2C (bottom) of Mo_2C (\bullet), $\text{K}(0.1\text{ML})/\text{Mo}_2\text{C}$ ($\color{red}\bullet$), $\text{K}(0.3\text{ML})/\text{Mo}_2\text{C}$ ($\color{orange}\bullet$), $\text{K}(0.5\text{ML})/\text{Mo}_2\text{C}$ ($\color{green}\bullet$), $\text{K}(0.7\text{ML})/\text{Mo}_2\text{C}$ ($\color{blue}\bullet$), and $\text{K}(1.1\text{ML})/\text{Mo}_2\text{C}$ ($\color{purple}\bullet$).

estimated H_2 consumption rates reached a minimum for the $\text{K}(0.3\text{ML})/\text{Mo}_2\text{C}$ catalyst;

however, unlike the acetic acid results, proceeded to increase to a maximum for the K(1.1ML)/Mo₂C catalyst.

The crotonaldehyde consumption rates between 275-350 °C are shown in the Arrhenius plot in Figure 3.3. When normalized by surface area, the rates for Mo₂C, K(0.1ML)/Mo₂C, K(0.5ML)/Mo₂C, and K(0.7ML)/Mo₂C are essentially equal. The conversion rates for K(1.1ML)/Mo₂C fall far above the rest, suggesting some enhancement effect on rate when K is above one full monolayer of promotion. When normalized by the amount (weight) of Mo₂C in the catalyst, the rates still all fall within an order of magnitude. All rates for the promoted catalysts are less than those for unpromoted Mo₂C, showing that for a given weight of Mo₂C support, potassium promotion reduces intrinsic activity of the support. Since the rates are mostly equivalent on a surface area basis, and the N₂ physisorption results demonstrated that K promotion reduces surface area, it follows that the apparent reduction in intrinsic activity of the support is a consequence of reduced surface area; less Mo₂C is exposed at the catalyst surface.

3.3.3 Selectivity

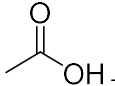
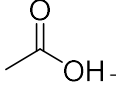
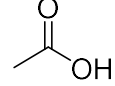
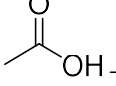
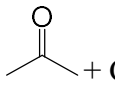
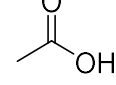
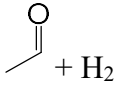
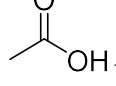
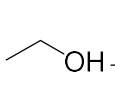
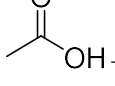
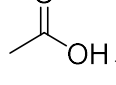
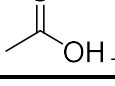
3.3.3.1 Acetic Acid Conversion

Under the conditions used in this study, acetic acid could undergo several reaction pathways including gasification, DCO, decarboxylation, ketonization, dehydration, and HDO, as illustrated in Table 3.7. Secondary reaction pathways, including CH₄ decomposition, steam reforming, and water gas shift could also occur. For promoted Mo₂C and promoted catalysts, acetaldehyde, acetone, ethylene, CO₂, CO, CH₄, ethane, propane and propylene were detected as products from acetic acid upgrading. The carbon

selectivities at 6 h TOS are presented in Table 3.8 and shown in Figure 3.4.

Carbon selectivities as a function of TOS are illustrated for Mo₂C and K(1.1ML)/Mo₂C catalysts as representative in Figure 3.6. The parent Mo₂C catalyst formed primarily acetaldehyde, while CO and CH₄ also formed in significant quantities. The selectivity to acetaldehyde and acetone shifted dramatically with the addition of K, even for loadings as low as 0.1ML.

Table 3.7. Possible primary and secondary reaction pathways of acetic acid.

Primary Reaction Pathways	Reaction Class	Equation
 $\rightarrow 2 \text{CO} + 2 \text{H}_2$	Gasification	(5)
 $+ \text{H}_2 \rightarrow \text{CO} + \text{CH}_4 + \text{H}_2\text{O}$	Decarbonylation (DCO)	(6)
 $\rightarrow \text{CO}_2 + \text{CH}_4$	Decarboxylation (DCO)	(7)
2  \rightarrow  $+ \text{CO}_2 + \text{H}_2\text{O}$	Ketonization (KET)	(8)
 $+ \text{H}_2 \rightarrow$  $+ \text{H}_2\text{O}$	Hydrodeoxygenation (HDO)	(9)
 $+ 2 \text{H}_2 \rightarrow$  $+ \text{H}_2\text{O}$	Hydrodeoxygenation (HDO)	(10)
 $+ 2 \text{H}_2 \rightarrow \text{H}_2\text{C}=\text{CH}_2 + 2 \text{H}_2\text{O}$	Hydrodeoxygenation (HDO)	(11)
 $\rightarrow \text{H}_2\text{C}=\text{C}=\text{O} + \text{H}_2\text{O}$	Dehydration	(12)
 $\rightarrow 2 \text{C} + 2 \text{H}_2\text{O}$	Dehydration	(13)
Secondary Reaction Pathways		
$\text{CH}_4 \rightarrow \text{C} + 2 \text{H}_2$	Methane decomposition	(14)
$\text{CH}_4 + \text{H}_2\text{O} \rightarrow \text{CO} + 3 \text{H}_2$	Methane steam reforming	(15)
$\text{CO} + \text{H}_2\text{O} \leftrightarrow \text{CO}_2 + \text{H}_2$	Water gas shift	(16)

The molar productivities for acetaldehyde and acetone at 6 hr TOS are presented in Figure 3.5 to further exemplify the effect of K loading on acetic acid upgrading. The productivity to acetaldehyde decreased with K loading, while the productivity to acetone

Table 3.8. Carbon selectivities (%) for acetic acid conversion at 350 °C and 3 h TOS for all catalysts.

	Acetaldehyde	Acetone	CO ₂	Ethylene	CO	CH ₄	Other ^a
MgO	0	79	21	0	0	0	0
Mo ₂ C	57	6	2	7	14	10	4
K(0.1ML)/Mo ₂ C	40	30	11	2	9	7	1
K(0.3ML)/Mo ₂ C	28	49	16	1	0	4	2
K(0.5ML)/Mo ₂ C	14	65	19	0	0	2	0
K(0.7ML)/Mo ₂ C	8	69	20	0	2	1	0
K(1.1ML)/Mo ₂ C	6	72	20	0	1	1	0

^aSum of the carbon selectivity to CO, CH₄, ethane, propane, and propylene.

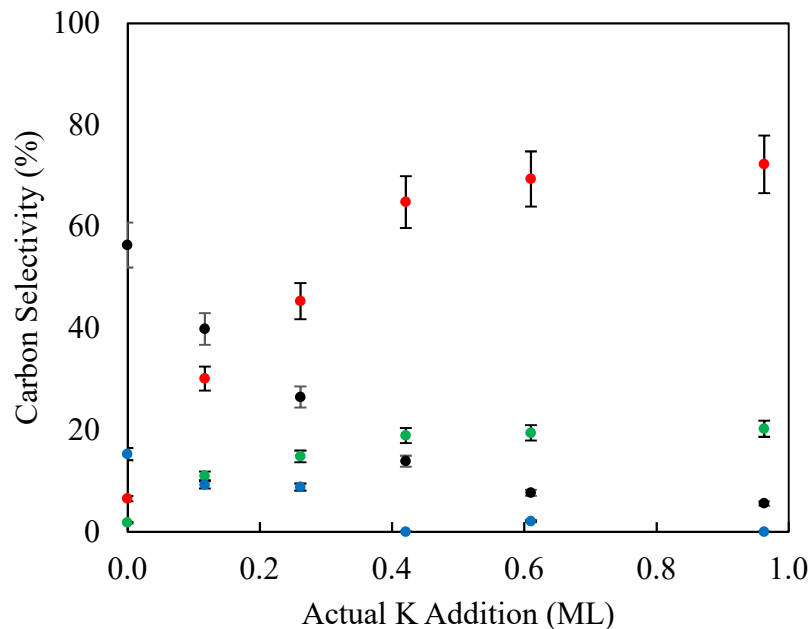


Figure 3.4. Carbon selectivities (%) of AA upgrading for acetone (•), CO (•), acetaldehyde (•), and CO₂ (•) at 350 °C with increasing K coverage of Mo₂C catalyst. Data were taken at 6 h time on stream. Error bars represent 95% confidence interval.

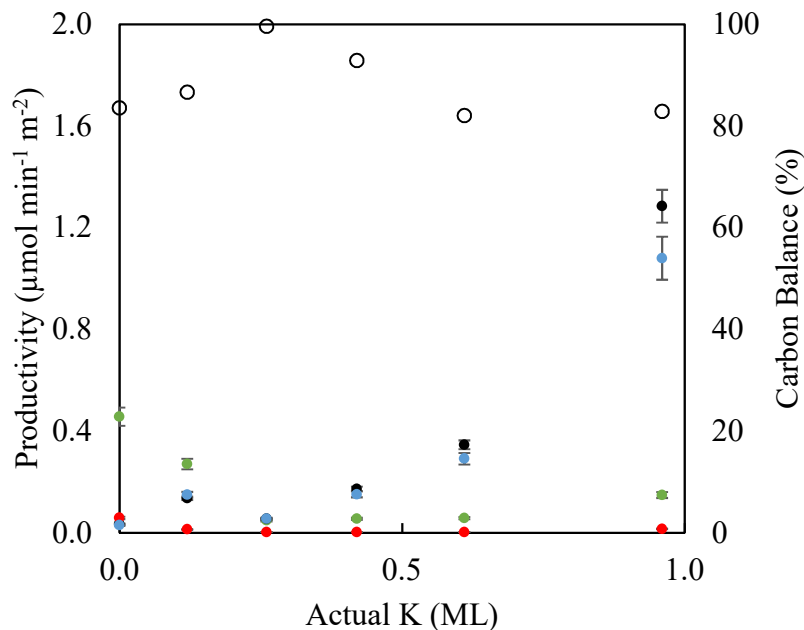


Figure 3.5. Molar productivity from acetic acid conversion of acetone (•), CO₂ (•), acetaldehyde (•), and ethylene (•) at 350 °C with increasing K coverage of Mo₂C catalyst and (o) carbon balance. Data were taken at 6 h. Error bars represent 95% confidence interval. increased. Thus, the productivity data are consistent with the increase in selectivity to

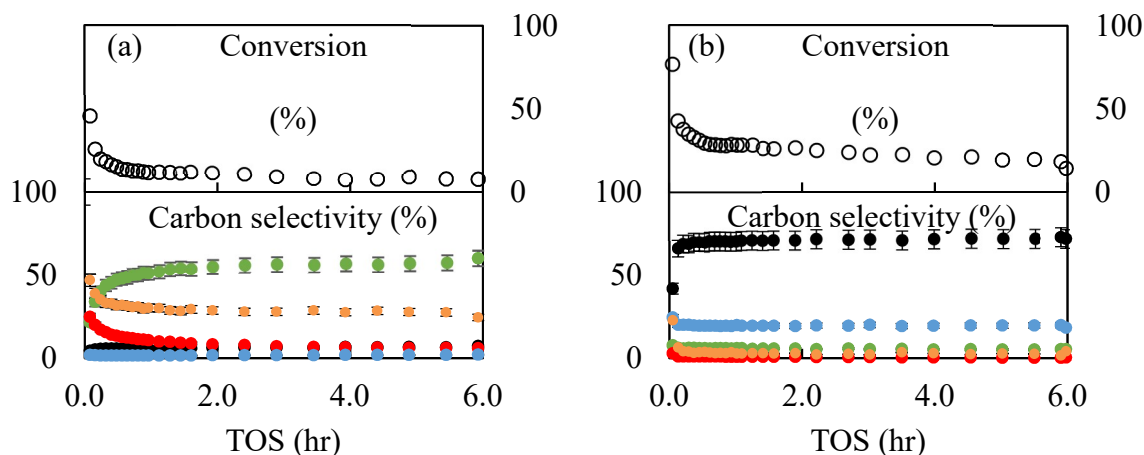


Figure 3.6. TOS carbon selectivity and conversion of (a) Mo_2C and (b) $\text{K}(1.1\text{ML})/\text{Mo}_2\text{C}$ for acetic acid upgrading for acetone (●), CO_2 (●), acetaldehyde (●), ethylene (●), and other (●). Error bars represent 95% confidence interval, based on the determined standard error of $\pm 4\%$.

acetone not being solely due to a decrease in the production of acetaldehyde, but rather from a combination of higher acetone production and lower acetaldehyde production. In general, HDO reaction pathways, such as those to form acetaldehyde and ethylene, are preferred because reactant oxygen is removed as H_2O and carbon is not lost to light gas products. Interestingly, increasing the K loading shifted the dominant reaction pathway from HDO to ketonization while also minimizing C-C bond cleavage. That is, K promotion reduced the DCO activity as indicated by the decrease in selectivity to CO and CH_4 , whereas DCO was a significant reaction pathway over the parent Mo_2C catalyst.

3.3.3.2 Crotonaldehyde Conversion

Under the conditions used in this study, crotonaldehyde could undergo several primary and secondary reaction pathways as previously discussed in Chapter 2. For promoted Mo_2C and promoted catalysts, butadiene, butenes, butyraldehyde, and 3-butenal

were detected as products from crotonaldehyde upgrading. The carbon selectivities to these products are illustrated in Figure 3.7 and shown in Table 3.9. 3-Butenal was the dominant product for all the catalysts, although its selectivity reached a maximum for the K(0.3ML)/Mo₂C catalyst. 3-Butenal is indicative of structural isomerization, which has been previously reported to occur over Mo₂C catalysts [25–27], and has often been associated with the presence of both carbide and oxide domains. In experiments where crotyl alcohol and butyraldehyde were separately co-fed with H₂ to the catalyst, 3-butenal only formed from crotyl alcohol, suggesting that crotyl alcohol may have been an intermediate.

In general, selectivities to the butenes and butadiene decreased with increasing K addition, while selectivities to butyraldehyde, a hydrogenation product, increased with K addition, with the exception of the K(0.1ML)/Mo₂C catalyst. For example, the sum of the butenes and butadiene selectivities decreased from 27% for Mo₂C to 4% for the K(0.3ML)/Mo₂C catalyst, indicating that low K loadings resulted in a significant decrease in deoxygenation (i.e., C-O cleavage), similar to that observed for acetic acid.

The crotonaldehyde upgrading molar productivities at 6 h TOS are presented in

Table 3.9. Carbon selectivities (%) of crotonaldehyde upgrading at 350 °C and 6 h TOS for all catalysts.

	Butadiene	Butenes ¹	Butyraldehyde	3-Butenal
MgO	0	4	20	76
Mo ₂ C	2	25	6	67
K(0.1ML)/Mo ₂ C	11	16	27	46
K(0.3ML)/Mo ₂ C	0	4	7	88
K(0.5ML)/Mo ₂ C	0	5	10	85
K(0.7ML)/Mo ₂ C	0	5	14	81
K(1.1ML)/Mo ₂ C	2	8	25	64

Figure 3.9. The productivities for all products increased with K loadings above 0.3ML,

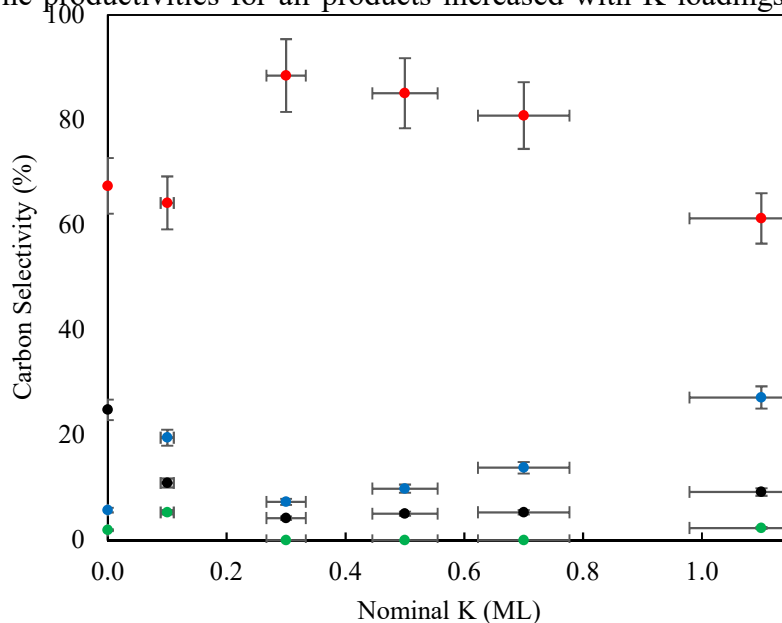


Figure 3.7. Carbon selectivities (%) crotonaldehyde for 3-butenal (•), butyraldehyde (•), butenes (•), and butadiene (•) at 350 °C with increasing K coverage of Mo₂C catalyst. Data were taken at 6 h time on stream. Error bars represent 95% confidence interval.

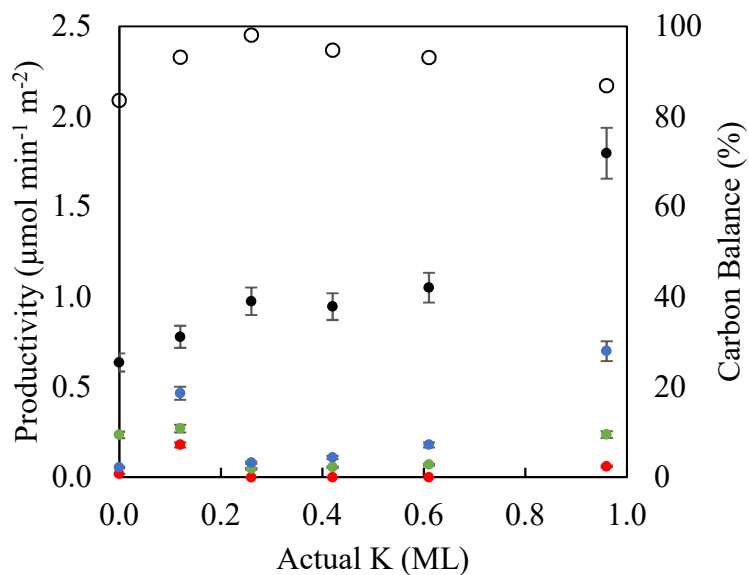


Figure 3.8. Molar productivity from crotonaldehyde conversion of 3-butenal (•), butyraldehyde (•), butene (•), and butadiene (•) at 350 °C with increasing K coverage of Mo₂C catalyst and (○) carbon balance. Data were taken at 6 h. Error bars represent 95% confidence interval.

although the productivities for 3-butenal and butyraldehyde increased more significantly. An increase in the butene, butadiene and butyraldehyde productivities implies an overall increase in the hydrogenation activity. We propose that K creates new types of active sites; if K were poisoning active sites important to the reaction mechanism, the productivity of at least one product would decrease. This hypothesis will be explored further in the following chapter. For crotonaldehyde upgrading, K does not appear to affect the available reaction pathways; instead it appears to promote isomerization and hydrogenation.

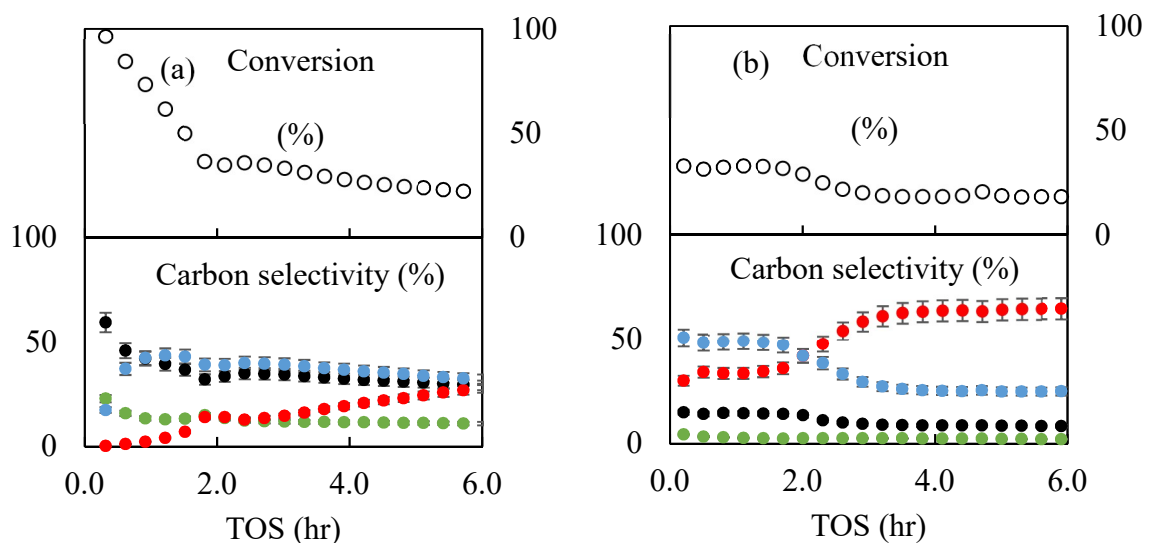


Figure 3.9. TOS carbon selectivity of (c) Mo₂C and (d) K(1.1ML)/Mo₂C for crotonaldehyde upgrading for 3-butenal (•), butyraldehyde (•), butene (•), and butadiene (•). Error bars represent 95% confidence interval, based on the determined standard error of $\pm 4\%$.

3.4. Discussion

K was found to be an effective method of eliminating micropore structure in Mo₂C catalyst, while still preserving the majority of the mesopore structure. K promotion has been found to similarly result in decreased surface area and decreased porosity for other catalysts including Fe/Mn catalysts and fused magnetite catalysts [28,29]. In these cases, it was hypothesized the presence of K induces greater crystallite sizes of the supporting catalyst during calcination which leads to decreased surface area; the Mo₂C catalyst were not calcined, but crystallite size could have increased during reduction in H₂ after incipient wetness of K. For K, reduction in surface area increased with K promotion. Therefore, either K is also physically blocking pores and therefore an increase in K increases the amount of blockage; or increase in K promotion increased the degree of structural change. This relationship between the pore structure and K promotion could be a useful tool to employ in size-selective upgrading reactions when the micropore sites need to be selectively eliminated.

In fitting the deactivation profiles to the GPL model, $n=1$ was the best overall fit for the Mo₂C and K/Mo₂C catalysts for both acetic acid and crotonaldehyde upgrading. The order of deactivation has been found to be an indicator for the mechanism of the deactivation [30,31]. First-order decay ($n=1$) was the clear best fit for acetic acid upgrading, given that the R^2 values were all positive and greater than 0.89. For acetic acid upgrading, the fitted $[W/F]N$ values trended closely with steady-state conversion, and was therefore considered a function of catalyst activity. In contrast, the deactivation constant Q_1 (a larger Q_1 indicates faster deactivation to the steady-state value), trended very differently than steady-state conversion and appeared to be independent of catalyst activity.

Instead, Q_1 could be a function on K loading. The rate of deactivation, Q_1 , initially increased with K loading up to 0.3ML and then, upon further K loading, decreased and returned to the same deactivation rate observed on Mo_2C . In Chapter 2, the deactivation profile of $\text{K}(0.1\text{ML})/\text{Mo}_2\text{C}$ was found to have a very strong correlation ($R^2 = 1.00$) to a reciprocal model, which indicated deactivating by coking. One possibility is that coking is related to the K particle size, and therefore the amount of K- Mo_2C interface; at loadings below 0.5ML, the K was likely well-dispersed on the surface, while at K loadings above 0.5ML, the K species may have agglomerated on the surface.

The best model fit ($n=1$ or $n=2$) was less clear for crotonaldehyde upgrading, in which first-order and second-order were both the best for some catalysts. For both $n=1$ and $n=2$, the fitted $[\text{W}/\text{F}]^n$ values trended closely with steady-state conversion, similarly to the trend observed for acetic acid. Also, for both first- and second-order models, the deactivation constants Q_1 and Q_2 appeared to be independent of catalyst activity, and instead were likely a function of K loading.

For acetic acid upgrading, the H_2 consumption rate could be directly measured, and was a good first clue as to the change in mechanism with K promotion. H_2 consumption was dramatically reduced with just 0.1ML of K, suggesting a difference in the dominant reaction pathways between the parent Mo_2C and $\text{K}/\text{Mo}_2\text{C}$ materials. As can be seen in Table 3.8 and Figure 3.4, catalysts with low and zero H_2 consumption rates still generated HDO products; this could be a result of H_2 generated *in situ* from other reactions such as gasification, and/or the H_2 consumption was below the detection limit of the analytical equipment.

The selectivity to acetaldehyde and acetone shifted dramatically with the addition

of K, even for loadings as low as 0.1ML. As the K loading was increased, the selectivity to acetaldehyde decreased, with a concomitant increase in acetone selectivity. The shift in selectivity from acetaldehyde to acetone and CO₂, was independent of acetic acid consumption rate (Table 3.5), and thus indicates that the primary reaction pathway shifted from HDO to ketonization as a result of K addition. In order to compare catalyst performance to a basic catalyst, MgO, was also evaluated.

The productivity to acetaldehyde decreased with K loading, while the productivity to acetone increased. Thus, the productivity data are consistent with the increase in selectivity to acetone not being solely due to a decrease in the production of acetaldehyde, but rather from a combination of higher acetone production and lower acetaldehyde production. In general, HDO reaction pathways, such as those to form acetaldehyde and ethylene, are preferred because reactant oxygen is removed as H₂O and carbon is not lost to light gas products. Interestingly, increasing the K loading shifted the dominant reaction pathway from HDO to ketonization while also minimizing C-C bond cleavage. That is, K modification reduced the DCO activity as indicated by the decrease in selectivity to CO and CH₄. As mentioned earlier, DCO was a significant reaction pathway over the parent Mo₂C catalyst.

As shown in Table 3.8 and Table 3.9, the MgO catalyst performed similarly to the K(1.1ML)/Mo₂C for both acetic acid and crotonaldehyde upgrading. For acetic acid, MgO favored the ketonization reaction pathway exclusively, and for crotonaldehyde, MgO favored isomerization and hydrogenation products. MgO is a known base catalyst, and the fact that high loadings of K caused Mo₂C to have selectivity more similar to MgO suggests that K addition increases basicity of the catalyst. This will be explored further in Chapter

4.

3.5. Summary

The addition of K to Mo₂C had a dramatic effect on the selectivities for acetic acid and crotonaldehyde upgrading in temperature ranges of interest for catalytic upgrading of biomass pyrolysis vapors. For acetic acid, the addition of K resulted in high selectivities for ketonization while subverting the HDO and DCO reaction pathways. For crotonaldehyde, the addition of K increased the selectivities to isomerization products while HDO and hydrogenation-dehydration reactions were diminished. This effect reached a maximum in selectivity between 0.5 and 0.7 ML of K.

3.6. References

- [1] K. Y. Park, W. K. Seo, J. S. Lee, Selective Synthesis of Light Olefins from Syngas over Potassium-Promoted Molybdenum Carbide Catalysts, *Catalysis Letters* 11 (1991) 349–356. doi:10.1007/BF00764327.
- [2] F. Solymosi, L. Bugyi, Effects of Potassium on the Chemisorption of CO₂ and CO on the Mo₂C/Mo(100) Surface, *Catalysis Letters* 66 (2000) 227–230.
- [3] D.-V. N. Vo, T.-H. Nguyen, E. M. Kennedy, B. Z. Dlugogorski, A. A. Adesina, Fischer–Tropsch Synthesis: Effect of Promoter Type on Alumina-Supported Mo Carbide Catalysts, *Catalysis Today* 175 (2011) 450–459. doi:10.1016/j.cattod.2011.04.045.
- [4] A. A. Lemonidou, L. Nalbandian, I. A. Vasalos, Oxidative Dehydrogenation of Propane over Vanadium Oxide Based Catalysts Effect of Support and Alkali Promoter, *Catalysis Today* (2000) 9.
- [5] L. Ronchin, L. Toniolo, Selective Hydrogenation of Benzene to Cyclohexene Catalyzed by Ru Supported Catalysts Influence of the Alkali Promoters on Kinetics, Selectivity and Yield, *Catalysis Today* (2001) 7.
- [6] G. Neri, A. M. Visco, A. Donato, C. Milone, M. Malentacchi, G. Gubitosa,

- Hydrogenation of Phenol to Cyclohexanone over Palladium and Alkali-Doped Palladium Catalysts, *Applied Catalysis A: General* 110 (1994) 49–59. doi:10.1016/0926-860X(94)80104-5.
- [7] F. G. Baddour, C. P. Nash, J. A. Schaidle, D. A. Ruddy, Synthesis of α -MoC_{1-x} Nanoparticles Using a Surface-Modified SBA-15 Hard Template and Determination of Structure-Function Relationships in Acetic Acid Deoxygenation, *Angewandte Chemie International Edition* 55 (2016) 9026–9029.
- [8] J. A. Schaidle, J. Blackburn, C. A. Farberow, C. Nash, K. X. Steirer, J. Clark, D. J. Robichaud, D. A. Ruddy, Experimental and Computational Investigation of Acetic Acid Deoxygenation over Oxophilic Molybdenum Carbide: Surface Chemistry and Active Site Identity, *ACS Catalysis* 6 (2016) 1181–1197. doi:10.1021/acscatal.5b01930.
- [9] D. A. Ruddy, J. A. Schaidle, J. R. Ferrell III, J. Wang, L. Moens, J. E. Hensley, Recent Advances in Heterogeneous Catalysts for Bio-Oil Upgrading via “Ex Situ Catalytic Fast Pyrolysis”: Catalyst Development Through the Study of Model Compounds, *Green Chemistry* 16 (2014) 454–490. doi:10.1039/C3GC41354C.
- [10] M. M. Sullivan, J. T. Held, A. Bhan, Structure and Site Evolution of Molybdenum Carbide Catalysts upon Exposure to Oxygen, *Journal of Catalysis* 326 (2015) 82–91. doi:10.1016/j.jcat.2015.03.011.
- [11] K. Xiong, W. Yu, J. G. Chen, Selective Deoxygenation of Aldehydes and Alcohols on Molybdenum Carbide (Mo₂C) Surfaces, *Applied Surface Science* 323 (2014) 88–95. doi:10.1016/j.apsusc.2014.06.100.
- [12] C.-J. Chen, W.-S. Lee, A. Bhan, Mo₂C Catalyzed Vapor Phase Hydrodeoxygenation of Lignin-Derived Phenolic Compound Mixtures to Aromatics under Ambient Pressure, *Applied Catalysis A: General* 510 (2016) 42–48. doi:10.1016/j.apcata.2015.10.043.
- [13] F. G. Baddour, V. A. Witte, C. P. Nash, M. B. Griffin, D. A. Ruddy, J. A. Schaidle, Late-Transition-Metal-Modified β -Mo₂C Catalysts for Enhanced Hydrogenation during Guaiacol Deoxygenation, *ACS Sustainable Chemistry & Engineering* 5 (2017) 11433–11439. doi:10.1021/acssuschemeng.7b02544.
- [14] W.-S. Lee, Z. Wang, R. J. Wu, A. Bhan, Selective Vapor-Phase Hydrodeoxygenation of Anisole to Benzene on Molybdenum Carbide Catalysts, *Journal of Catalysis* 319 (2014) 44–53. doi:10.1016/j.jcat.2014.07.025.
- [15] W.-S. Lee, A. Kumar, Z. Wang, A. Bhan, Chemical Titration and Transient Kinetic Studies of Site Requirements in Mo₂C-Catalyzed Vapor Phase Anisole Hydrodeoxygenation, *ACS Catalysis* 5 (2015) 4104–4114. doi:10.1021/acscatal.5b00713.

- [16] T. Milne, F. Agblevor, M. David, S. Deutch, D. Johnson, *Developments in Thermochemical Biomass Conversion*, Blackie Academic and Professional, London, U.K., 1997.
- [17] C. N. Satterfield, *Heterogeneous catalysis in industrial practice*, 2nd ed, McGraw-Hill, New York, 1991.
- [18] J. Jagiello, J. P. Olivier, 2D-NLDFT Adsorption Models for Carbon Slit-Shaped Pores with Surface Energetical Heterogeneity and Geometrical Corrugation, *Carbon* 55 (2013) 70–80. doi:10.1016/j.carbon.2012.12.011.
- [19] J. Jagiello, J. P. Olivier, Carbon Slit Pore Model Incorporating Surface Energetical Heterogeneity and Geometrical Corrugation, *Adsorption* 19 (2013) 777–783. doi:10.1007/s10450-013-9517-4.
- [20] J. A. Schaidle, L. T. Thompson, Fischer–Tropsch Synthesis over Early Transition Metal Carbides and Nitrides: CO Activation and Chain Growth, *Journal of Catalysis* 329 (2015) 325–334. doi:10.1016/j.jcat.2015.05.020.
- [21] J. A. Schaidle, N. M. Schweitzer, O. T. Ajenifujah, L. T. Thompson, On the Preparation of Molybdenum Carbide-Supported Metal Catalysts, *Journal of Catalysis* 289 (2012) 210–217. doi:10.1016/j.jcat.2012.02.012.
- [22] G. A. Fuentes, Catalyst Deactivation and Steady-State Activity: A Generalized Power-Law Equation Model, *Applied Catalysis* 15 (1985) 33–40. doi:10.1016/S0166-9834(00)81484-0.
- [23] P. M. Mortensen, H. W. P. de Carvalho, J.-D. Grunwaldt, P. A. Jensen, A. D. Jensen, Activity and Stability of Mo₂C/ZrO₂ as Catalyst for Hydrodeoxygenation of Mixtures of Phenol and 1-Octanol, *Journal of Catalysis* 328 (2015) 208–215. doi:10.1016/j.jcat.2015.02.002.
- [24] H. Ren, W. Yu, M. Saliccioli, Y. Chen, Y. Huang, K. Xiong, D. G. Vlachos, J. G. Chen, Selective Hydrodeoxygenation of Biomass-Derived Oxygenates to Unsaturated Hydrocarbons Using Molybdenum Carbide Catalysts, *ChemSusChem* 6 (2013) 798–801. doi:10.1002/cssc.201200991.
- [25] A.-F. Lamic, T. L. H. Pham, C. Potvin, J.-M. Manoli, G. Djéga-Mariadassou, Kinetics of Bifunctional Isomerization over Carbides (Mo, W), *Journal of Molecular Catalysis A: Chemical* 237 (2005) 109–114. doi:10.1016/j.molcata.2005.03.041.
- [26] J. Han, J. Duan, P. Chen, H. Lou, X. Zheng, H. Hong, Nanostructured Molybdenum Carbides Supported on Carbon Nanotubes as Efficient Catalysts for One-Step Hydrodeoxygenation and Isomerization of Vegetable Oils, *Green Chemistry* 13 (2011) 2561–2568. doi:10.1039/c1gc15421d.
- [27] A. P. E. York, C. Pham-Huu, P. Del Gallo, E. A. Blekkan, M. J. Ledoux,

- Comparative Effect of Organosulfur Compounds on Catalysts for the *n*-Heptane Isomerization Reaction at Medium Pressure: Mo₂C-Oxygen-Modified, MoO₃-Carbon-Modified, Pt/ γ -Al₂O₃, and Pt/ β -Zeolite Catalysts, *Industrial & Engineering Chemistry Research* 35 (1996) 672–682. doi:10.1021/ie950409a.
- [28] M. E. Dry, G. J. Oothuizen, The Correlation between Catalyst Surface Basicity and Hydrocarbon Selectivity in the Fischer-Tropsch Synthesis, *Journal of Catalysis* 11 (1968) 18–24. doi:10.1016/0021-9517(68)90004-3.
- [29] Y. Yang, H.-W. Xiang, Y.-Y. Xu, L. Bai, Y.-W. Li, Effect of Potassium Promoter on Precipitated Iron-Manganese Catalyst for Fischer-Tropsch Synthesis, *Applied Catalysis A: General* 266 (2004) 181–194. doi:10.1016/j.apcata.2004.02.018.
- [30] J. Corella, J. M. Asua, Kinetic Equations of Mechanistic Type with Nonseparable Variables for Catalyst Deactivation by Coke. Models and Data Analysis Methods, *Industrial & Engineering Chemistry Process Design and Development* 21 (1982) 55–61. doi:10.1021/i200016a011.
- [31] E. Wolf, Kinetics of Deactivation of a Reforming Catalyst during Methylcyclohexane Dehydrogenation in a Diffusion Reactor, *Journal of Catalysis* 46 (1977) 190–203. doi:10.1016/0021-9517(77)90199-3.

CHAPTER 4

Pathway of selectivity influence for transition versus alkali metals

4.1. Introduction

From the results in Chapter 3, K promotion is known to be an effective method of controlling selectivity for bio-oil model compound conversion on Mo₂C. However, the products that increased in selectivity with K promotion were not necessarily the most “desired” product. For example, 3-butenal is a more preferred compound than crotonaldehyde because coupling products from 3-butenal are more linear than coupling products from crotonaldehyde; the double bond shifts from between two internal C atoms to the being on the end of the carbon chain. However, 3-butenal is not deoxygenated or nor has increased energy density. In order to be able to tune selectivity to the most desired products, this chapter aims to identify a link between catalyst properties and performance, so that selectivity can be controlled for further optimization.

As suggested in Chapter 3, selectivity changes with K promotion may be due to K’s effect on Mo₂C active site concentrations. Mo₂C catalysts have been shown to possess multiple types of surface active sites. Various studies have described acid, base, and metallic sites on Mo₂C [1–18]. Surface sites can be quantified in a variety of ways including pulse chemisorption, temperature-programmed desorption (TPD), FTIR, test reactions (including *in situ* titration), and more.

In pulse chemisorption, the catalyst is exposed to small doses of a probe molecule

that is known to adsorb on a particular type of active site. The amount of probe molecule that does not adsorb is monitored by spectroscopic or chromatographic techniques. When the catalyst surface is saturated with the probe molecule, the following doses will not be fully adsorbed, and the amount of probe molecule detected per pulse equal to the previous. The metallic character of Mo₂C has been measured via CO pulse chemisorption [2–6] and H₂ pulse chemisorption [5–7].

For TPD, the catalyst is saturated with a probe molecule. It is then exposed to a flowing inert gas, with the goal of desorbing any physisorbed probe molecule, and leaving the chemisorbed probe molecules on the surface. The catalyst is then heated at a constant rate, and the amount of probe molecule that desorbs during heating is detected by spectroscopic or chromatographic techniques, and quantified. In TPD with co-adsorption, before heating, the catalyst is saturated with a second probe molecule that is known to adsorb on a different active site; the inert gas purge is repeated before the catalyst is heating [19]. TPD with co-adsorption addresses two weaknesses of TPD: (1) it more accurately accounts for induction effects on catalysts with multiple types of active sites and (2) ensures that not sites are double-counted. The total acid character of Mo₂C has been quantified via NH₃ [1,7,8]; *n*-propylamine [2,9,10,20], *iso*-propylamine [3], and ethylamine [11] TPD of Mo₂C have been used to distinguish between Lewis and Brønsted acidity. The metallic character of Mo₂C has been measured with H₂ TPD [8,12]. CO₂ TPD has been used to quantify basic sites on Mo₂C [1,8,12–14].

FTIR offers another way of quantifying active sites. A probe molecule is adsorbed onto the surface, and the position and size of the FTIR bands are quantified to determine site concentration. This method avoids challenges with TPD that can hamper interpretation

including the potential of convection lag, diffusive lag, particle concentration gradient, bed concentration gradient, readsorption at infinite flow rates, and readsorption (more in Section 4.3.1). Pyridine FTIR [15,16] has been employed to quantify acid site densities of Mo₂C, but only for Mo₂C on a support. For Mo₂C/Al₂O₃, only Lewis acidity was detected (no Brønsted acidity), but the authors believed those acid centers to be on the Al₂O₃ and not on the Mo₂C.

In situ site titration is another method available to quantify active sites. For this method, a known site poison with high specificity is introduced to the catalyst on-stream during reaction. The change in productivity is monitored as it decreases, and this is used to calculate the total adsorption of the site poison, which is representative of the active site concentration. For Mo₂C, Brønsted acid sites have been measured by *in situ* 2,6-di-tert-butylpyridine (DTBP) titration during isopropanol dehydration [17,18].

While these methods provide the ability to quantify the catalyst's site concentrations, it does not necessarily provide information on the identity of the active sites. Multiple theories have been offered to describe the base site identity on Mo₂C. One theory is that charge transfer from the Mo to the C results in negative charge on the C which is the location of the base sites on the Mo₂C surface [1]. DFT work has further suggested that C defect in α -Mo₂C results in an electron "trap" with increased electron density, which may be the source of Lewis base sites [21]. In other work, a Mo–O species has been theorized as the base site [17]. In terms of their function, base sites on Mo₂C have been shown to catalyze dehydrogenation [1].

Bej et. al. proposed that charge transfer from the Mo to the C results in electron deficiency, and a corresponding positive charge, on the Mo that is the location of the acid

site [1]. Weak acid sites on Mo₂C have also been attributed to O, both by O₂ exposure and incomplete removal of hydroxyl groups during pretreatment [7,17]. Mechanistically, acid sites on Mo₂C have been found to be active for dehydrogenation, cracking, isomerization, dealkylation, and dehydration reactions [1,2].

Metallic sites, often identified as H-adsorption or H* sites, have been attributed variously to exposed Mo and/or C atoms [3,4,7]. These metallic sites on Mo₂C have been credited for hydrogenation and hydrogenolysis activity [2].

When studied on Al₂O₃ support, K promotion with KNO₃ and KI was found to increase the basicity of the catalyst up to 35 wt% [22,23]. K addition to VO_x/Al₂O₃ catalyst was determined to decrease acidity and increase basicity; acid sites were removed and replaced by base sites which formed from coordination with surface vanadia species [24].

Alkali promoters have proven to be an effective way to manipulate the balance of active sites on the surface of heterogeneous catalysts. Group IA metals were found to increase the density of medium- and high-strength base sites for MgO [25].

For MoC_{1-x}, Vo et al. reported that total acid sites decreased with K and Na promotion, while total base sites increased [8]. Ardakani and Smith found that while 1% K doping of Mo₂C/HY catalyst did not affect the total acidity, it increased the Lewis acidity and decreased the Brønsted acidity [9].

Alkali promoters can affect the active sites on the catalyst surface via electronic and/or geometric factors. Electronically, the alkali promoter can influence the electron density of the metal. Studies of K on Ru(001) with Photoemission of Adsorbed Xenon atoms (PAX) found that K exhibits relatively short-range electronic effects, up to ca. 6 Å [26]. On Mo₂C, potassium has been found to increase the electron density of the Mo surface

atoms [27]. More specifically, Xiang et. al. found that K acted as an electronic promoter on β -Mo₂C and affected the relative amounts of Mo in various oxidation states, while K interaction with α -Mo₂C was much weaker and did not significantly affect distribution of oxidation states [28].

Geometrically, it may physically block active sites on the surface. For a Ru silica catalyst, the geometric effect was determined to be the predominant mechanism by which an alkali promoter affected the selectivity of Fischer-Tropsch reaction [29].

4.2. Experimental Methods

4.2.1 Catalyst Synthesis

Catalysts were synthesized by the same manner described in Section 3.2.1.

4.2.2 Catalyst Characterization

The acid and base site concentrations were measured by temperature programmed desorption (TPD) using a Micromeritics AutoChem 2920 Automated Catalyst Characterization System equipped with a Pfeiffer Vacuum Quadstar GSD-301 mass spectrometer (MS). NH₃ and CO₂ were used as probe molecules to characterize the acid and base sites, respectively. Approximately 100 mg of catalyst was loaded into the U-tube quartz reactor. The Mo₂C and K/Mo₂C catalysts were pretreated in 15% CH₄/H₂ at 590 °C for 4 h, and the MgO was pretreated in 1% O₂/He at 500 °C for 2 h. The catalysts were then treated in UHP He at the respective pretreatment temperatures for 30 min to remove any physisorbed species before being cooled to 40 °C. The sample was then saturated with

the probe molecule by flowing 50 mL min⁻¹ of either CO₂ or NH₃ for 2 h. The gas was then switched to UHP He for 1 h to remove the physisorbed species. The samples were heated to 800 °C at 10 °C min⁻¹ and the desorbed molecules were measured using the MS. The signals for CO₂ (m/z=44) or NH₃ (m/z=16) were calibrated after every experiment to account for changes in the baseline vacuum pressure. Peak areas were integrated and converted to adsorbed moles with response factors obtained via the calibration. A sample loop of known volume (500 µL) was used to calibrate the MS responses and quantify the amount desorbed from the catalyst surface. An adsorption stoichiometry of one NH₃ and CO₂ molecule per acid and base site, respectively, was assumed.

The CO₂-TPD and NH₃-TPD spectra for the Mo₂C catalysts were deconvoluted into peaks that were 30% Lorentzian and 70% Gaussian with a linear baseline using the peak fitting software CasaXPS. The number of peaks used in the fits was chosen to achieve a good fit (residual RMS <3% of the maximum, as detailed in Table S1) between the TPD curve (y_i) and the fitted curve (\hat{y}_i) while minimizing the number of peaks required. The residual RMS were determined using the following:

$$\text{residual RMS} = \sqrt{\frac{\sum_{i=1}^n (\hat{y}_i - y_i)^2}{n}} \quad (1)$$

The full-width-half-maxima (FWHM) of each peak were constrained so that the FWHM of each peak was constant for all TPD spectra of the same probe molecule. After fitting, the coefficients of determination (R^2) and correlation coefficients (r) were determined for each set of peak areas. The peak maximum was identified as the temperature at which the envelope of the deconvoluted peaks reached a maximum.

The H* site concentrations were measured by H₂-TPD using an Altamira AMI-390

equipped with a thermal conductivity detector (TCD). Catalyst samples (ca. 10-40 mg) were loaded into a 1/4 in. quartz U-tube reactor and analyzed using the TPD system. The Mo₂C and K/Mo₂C catalysts were pretreated in 15% CH₄/H₂ at 590 °C for 4 h. The carbides were then cooled to 40 °C in 15% CH₄/H₂ and saturated with 5% H₂/Ar at 30 mL min⁻¹ for 1 h. The MgO was pretreated in 10% O₂/He at 500 °C for 2 h then cooled in 10% O₂/He to 40 °C, purged with UHP Ar at 25 mL min⁻¹ for 1 h before being saturated with 5% H₂/Ar at 30 mL min⁻¹ for 1 h. Excess and/or physisorbed H₂ was removed by holding the sample at 40 °C for 5 min in flowing UHP Ar at 25 mL min⁻¹. The samples were heated to 500 °C at 15 °C min⁻¹ in flowing UHP Ar (25 mL min⁻¹), followed by a 30 min hold at 500 °C. A sample loop of known volume (100 μL) was used to calibrate the TCD response for 5% H₂/Ar and quantify the amount of H₂ desorbed from the catalyst surface. An adsorption stoichiometry of two H* sites per H₂ molecule desorbed was assumed. The peak maximum was identified as the temperature at which the signal reached a maximum.

4.3. Results

4.3.1 Evaluating TPD Dimensionless Numbers

Demmin and Gorte derived six dimensionless numbers which can be used to identify potential effects of convection lag, diffusive lag, particle concentration gradient, bed concentration gradient, readsorption at infinite flow rates, and readsorption at low flow rates for temperature-programmed desorption [30], as shown in Table 4.2. Most parameters necessary for the calculations of the dimensionless numbers are experimentally determined, observed, or measured, as shown in Table 4.1. The particle diffusion coefficients, D_p , of NH₃ and CO₂ in He were calculated the same way as the effective

diffusivity for the Weisz-Prater criterion, described in Section 2.3.2. The bed dispersion coefficient, D_B , is a function of the superficial velocity, u_0 , the catalyst particle radius, R , the bed porosity, ε_B , and the Peclet number, Pe :

$$D_B = \frac{2u_0R}{\varepsilon_B Pe}$$

And Pe is calculated from an empirical correlation [31]:

$$Pe = \frac{0.3}{Re \cdot Sc} + \frac{0.5}{1 + 3.8(Re \cdot Sc)^{-1}}$$

Table 4.1. Parameters used to analyze dimensionless parameters associated with temperature-programmed desorption, and their associated values for the experiments described in this work.

ε_B	bed porosity	0.69
ε_P	particle porosity	0.33
β	heating rat	10 K sec ⁻¹
Q	carrier flow rate	50 mL min ⁻¹
T_f	final temperature	800 °C
T_0	starting temperature	40 °C
N	number of particles in bed	2800
R	particle radius	62.5 μm
L	bed length	2 mm
V	bed volume	230 mm ³
α	particle surface area	< 110 m ² g ⁻¹
ρ	particle density	2085 kg m ⁻³
s	sticking coefficient	< 1

Table 4.2. Dimensionless numbers associated with temperature-programmed desorption, based on [1].

Parameter	Definition	Observed effect	Value	Ideal requirement
$\frac{\varepsilon_B V \beta}{Q(T_f - T_0)}$	Residence time of carrier gas	Convective lag	.002	< 0.01
$\frac{\varepsilon_P R^2 \beta}{D_P(T_f - T_0)}$	Time constant for diffusion out of an individual particle	Diffusive lag	2E-8	< 0.01
$\frac{QR}{4\pi R^2 N D_P}$	[carrier-gas flow rate]: [diffusion rate]	Particle concentration gradients	0.001	<0.05
$\frac{QL^2}{V D_B}$	[carrier-gas flow rate]: [axial mixing]	Bed concentration gradients	0.05	<0.1
$\frac{\alpha \rho s F R^2}{\pi D_P}$	[adsorption rate]: [diffusion rate]	Readsorption at infinite flow rate	Max: 2×10^8	<1
$\frac{\alpha \rho s F V (1 - \varepsilon_B)}{Q}$	[adsorption rate]: [carrier-gas flow rate]	Readsorption at low flow rate	Max: 1×10^4	<1

The dimensionless numbers for convective lag, diffusive lag, particle concentration gradients, and bed concentration gradients were calculated to be less than the ideal requirements of 0.01, 0.01, 0.05, and 0.1, respectively, confirming that the observed effects are not expected. However, the dimensionless numbers associated with readsorption at infinite and low flow rates were both calculated to be significantly larger than the ideal requirement of 1. While the dimensionless numbers associated with readsorption are both greater than the requirement, they do not change significantly with different catalysts. In particular, only α will change, and will nominally decrease with increasing amounts of potassium deposited on the catalyst. Thus, at increasing potassium loadings, readsorption is expected to become less significant, though the change is expected to be negligible.

4.3.2 Active Site Concentration Measurements

CO₂-TPD and NH₃-TPD profiles are shown in Figure 4.1. CO and CO₂ also desorbed at temperatures above 700 °C, consistent with previous reports which suggested that these products were due to decomposition of the Mo₂C [1]. The amounts of CO₂, NaH₃, and H₂, desorbed at temperatures below 540, 450, and 450 °C, respectively, were quantified for each material. The amounts were converted to site concentrations and are listed in Table 4.5 and illustrated in Figure 4.3.

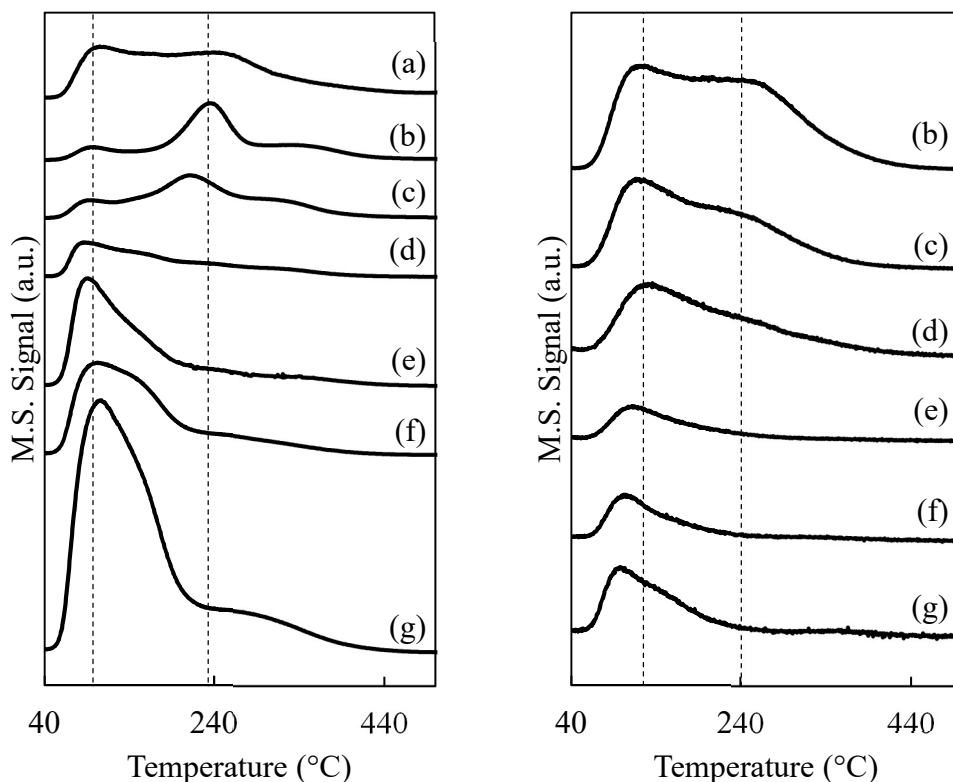


Figure 4.1. CO₂-TPD (left) and NH₃-TPD (right) profiles of (a) MgO, (b) Mo₂C, (c) K(0.1ML)/ Mo₂C, (d) K(0.3ML)/ Mo₂C, (e) K(0.5ML)/Mo₂C Mo₂C (f) K(0.7ML)/ Mo₂C, and (g) K(1.1ML)/ Mo₂C catalysts where M.S. signal has been normalized by the surface area of the catalysts. Peak maxima temperatures are listed for strong and weak deconvoluted peaks for each TPD. Dash lines represent peak maxima temperature of deconvoluted peaks for Mo₂C.

Deconvolution of the CO₂-TPD spectra indicated the presence of four peaks with maxima between 83-94 °C, 123-140 °C, 212-232 °C, and 298-348 °C, as shown in Figure 4.2. The deconvolution matched well to the TPD spectra, as evidenced by low residuals compared to the maximum, as shown in Table 4.3. The site concentrations derived from the deconvolution are listed in Table 4.4. The areas of the two low-temperature peaks (red and green) correlated and were therefore considered to be identified with the same site type. The sites associated with the red and green peaks are designated as weak base sites. The areas of the two high-temperature peaks (purple and blue) also correlated; similarly, the sites corresponding to the purple and blue peaks are designated as strong base sites. The resulting concentrations of weak and strong base sites are shown in Table 4.5. The peak maxima for the first peak generally shifted to lower temperatures with increasing K loading up to 0.7ML. In addition, the weak base site concentrations increased with K addition. Trends for the strong base sites were not a clear function of K, but their concentrations did appear to decrease to 0.3ML K and then increase up to 1.1ML K. The weak base sites accounted for ca. 14% of the total base sites on Mo₂C and ca. 79% for the K(1.1ML)/Mo₂C material.

Table 4.3. Residual RMS of recorded TPD vs the deconvolution pattern. RMSE% is a scale-independent error from residual RMS divided by the maximum value.

	CO ₂			NH ₃		
	Residual RMS ($\frac{\text{molecules}}{\text{cm}^2 \cdot \text{K}}$)	Max ($\frac{\text{molecules}}{\text{cm}^2 \cdot \text{K}}$)	Residual RMS Max	Residual RMS ($\frac{\text{molecules}}{\text{cm}^2 \cdot \text{K}}$)	Max ($\frac{\text{molecules}}{\text{cm}^2 \cdot \text{K}}$)	Residual RMS Max
Mo ₂ C	5.60E+10	1.66E+09	3.0%	5.25E+10	8.09E+08	1.5%
K(0.1ML)/ Mo ₂ C	4.36E+10	5.59E+08	1.3%	4.88E+10	7.59E+08	1.6%
K(0.3ML)/ Mo ₂ C	3.61E+10	1.00E+09	2.8%	4.91E+10	6.93E+08	1.4%
K(0.5ML)/ Mo ₂ C	1.06E+11	2.59E+09	2.4%	2.17E+10	3.09E+08	1.4%
K(0.7ML)/ Mo ₂ C	9.17E+10	2.33E+09	2.5%	2.93E+10	4.55E+08	1.6%
K(1.1ML)/ Mo ₂ C	3.55E+11	8.43E+09	2.4%	4.41E+10	9.12E+08	2.1%

Table 4.4. Base and acid site concentrations for each deconvoluted peak.

Catalyst	Site Concentration (10 ¹⁴ molecules cm ⁻²)					
	Base Peak 1	Base Peak 2	Base Peak 3	Base Peak 4	Acid Peak 1	Acid Peak 2
Mo ₂ C	0.03	0.06	0.18	0.11	0.09	0.11
K(0.1ML)/Mo ₂ C	0.03	0.06	0.17	0.14	0.07	0.11
K(0.3ML)/Mo ₂ C	0.06	0.13	0.07	0.04	0.08	0.08
K(0.5ML)/Mo ₂ C	0.18	0.31	0.10	0.05	0.03	0.03
K(0.7ML)/Mo ₂ C	0.15	0.42	0.09	0.05	0.04	0.05
K(1.1ML)/Mo ₂ C	0.52	0.97	0.18	0.16	0.06	0.10

Characteristic NH₃-TPD profiles are also shown in Figure 4.1. Below 500 °C, the signal at m/z=16 was independent of that at m/z=28, suggesting that the peak was due to NH₃ and not to CO or CO₂. Based on this observation, the signal at m/z=16 was assigned to NH₃. There was no evidence for desorption of other N-containing species; m/z=14 did not reveal desorption peaks for N₂. Deconvolution of the NH₃-TPD resulted in three peaks with maxima between 100-119 °C, 146-165 °C, and 200-275 °C. The peak concentrations

corresponding to those peaks are shown in Table 4.4. The areas of the two low-temperature peaks (red and green) correlated strongly; sites associated with these peaks were designated as weak acid sites. The higher-temperature peak (purple) was assigned to strong acid sites. The corresponding site concentrations for weak and strong acid sites are displayed in Table 4.5 and are in good agreement with values reported in literature for Mo₂C [1].

As shown in Table 4.5, approximately 32% of the total acid sites on Mo₂C were weak, while weak acid sites accounted for 84% of the total acid sites for the K(1.1ML)/Mo₂C material. The strong acid site concentration decreased linearly with K addition up to K(0.5ML)/Mo₂C, at which point the strong acid sites were virtually eliminated, while the weak acid site concentration decreased with a minimum observed on the K(0.5ML)/Mo₂C catalyst (0.06×10^{14} molecules cm⁻²), and then increased with further K loading. This trend resembles that for the strong base sites, which also decreased with K addition and then increased with further K addition.

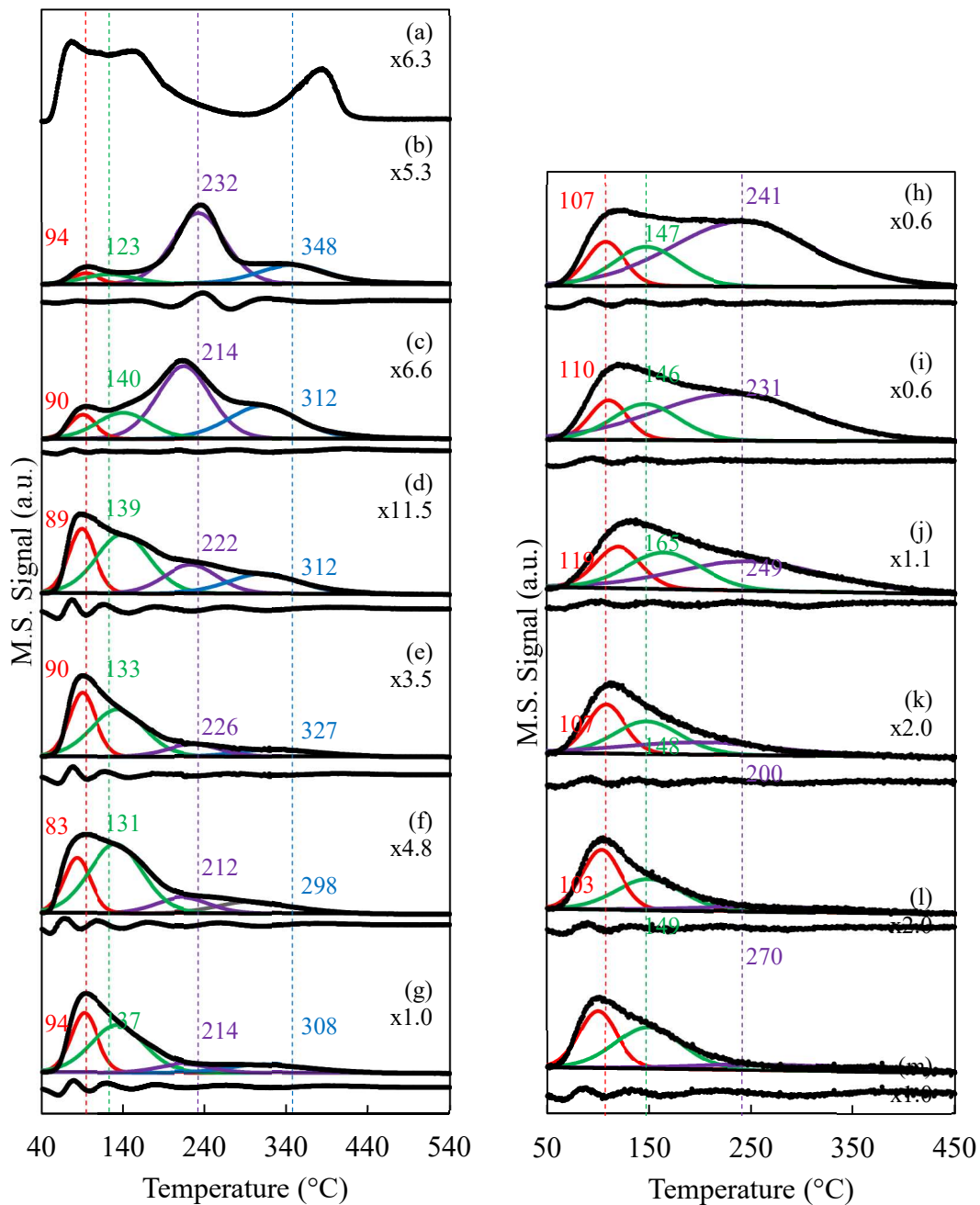


Figure 4.2. Deconvolution of CO_2 -TPD (left) and NH_3 -TPD profiles (right) of (a) MgO, (b) and (h) Mo₂C, (c) and (i) K(0.1ML)/Mo₂C, (d) and (j) K(0.4ML)/ Mo₂C, (e) and (k) K(0.5ML)/ Mo₂C, (f) and (l) K(0.7ML)/ Mo₂C, and (g) and (m) K(1.1ML)/ Mo₂C catalysts. Deconvoluted peaks (peak maxima are noted in $^\circ\text{C}$ with corresponding colors, and dashed lines represent the peak maxima of Mo₂C), background, and residual (difference between raw spectrum and fit) are shown for all the Mo₂C catalysts. The M.S. signal has been scaled so that the profiles are of the same height for ease of viewing (scaling factors are listed below figure labels).

Table 4.5. Base, acid, and H* site concentrations for the various catalysts.

Catalyst	Site Concentration (10 ¹⁴ molecules cm ⁻²)						
	Weak Base [%]	Strong Base [%]	Total Base	Weak Acid [%]	Strong Acid [%]	Total Acid	H*
MgO			1.04				
Mo ₂ C	0.05 [13]	0.33 [87]	0.38	0.20 [32]	0.42 [68]	0.62	0.36
K(0.1ML)/Mo ₂ C	0.10 [25]	0.30 [75]	0.41	0.15 [34]	0.29 [66]	0.43	0.27
K(0.3ML)/Mo ₂ C	0.19 [63]	0.11 [37]	0.30	0.15 [50]	0.15 [50]	0.30	0.07
K(0.5ML)/Mo ₂ C	0.50 [78]	0.14 [22]	0.64	0.06 [67]	0.03 [33]	0.09	0.12
K(0.7ML)/Mo ₂ C	0.54 [75]	0.18 [25]	0.71	0.09 [82]	0.02 [18]	0.11	0.19
K(1.1ML)/Mo ₂ C	1.7 [79]	0.44 [21]	2.1	0.15 [83]	0.03 [17]	0.19	0.09

Table 4.6. Ratios of catalyst active site concentrations.

Catalyst	Ratio of Site Concentrations		
	Base:Acid	Acid:H*	Base:H*
MgO			
Mo ₂ C	0.6	1.8	1
K(0.1ML)/Mo ₂ C	0.9	1.6	2
K(0.3ML)/Mo ₂ C	1	4.9	5
K(0.5ML)/Mo ₂ C	7	0.7	5
K(0.7ML)/Mo ₂ C	7	0.6	4
K(1.1ML)/Mo ₂ C	10	2.1	20

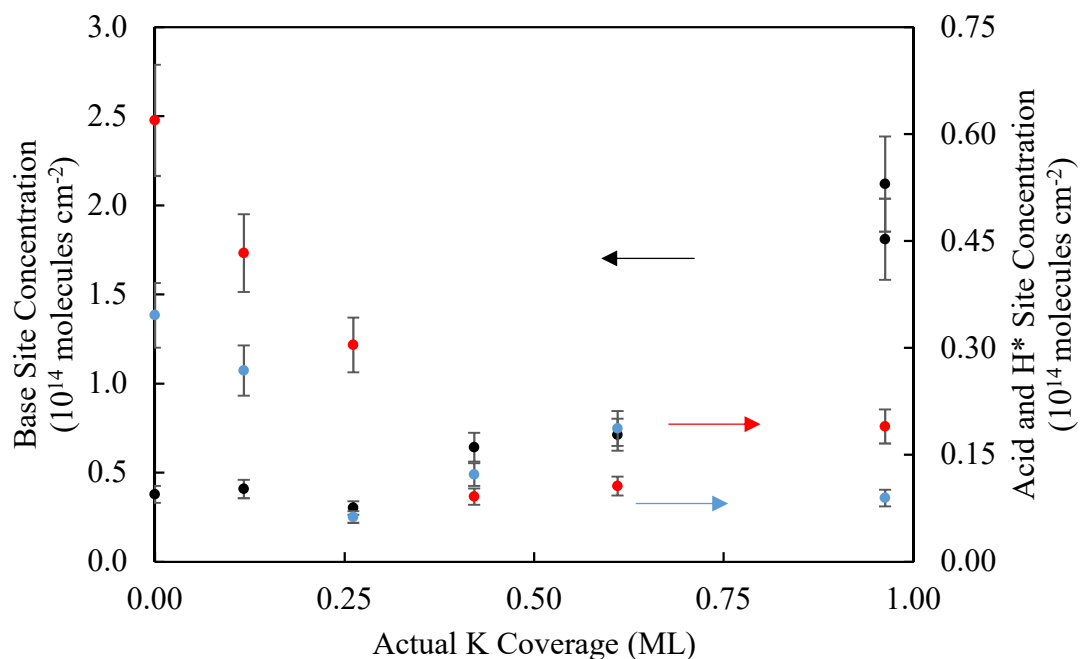


Figure 4.3. Site concentrations of base (•), acid (•), and H* sites (•) on the surface of Mo₂C catalysts with increasing K coverage. Error bars represent 95% confidence interval.

Characteristic H₂-TPD profiles are shown in Figure 4.4. The peak maxima were between 101 and 137 °C. In general, the temperature of the peak maximum decreased with K loading suggesting that the addition of K weakened the overall strength of the H* sites. The amounts of desorbed H₂ are listed in Table 4.5. While all K-modified catalysts showed a decreased concentration of H* sites compared to the Mo₂C, the trend as a function of K concentration is less clear and seems vary from low K loadings (<0.5ML) to high K loadings (>0.5ML). The overall reduction in H* site concentration is consistent with previous reports that alkali addition inhibits hydrogen adsorption [32]. Assuming a total site concentration of 10¹⁵ cm⁻², the H* sites account for 0.3-1.7% of the surface sites on the Mo₂C based catalysts.

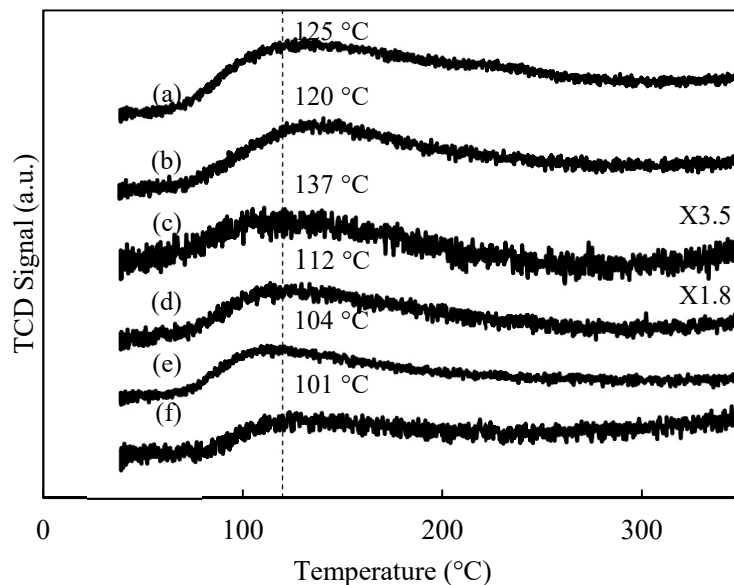


Figure 4.4. H₂-TPD profiles of (a) Mo₂C, (b) K(0.1ML)/Mo₂C, (c) K(0.3ML)/Mo₂C, (d) K(0.5ML)/Mo₂C, (e) K(0.7ML)/Mo₂C, and (f) K(1.1ML)/Mo₂C catalysts where TCD signal has been normalized by the surface area of the catalysts. Dashed line marks the temperature of the peak maximum for Mo₂C. Some spectra have been scaled for ease of viewing; scaling factor is noted on the figure.

4.3.3 Linking Active Sites Concentrations to Selectivity

The addition of K had a significant impact on the acetic acid and crotonaldehyde upgrading selectivities. Relationships between the selectivities and site concentrations were assessed by correlating concentrations of the acid, base, and H* sites with the productivities. An example for 3-butenal productivity from crotonaldehyde upgrading is shown in Figure 4.5. The Pearson product-moment correlation coefficient (r) and the coefficient of determination ($R^2 = r^2$) were calculated for all pairings of site types and products from both acetic acid and crotonaldehyde upgrading, and the R^2 values are shown in Table 4.7. A positive relationship ($r > 0$) conveys that the productivity increases as the site concentration increases; for this analysis, the product-site pairings with $r < 0$ were

discounted because it conveys that new sites of the given type do not lead to an increase in productivity.

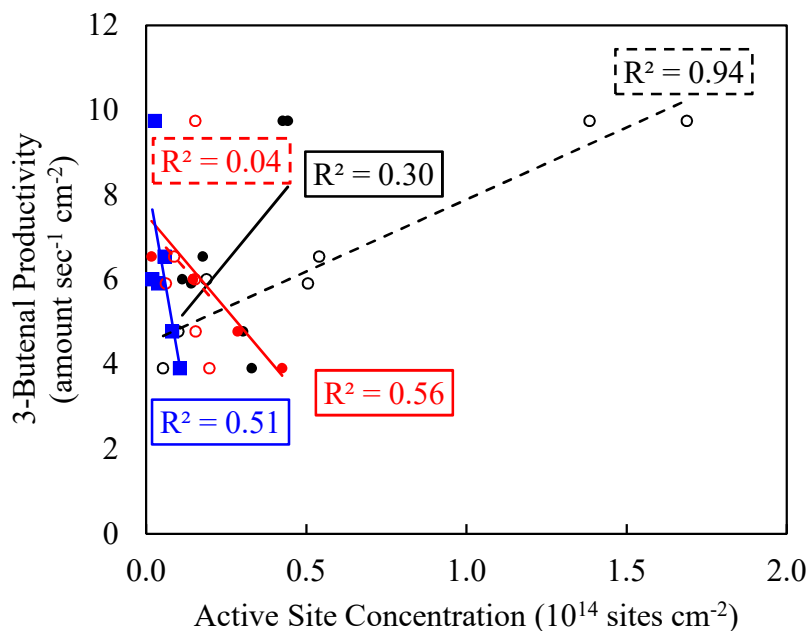


Figure 4.5. Correlations between site concentration of weak base (○), strong base (●), weak acid (○), strong acid (●), and H* sites (■) with the 3-butenal productivity.

The R^2 values quantify the linearity of the relationship between the productivity and site concentration. A strong correlation (high R^2) between a specific site type and productivity suggests that the productivity is linearly related to the site concentration, and therefore a given change in site concentration produces a standard change in the productivity. Essentially, a high R^2 represented a more constant turnover frequency of the given product on the given site type. A weak correlation (low R^2) suggested that the product and site type were not mechanistically related. Colloquially, the R^2 represents the percentage of the change in productivity that can be attributed to the site concentration. Here, $R^2 > 0.70$ are taken to be significant, in the sense that the given site type is worthy

of further investigation as playing a significant role in that product's productivity.

For acetic acid upgrading, seven pairings of products and site types were found to have $R^2 > 0.70$. Strong acid sites and total acid sites both correlated with acetaldehyde and CO. Total base sites correlated with acetone and CO₂, and weak base sites correlated well with acetone. CO₂ and acetone and both ketonization products, so their productivities are not independent.

For crotonaldehyde upgrading, four pairing of products and site types were found to have $R^2 > 0.70$. Total base sites correlated well with 3-butenal and butyraldehyde productivity, weak base sites correlated strongly with 3-butenal productivity, and strong base sites correlated well with butene productivity.

Table 4.7. Correlations between productivity of each product and acid, H*, and base site concentrations for Mo₂C and K/Mo₂C catalysts.

AA Correlations							
Product	Weak Acid Sites	Strong Acid Sites	Total Acid Sites	H* Sites	Total Base Sites	Weak Base Sites	Strong Base Sites
Acetaldehyde	0.38	0.76	0.71	0.69	0.07	0.15	0.15
Acetone	0.06	0.22	0.20	0.00	0.79	0.73	0.44
CO ₂	0.06	0.18	0.16	0.00	0.72	0.64	0.48
CO	0.40	0.75	0.72	0.67	0.08	0.16	0.13
CR Correlations							
Product	Weak Acid Sites	Strong Acid Sites	Total Acid Sites	H* Sites	Total Base Sites	Weak Base Sites	Strong Base Sites
Butadiene	0.11	0.12	0.12	0.12	0.01	0.00	0.23
Butenes	0.47	0.34	0.39	0.34	0.17	0.08	0.80
3-Butenal	0.56	0.04	0.41	0.51	0.89	0.94	0.30
Butyraldehyde	0.03	0.06	0.02	0.04	0.74	0.66	0.67

4.4. Discussion

Potassium addition increased the base site concentration while also causing an

overall weakening in the base site strength. In the CO₂-TPD spectra, the peak maxima for the first peak generally shifted to lower temperatures with increasing K loading up to 0.7ML. This change cannot be explained by mass transfer limitations or readsorption in the catalyst bed as investigated in the previous section, and indicates an overall weakening of these base sites, or a destabilization of the CO₂ absorbed on the base sites due to repulsive forces associated with the increased CO₂ surface coverage.

The base site concentration decreased marginally upon addition of small amounts of K (<.3ML) but then increased with larger amount of K. However, the relative amounts of weak and strong base sites changed even with small amounts of K. One possibility is that at loadings below 0.5ML, the K is well-dispersed on the surface and weakens both the weak and strong acid sites, essentially converting a portion of the strong sites to weak sites and eliminating some weak sites. With K loadings above 0.5ML, the K species may have agglomerated on the surface, and the agglomerations are either less efficient at weakening and eliminating base sites, or the agglomerations could themselves be the source of additional (predominantly weak) base sites. Frusteri et. al. similarly found that K increased the deactivation constant for K promotion of Ni/MgO catalyst [33].

The total base site concentrations correlated strongly and positively with the production of acetone (and its co-product, CO₂) and 3-butenal for acetic acid and crotonaldehyde upgrading, respectively. The acetone and 3-butenal formation rates correlated strongly with the weak base site concentrations, but correlated only modestly or weakly with the strong base site concentrations. Therefore, the weak base sites appeared to catalyze the formation of acetone and 3-butenal from acetic acid and crotonaldehyde, respectively. Note that these correlations were much stronger than the correlations between

acetone and 3-butenal for acetic acid and crotonaldehyde upgrading, respectively, and acid or H* site concentrations. Consequently, the increase in formation of these dominant products (*i.e.*, acetone/CO₂, 3-butenal) was more likely associated with the formation of base sites rather than the poisoning of acid sites or H* sites. Base sites have previously been observed to promote double-bond isomerization, and Hattori found that butene isomerization is initiated through abstraction of the allylic H by the base site [34].

Potassium addition also had a significant effect on catalyst acidity; specifically, the percentage of total acid sites that were weak sites increased with increasing K loading. Potassium has been previously reported to dilute or poison acid sites on catalysts, including for Mo₂C/HY [35], HZSM-5 [36], and Mo-V-Sb [37]. In the case of Mo-V-Sb, the decrease in acid sites resulted in a shift in selectivity during propane oxidation.

The strong acid and total acid concentrations correlated moderately and positively ($r > 0$) with the acetaldehyde and CO formation rates for acetic acid upgrading, suggesting that total acid sites – specifically strong acid sites – played a role in the HDO and DCO reactions. This finding is in agreement with the acid:H* site ratio being a key parameter for controlling product selectivity during biomass pyrolysis vapor upgrading [7,38,39], and further suggests that the ratio of strong acid sites to H* sites may be more descriptive. The acid and H* site concentrations only weakly correlated with each other, suggesting that these sites are largely independent. For crotonaldehyde upgrading, the weak acid and total acid site concentrations correlated well with the butene and 3-butenal formation rates.

In general, increased K loadings increased the base site concentrations and decreased the acid and H* site concentrations. The ratio of the total base sites to the acid sites increased from 0.9 for Mo₂C to 10 for the K(1.1ML)/Mo₂C material, and the ratio of

total base sites to the H* sites increased from 2 for Mo₂C to 40 for the K(1.1ML)/Mo₂C material (Table 4.6). The acid and H* site concentrations decreased with K addition – at similar rates – and therefore the total acid:H* ratios were relatively constant with K addition; however, the ratio of strong acid sites to H* sites varied considerably. It should be noted that the total acid:H* site ratio for Mo₂C reported in Table 4.6 is lower than previous reports [7], which is attributed to a difference in pretreatment conditions (H₂ at 400°C vs. CH₄/H₂ at 590°C). Previous reports regarding the HDO of acetic acid indicate that higher acid:H* ratios give rise to higher decarbonylation selectivities [38]. It is possible that H₂ and NH₃ titrated some of the same sites and/or that the acid and H* sites are associated with each other on the surface of Mo₂C catalysts. However, as will be discussed later, it is unlikely that a significant portion of H₂- and NH₃-titrated sites are directly associated with each other.

The correlation results also aid in explaining the low activity observed over the K(0.3ML)/Mo₂C material in acetic acid upgrading experiments. The low activity of the K(0.3ML)/Mo₂C sample in acetic acid upgrading experiments can be explained by (1) the decrease in strong acid site concentration and H* site concentration (Table 4.5) resulting in less activity for HDO and DCO reaction pathways, and (2) an insufficient concentration of weak base sites found on materials with greater K loading. Thus, the K(0.3ML)/Mo₂C did not have a high enough concentration of active sites (acid/H* or base sites) to convert acetic acid to products, resulting in the low observed activity. It is important to note that these data do not speak to the intrinsic activity of each site type, as the upgrading experiments were not run under differential conversion conditions. Further research is needed to determine whether the intrinsic activity of each active site type changes with K

loading, or whether the productivities and reactant consumption rates are strictly dependent on the number of available active sites.

The rate of crotonaldehyde upgrading to butadiene did not correlate strongly with any site type. This could be because (1) another uncharacterized site type is responsible for the formation of butadiene, (2) it is an intermediate and its relationship to a characterized site type is confounded, or (3) its formation depends on some combination of active sites. A similar mechanism could explain the formation of butenes, which correlated modestly with acid and H* site concentrations, but only weakly with total base and weak base site concentrations.

Previous literature reports using X-ray photoelectron spectroscopy (XPS) to study electronic effects of K promotion on carbide surfaces suggest K acts as an electron donor and transfers a portion of its electron density to the Mo and C atoms of the carbide surface. Specifically, these studies have shown that addition of K increased the number of reduced surface Mo atoms (Mo^0 or $\text{Mo}^{\delta+}$, $0 < \delta < 2$) [40]. DFT results have sought to quantify this charge transfer, and found that for $\beta\text{-Mo}_2\text{C}(001)$ (surface Mo with subsurface C layers) promoted with 1/8 surface coverage of K, the surface Mo atoms had an increase in electron density of 0.02 electrons [27]. These results help explain how the presence of K on Mo_2C surface affects active site concentrations on the support; K clusters may be active site locations, but K also electronically affects Mo_2C , and by extension, the site types on the Mo_2C .

In addition to implicating base sites in the conversion of crotonaldehyde to 3-butenal over the potassium modified Mo_2C , results presented in this chapter provide insights regarding the overall reaction pathways. Based on results for the conversion of

crotonaldehyde, butyraldehyde and crotyl alcohol, a proposed reaction pathway is illustrated in Figure 4.6. Recall that, under conditions similar to those used for the crotonaldehyde experiments, crotyl alcohol produced 3-butenal, butyraldehyde, butadiene and butenes while butyraldehyde produced butenes and butadiene. Crotyl alcohol formation was not detected during crotonaldehyde hydrogenation, perhaps due to its reactivity.

At least two site types for the K/Mo₂C catalysts are proposed, one for C=O and C=C hydrogenations and hydrodeoxygenation (HDO), and another for isomerization. Mo₂C is known to be active for both types of reactions [41–45]. The addition of small amounts of potassium to Mo₂C appears to affect primarily the hydrogenation and HDO reactions. The consequence is an increase in butyraldehyde production and a shift in HDO products from butenes to butadiene. Further increases in the potassium loading resulted in a significant suppression of the HDO activity and butyraldehyde production, and an enhancement in the isomerization activity (recall correlation between potassium and 3-butenal formation). The results are consistent with deactivation of the HDO and hydrogenation sites, and an increase in the concentration of basic, isomerization sites.

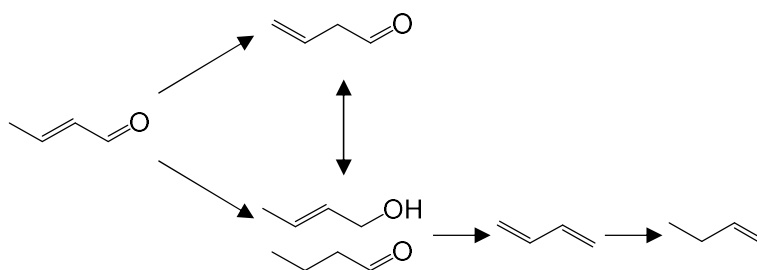


Figure 4.6. Proposed reaction pathway for crotonaldehyde upgrading.

4.5. Summary

Through TPD of NH_3 and CO_2 probe molecules, K was shown to increase basic site concentration and decrease acid and H^* site density on Mo_2C catalysts. Specifically, the K created weak base sites and eliminated strong acid sites. Through correlating the active site concentrations with productivity of each product, it was shown that the increase in base sites was responsible for the increase in productivity of the dominant products (acetone for acetic acid upgrading, 3-butenal for crotonaldehyde upgrading) at high K loadings.

4.6. References

- [1] S. K. Bej, C. A. Bennett, L. T. Thompson, Acid and Base Characteristics of Molybdenum Carbide Catalysts, *Applied Catalysis A: General* 250 (2003) 197–208. doi:10.1016/S0926-860X(02)00664-6.
- [2] S. J. Ardakani, X. Liu, K. J. Smith, Hydrogenation and Ring Opening of Naphthalene on Bulk and Supported Mo_2C Catalysts, *Applied Catalysis A: General* 324 (2007) 9–19. doi:10.1016/j.apcata.2007.02.048.
- [3] A.-F. Lamic, C.-H. Shin, G. Djéga-Mariadassou, C. Potvin, Characterization of Mo_2C –

- WO₂ Composite Catalysts for Bifunctional Isomerization: A New Pulse Method to Quantify Acid Sites, *Applied Catalysis A: General* 302 (2006) 5–13. doi:10.1016/j.apcata.2005.12.006.
- [4] J.-S. Choi, G. Bugli, G. Djéga-Mariadassou, Influence of the Degree of Carburization on the Density of Sites and Hydrogenating Activity of Molybdenum Carbides, *Journal of Catalysis* 193 (2000) 238–247. doi:10.1006/jcat.2000.2894.
- [5] J. Lee, S. T. Oyama, M. Boudart, Molybdenum Carbide Catalysts I. Synthesis of Unsupported Powders, *Journal of Catalysis* 106 (1987) 125–133. doi:10.1016/0021-9517(87)90218-1.
- [6] J. S. Lee, K. H. Lee, J. Y. Lee, Selective Chemisorption of Carbon Monoxide and Hydrogen over Supported Molybdenum Carbide Catalysts, *The Journal of Physical Chemistry* 96 (1992) 362–366. doi:10.1021/j100180a067.
- [7] J. A. Schaidle, J. Blackburn, C. A. Farberow, C. Nash, K. X. Steirer, J. Clark, D. J. Robichaud, D. A. Ruddy, Experimental and Computational Investigation of Acetic Acid Deoxygenation over Oxophilic Molybdenum Carbide: Surface Chemistry and Active Site Identity, *ACS Catalysis* 6 (2016) 1181–1197. doi:10.1021/acscatal.5b01930.
- [8] D.-V. N. Vo, T.-H. Nguyen, E. M. Kennedy, B. Z. Dlugogorski, A. A. Adesina, Fischer–Tropsch Synthesis: Effect of Promoter Type on Alumina-Supported Mo Carbide Catalysts, *Catalysis Today* 175 (2011) 450–459. doi:10.1016/j.cattod.2011.04.045.
- [9] S. J. Ardakani, K. J. Smith, A Comparative Study of Ring Opening of Naphthalene, Tetralin and Decalin over Mo₂C/HY and Pd/HY Catalysts, *Applied Catalysis A: General* 403 (2011) 36–47. doi:10.1016/j.apcata.2011.06.013.
- [10] X. Liu, K. J. Smith, Acidity and Deactivation of Mo₂C/HY Catalysts Used for the Hydrogenation and Ring Opening of Naphthalene, *Applied Catalysis A: General* 335 (2008) 230–240. doi:10.1016/j.apcata.2007.11.028.
- [11] V. Schwartz, V. T. da Silva, S. T. Oyama, Push–Pull Mechanism of Hydrodenitrogenation over Carbide and Sulfide Catalysts, *Journal of Molecular Catalysis A: Chemical* 163 (2000) 251–268. doi:10.1016/S1381-1169(00)00390-3.
- [12] K. Xiong, G. Zhou, H. Zhang, Y. Shen, X. Zhang, Y. Zhang, J. Li, Bridging Mo₂C–C and Highly Dispersed Copper by Incorporating N-Functional Groups to Greatly Enhance the Catalytic Activity and Durability for Carbon Dioxide Hydrogenation, *Journal of Materials Chemistry A* (2018). doi:10.1039/C8TA04096F.
- [13] F. Solymosi, L. Bugyi, Effects of Potassium on the Chemisorption of CO₂ and CO on the Mo₂C/Mo(100) Surface, *Catalysis Letters* 66 (2000) 227–230.

- [14] J. Huang, T. Huang, H. Chunluan, W. Huang, R. X. Ma, The Function of Sba-15 over Ni/Mo₂C Catalysts for Carbon Dioxide Reforming of Methane, *Advanced Materials Research* 455–456 (2012) 174–179. doi:10.4028/www.scientific.net/AMR.455-456.174.
- [15] L. Óvári, F. Solymosi, Determination of Acidic Centers on Supported Mo₂C Catalysts, *Journal of Molecular Catalysis A: Chemical* 207 (2004) 35–40. doi:10.1016/S1381-1169(03)00469-2.
- [16] R. Barthos, F. Solymosi, Aromatization of n-Heptane on MoC-Containing Catalysts, *Journal of Catalysis* 235 (2005) 60–68. doi:10.1016/j.jcat.2005.07.004.
- [17] M. M. Sullivan, J. T. Held, A. Bhan, Structure and Site Evolution of Molybdenum Carbide Catalysts upon Exposure to Oxygen, *Journal of Catalysis* 326 (2015) 82–91. doi:10.1016/j.jcat.2015.03.011.
- [18] M. M. Sullivan, C.-J. Chen, A. Bhan, Catalytic Deoxygenation on Transition Metal Carbide Catalysts, *Catalysis Science & Technology* 6 (2016) 602–616. doi:10.1039/C5CY01665G.
- [19] T. Tago, Y. Okubo, S. R. Mukai, T. Tanaka, T. Masuda, Simultaneous Characterization of Acidic and Basic Properties of Solid Catalysts by a New TPD Method and Their Correlation to Reaction Rates, *Applied Catalysis A: General* 290 (2005) 54–64. doi:10.1016/j.apcata.2005.05.010.
- [20] O. Kresnawahjuesa, R. J. Gorte, D. de Oliveira, L. Y. Lau, A Simple, Inexpensive, and Reliable Method for Measuring Bronsted-Acid Site Densities in Solid Acids, *Catalysis Letters* 82 (2002) 155.
- [21] C. de Oliveira, D. R. Salahub, H. A. de Abreu, H. A. Duarte, Native Defects in α -Mo₂C: Insights from First-Principles Calculations, *The Journal of Physical Chemistry C* 118 (2014) 25517–25524. doi:10.1021/jp507947b.
- [22] W. Xie, H. Peng, L. Chen, Transesterification of Soybean Oil Catalyzed by Potassium Loaded on Alumina as a Solid-Base Catalyst, *Applied Catalysis A: General* 300 (2006) 67–74. doi:10.1016/j.apcata.2005.10.048.
- [23] W. Xie, H. Li, Alumina-Supported Potassium Iodide as a Heterogeneous Catalyst for Biodiesel Production from Soybean Oil, *Journal of Molecular Catalysis A: Chemical* 255 (2006) 1–9. doi:10.1016/j.molcata.2006.03.061.
- [24] G. Garcia Cortez, J. L. Fierro, M. Bañares, Role of Potassium on the Structure and Activity of Alumina-Supported Vanadium Oxide Catalysts for Propane Oxidative Dehydrogenation, *Catalysis Today* 78 (2003) 219–228. doi:10.1016/S0920-5861(02)00341-3.
- [25] V. K. Díez, C. R. Apesteguía, J. I. Di Cosimo, Acid–Base Properties and Active

- Site Requirements for Elimination Reactions on Alkali-Promoted MgO Catalysts, *Catalysis Today* 63 (2000) 53–62. doi:10.1016/S0920-5861(00)00445-4.
- [26] K. MARKERT, K. WANDELT, THE SHORT RANGE OF THE ELECTRONIC PROMOTER EFFECT OF POTASSIUM, *Surface Science* 159 (1985) 24–34.
- [27] C. Pistonesi, A. Juan, A. P. Farkas, F. Solymosi, Effects of Potassium on the Adsorption of Methanol on β -Mo₂C(001) Surface, *Surface Science* 604 (2010) 914–919. doi:10.1016/j.susc.2010.02.020.
- [28] M. Xiang, D. Li, J. Zou, W. Li, Y. Sun, X. She, XPS Study of Potassium-Promoted Molybdenum Carbides for Mixed Alcohols Synthesis via CO Hydrogenation, *Journal of Natural Gas Chemistry* 19 (2010) 151–155. doi:10.1016/S1003-9953(09)60051-7.
- [29] M. McClory, R. GONZALEZ, The Role of Alkali Metals as Promoters in the α -ethanation and Fischer-Tropsch Reaction: An in Situ Study, *Journal of Catalysis* 89 (1984) 392–403.
- [30] R. A. Demmin, R. J. Gorte, Design Parameters for Temperature-Programmed Desorption from a Packed Bed, *Journal of Catalysis* 90 (1984) 32–39.
- [31] J. B. Butt, *Reaction Kinetics and Reactor Design*, 2nd ed., 2000.
- [32] G. P. Van Der Laan, A. A. C. M. Beenackers, Kinetics and Selectivity of the Fischer–Tropsch Synthesis: A Literature Review, *Catalysis Reviews* 41 (1999) 255–318. doi:10.1081/CR-100101170.
- [33] F. Frusteri, F. Arena, G. Calogero, T. Torre, A. Parmaliana, Potassium-Enhanced Stability of Ni/MgO Catalysts in the Dry-Reforming of Methane, *Catalysis Communications* 2 (2001) 49–56. doi:10.1016/S1566-7367(01)00008-5.
- [34] H. Hattori, Solid Base Catalysts: Generation of Basic Sites and Application to Organic Synthesis, *Applied Catalysis A: General* 222 (2001) 247–259. doi:10.1016/S0926-860X(01)00839-0.
- [35] X. Liu, S. J. Ardakani, K. J. Smith, The Effect of Mg and K Addition to a Mo₂C/HY Catalyst for the Hydrogenation and Ring Opening of Naphthalene, *Catalysis Communications* 12 (2011) 454–458. doi:10.1016/j.catcom.2010.10.025.
- [36] S. P. R. Katikaneni, J. D. Adjaye, R. O. Idem, N. N. Bakhshi, Catalytic Conversion of Canola Oil over Potassium-Impregnated HZSM-5 Catalysts: C₂–C₄ Olefin Production and Model Reaction Studies, *Industrial & Engineering Chemistry Research* 35 (1996) 3332–3346. doi:10.1021/ie950740u.
- [37] P. Botella, P. Concepcion, J. M. Lopez Nieto, B. Solsona, Effect of Potassium Doping on the Catalytic Behavior of Mo–V–Sb Mixed Oxide Catalysts in the Oxidation of Propane to Acrylic Acid, *Catalysis Letters* 89 (2003) 249–253bo.

- [38] F. G. Baddour, C. P. Nash, J. A. Schaidle, D. A. Ruddy, Synthesis of α -MoC_{1-x} Nanoparticles Using a Surface-Modified SBA-15 Hard Template and Determination of Structure-Function Relationships in Acetic Acid Deoxygenation, *Angewandte Chemie International Edition* 55 (2016) 9026–9029.
- [39] F. G. Baddour, V. A. Witte, C. P. Nash, M. B. Griffin, D. A. Ruddy, J. A. Schaidle, Late-Transition-Metal-Modified β -Mo₂C Catalysts for Enhanced Hydrogenation during Guaiacol Deoxygenation, *ACS Sustainable Chemistry & Engineering* 5 (2017) 11433–11439. doi:10.1021/acssuschemeng.7b02544.
- [40] M. Xiang, D. Li, H. Qi, W. Li, B. Zhong, Y. Sun, Mixed Alcohols Synthesis from Carbon Monoxide Hydrogenation over Potassium Promoted β -Mo₂C Catalysts, *Fuel* 86 (2007) 1298–1303. doi:10.1016/j.fuel.2006.08.032.
- [41] J. A. Schaidle, L. T. Thompson, Fischer–Tropsch Synthesis over Early Transition Metal Carbides and Nitrides: CO Activation and Chain Growth, *Journal of Catalysis* 329 (2015) 325–334. doi:10.1016/j.jcat.2015.05.020.
- [42] J. Han, J. Duan, P. Chen, H. Lou, X. Zheng, H. Hong, Nanostructured Molybdenum Carbides Supported on Carbon Nanotubes as Efficient Catalysts for One-Step Hydrodeoxygenation and Isomerization of Vegetable Oils, *Green Chemistry* 13 (2011) 2561–2568. doi:10.1039/c1gc15421d.
- [43] N. Perret, X. Wang, L. Delannoy, C. Potvin, C. Louis, M. A. Keane, Enhanced Selective Nitroarene Hydrogenation over Au Supported on β -Mo₂C and β -Mo₂C/Al₂O₃, *Journal of Catalysis* 286 (2012) 172–183. doi:10.1016/j.jcat.2011.10.026.
- [44] M. Pang, C. Liu, W. Xia, M. Muhler, C. Liang, Activated Carbon Supported Molybdenum Carbides as Cheap and Highly Efficient Catalyst in the Selective Hydrogenation of Naphthalene to Tetralin, *Green Chemistry* 14 (2012) 1272. doi:10.1039/c2gc35177c.
- [45] B. Dhandapani, T. St. Clair, S. T. Oyama, Simultaneous Hydrodesulfurization, Hydrodeoxygenation, and Hydrogenation with Molybdenum Carbide, *Applied Catalysis A: General* 168 (1998) 219–228. doi:10.1016/S0926-860X(97)00342-6.

CHAPTER 5

Pathway of selectivity influence for transition versus alkali metals

5.1. Introduction

Results from Chapter 2 showed that, of the promoter metals tested, Fe gave the highest selectivity for deoxygenation products. Consequently, the focus of this chapter was to elucidate the mechanism by which iron promotes deoxygenation. Iron has long been used a promoter metal for organic catalytic reactions, and has been found to exert effects of various type and magnitude depending on the reaction phase and the model compound size [1]. For example, Fe promotion of a Pt catalyst for the gas-phase hydrogenation of acrolein (MW = 56.06) , a small molecule, caused only a small shift in selectivity (from ca. 2% to ca 8%) [2]. The shift was more significant for crotonaldehyde (MW = 70.09), and even more significant for 3-methyl-crotonaldehyde (MW = 84.12). This particular effect was attributed to the increasing steric hindrance, with methyl group addition, of adsorption through the carbonyl group. Similar trends were observed for other promoters including Ti, V, Ga, Ge, and Sn, but the differences between model compounds was most pronounced for Fe. For cinnamaldehyde, a much larger molecule (MW = 132.16), Fe promotion of a Pt catalysts for liquid-phase hydrogenation caused a large shift in selectivity (from ca. 70% to ca. 90%) [3]. Iron has also been incorporated into bimetallic catalysts. Adding Fe to a Ni/SiO₂ catalyst decreased the overall rate, but increased 2-methylfuran selectivity of furfural conversion at similar levels of conversion [4].

Iron-based catalysts have been used as effective HDO catalysts for bio-oil model compounds. Fe/SiO₂ was used as a selective HDO catalyst for guaiacol HDO, and rate was found to be proportional to the available iron surface for different Fe loadings [5]. At 25 min TOS, the Fe/SiO₂ catalyst gave selectivity to benzene and toluene over 75% but became much less selective with more TOS. For these catalysts, coke deposition was observed at the interface of the Fe and the support, suggesting that the interface was the location of the active sites for HDO. Fe/C was used as selective catalysts for guaiacol HDO [6]. Fe/C was found to have lower activity than precious metal catalysts, but high selectivity to unsaturated and non-ring-opened products such as benzene, toluene, and phenol.

Previous work has shown that Fe promotion may affect the overall acidity of a catalyst. Sikabwe and White reported that decreased the Lewis acidity of surface carbenium ions on sulfated zirconia as a result of Fe promotion accounted for the difference in reactivities between the unpromoted and promoted sulfated zirconia catalysts [7]. In contrast, Chen et. al concluded that Fe promotion of a sulfated zirconia *increased* the density and strength of surface acid sites, as determined by ³¹P MAS NMR and adsorbed trimethylphosphine oxide [8]. For nitrogen-doped carbon-supported iron catalysts, Li et. al. determined via NH₃ TPD that iron loading introduced Lewis acid sites, and by CO₂ TPD that no base sites were present on the catalyst surface [9]. Shen et. al demonstrated that Fe doping of Mn-Ce/TiO₂ non-linearly increased the amount of NH₃ that desorbed during TPD [10]. They did not tie these results to acid sites or overall acidity, but they imply that acid character of the catalyst increased with Fe doping. However, the authors did not normalize the reported results by surface area, and there is insufficient data reported to do precisely. Visual estimation of TPD area from provided figures coupled with reported

surface area measurements of catalysts suggest that acid site density did increase monotonically with Fe doping. Noh et. al. found that the change in basicity with Fe₃O₄ promotion varied by support [11]. Adding Fe₃O₄ to Ce-ZrO₂ and Si-ZrO₂ decreased the density of base sites, but adding Fe₃O₄ to ZrO₂ increased the density of base sites. In this catalytic system, the oxygen vacancy sites were proposed as the active sites for dehydration of ethylbenzene.

5.2. Experimental Methods

5.2.1 Catalyst Synthesis

The Mo₂C was synthesized by the methods described in Section 2.2.1 for incipient wetness. Incipient wetness was selected instead of wet impregnation so that higher loadings of Fe could be achieved; the maximum loading of Fe achievable via wet impregnation is <2% [12]. To avoid oxidation prior to Fe impregnation, the Mo₂C was transferred in a 15% CH₄/H₂ atmosphere to a water-tolerant, oxygen-free glovebox (N₂ atmosphere). Iron was added to the Mo₂C by incipient wetness using Fe(NO₃)₃ (Sigma Aldrich Iron(III) nitrate nonahydrate, ≥99.95% trace metals basis) solutions. The amount of Fe(NO₃)₃ was adjusted to correspond to the equivalent of 0.1, 0.5, and 1.1 equivalent monolayers (ML) of surface coverage, assuming a total site concentration of 10¹⁹ sites m⁻² [13]. The catalyst was transferred back to the synthesis reactor under an Ar atmosphere. The resulting catalyst was dried at 110 °C for 2 h in H₂, then reduced in H₂ at 450 °C for 4 h. After quenching to room temperature, the catalyst was passivated using a 1% O₂/He mixture for at least 6 h. The catalysts were named based on the nominal amount of Fe addition (in terms of ML), so Fe(1.1ML)/Mo₂C represents a Mo₂C catalyst with 1.1 ML of Fe addition.

5.2.2 Catalyst Characterization

Powder X-ray diffraction (XRD) patterns and relative metal loadings were collected using the same methods described in Section 2.2.2. N₂ physisorption isotherms were collected using the same methods described in 3.2.2. Crotonaldehyde conversion experiments were performed in the same manner as described in Section 2.2.3. The catalyst was maintained at the initial temperature for 9 hrs to accommodate for catalyst deactivation, and then maintained at each sequential temperature (275°C, 325°C, 300°C, 350°C) for 3 hrs to allow the catalyst to stabilize.

5.3. Results

5.3.1 Physical Catalyst Characterization

X-ray diffraction patterns for the as-synthesized materials are shown in Figure 5.1. There are no apparent oxide peaks, indicating complete carburization of the precursor. Additionally, the handling and passivation procedures avoided bulk oxidation of the carbide during transfers between the reactor and the glovebox.

The surface area of the parent Mo₂C material was 124.9 m² g⁻¹ (Table 5.1). The addition of just 0.1ML Fe caused a decrease in the surface area, though further Fe addition had a minimal and inconsistent effect on the surface area. The lowest surface area was measured as 64.4 m² g⁻¹ for the Fe(0.5ML)/Mo₂C material. The decrease in surface area affected the micropore and mesopore structures similarly. As seen in Table 5.1, the

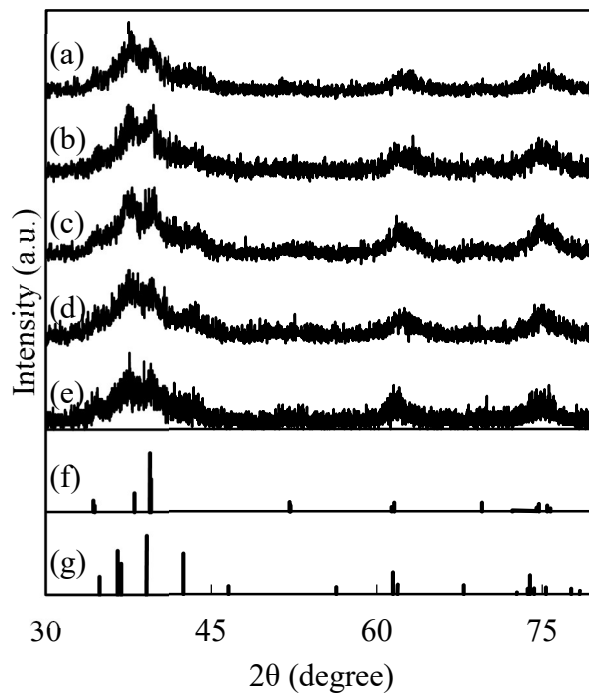
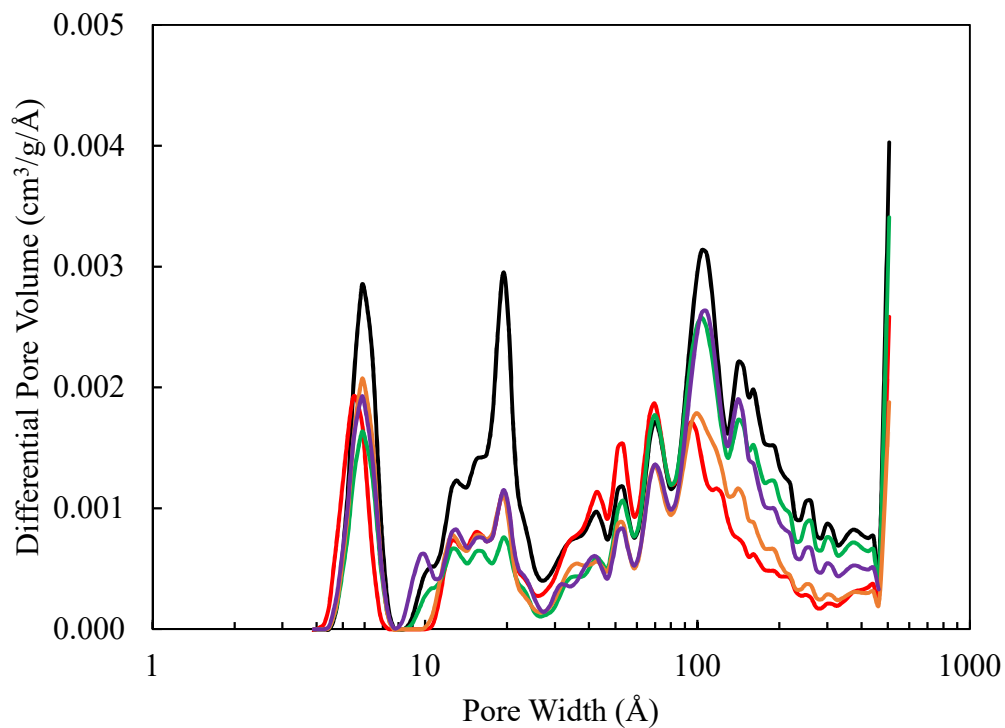


Figure 5.1. X-ray diffraction patterns for (a) Fe(1.1ML)/Mo₂C, (b) Fe(0.7ML)/Mo₂C, (c) Fe(0.5ML)/Mo₂C, (d) Fe(0.1ML)/Mo₂C, and (e) Mo₂C catalysts and peak positions for polycrystalline (f) orthorhombic β-Mo₂C (JCPDF 00035-0787) and (g) cubic α-MoC_{1-x} (JCPDF 00-015-0457).

percentage of surface area attributed to the micropore area ($76 \pm 3 \%$) and mesopore area ($24 \pm 3 \%$) is very similar for all Mo₂C and Fe/Mo₂C catalysts. This is further evidenced in the pore distribution shown in Figure 5.2. Therefore, Fe seemed to reduce surface area

Table 5.1 BET Surface area and DFT pore volumes for all catalysts.

	Nominal Fe Loading (wt %)	Nominal Fe Coverage (ML)	BET Surface Area ($\text{m}^2 \text{g}^{-1}$)	DFT Micropore Area ($\text{m}^2 \text{g}^{-1}$) [%]	DFT Mesopore Surface Area ($\text{m}^2 \text{g}^{-1}$) [%]
Mo_2C	0.0	0	124.9	80.0 [76]	24.8 [24]
$\text{Fe}(0.1\text{ML})/\text{Mo}_2\text{C}$	0.9	0.1	78.5	57.0 [78]	15.9 [22]
$\text{Fe}(0.5\text{ML})/\text{Mo}_2\text{C}$	4.6	0.5	64.4	44.1 [73]	16.3 [27]
$\text{Fe}(0.7\text{ML})/\text{Mo}_2\text{C}$	6.3	0.7	69.2	51.9 [79]	13.4 [21]
$\text{Fe}(1.1\text{ML})/\text{Mo}_2\text{C}$	9.5	1.1	71.4	52.5 [75]	17.7 [25]

**Figure 5.2.** DFT pore volume distribution for Mo_2C (—), $\text{Fe}(0.1\text{ML})/\text{Mo}_2\text{C}$ (—), $\text{Fe}(0.5\text{ML})/\text{Mo}_2\text{C}$ (—), $\text{Fe}(0.7\text{ML})/\text{Mo}_2\text{C}$ (—), and $\text{Fe}(1.1\text{ML})/\text{Mo}_2\text{C}$ (—).

by non-specifically reducing both micropores and mesopores.

5.3.2 Active Site Concentrations

NH_3 -TPD profiles are shown in Figure 5.5, and are scaled so that the area under the TPD profile is representative of the acid site concentration of that catalyst. The acid site concentrations are plotted in Figure 5.3. The acid site concentration increases slightly with 0.1ML of Fe, but then decreases with increasing amounts of Fe up to 0.7ML and appears to remain relatively constant with additional Fe of 1.1ML. At 1.1ML of Fe, the acid site concentration is approximately cut in half compared to the concentration for Mo_2C .

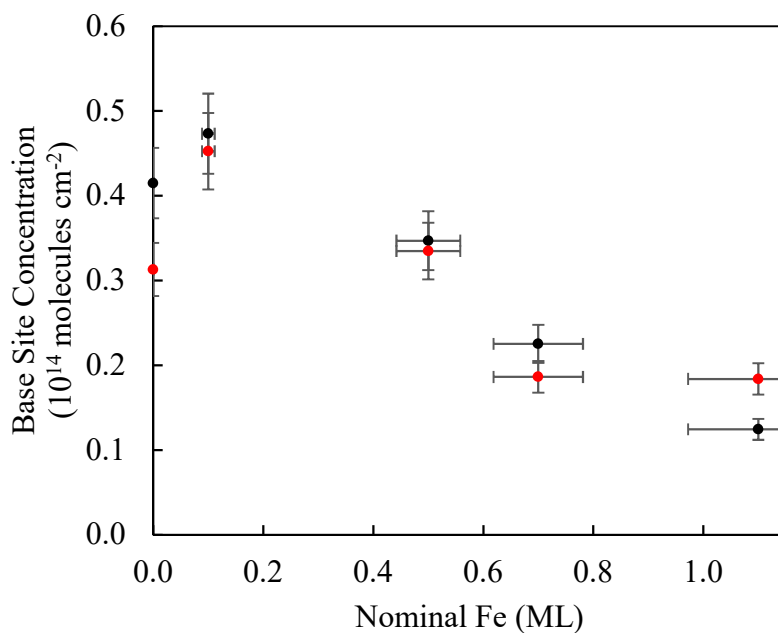


Figure 5.3. Site concentrations of base (•) and acid sites (•) on the surface of Mo_2C catalysts with increasing Fe coverage. Error bars represent 95% confidence interval.

CO_2 -TPD profiles are shown in Figure 5.5, and are scaled in the same way as the NH_3 -TPD profiles. The CO_2 -TPD concentrations are shown in Figure 5.3. The trend of total base site concentration follows closely with that of the acid site concentrations; the

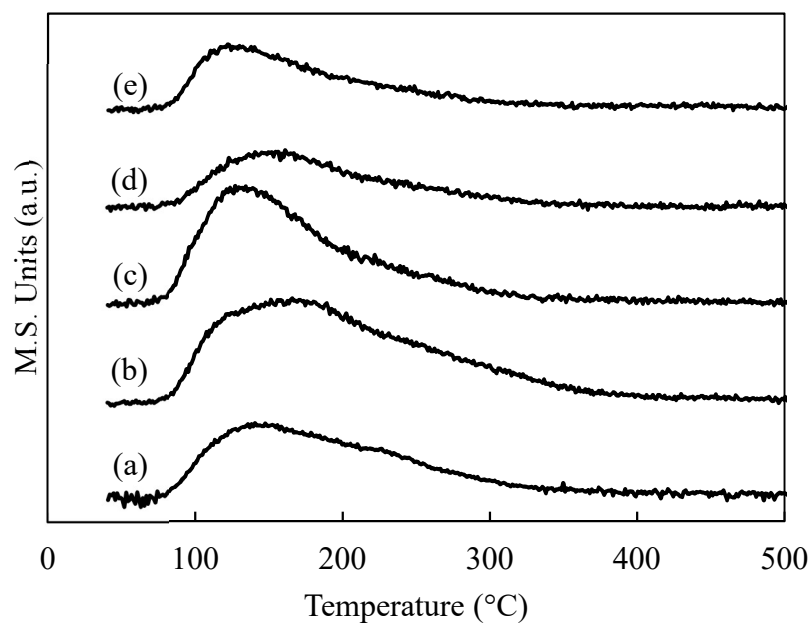


Figure 5.5. NH₃-TPD profiles of (a) Mo₂C, (b) Fe(0.1ML)/Mo₂C, (c) Fe(0.5ML)/Mo₂C Mo₂C (d) Fe(0.7ML)/Mo₂C, and (e) Fe(1.1ML)/Mo₂C catalysts where M.S. signal has been normalized by the surface area of the catalysts.

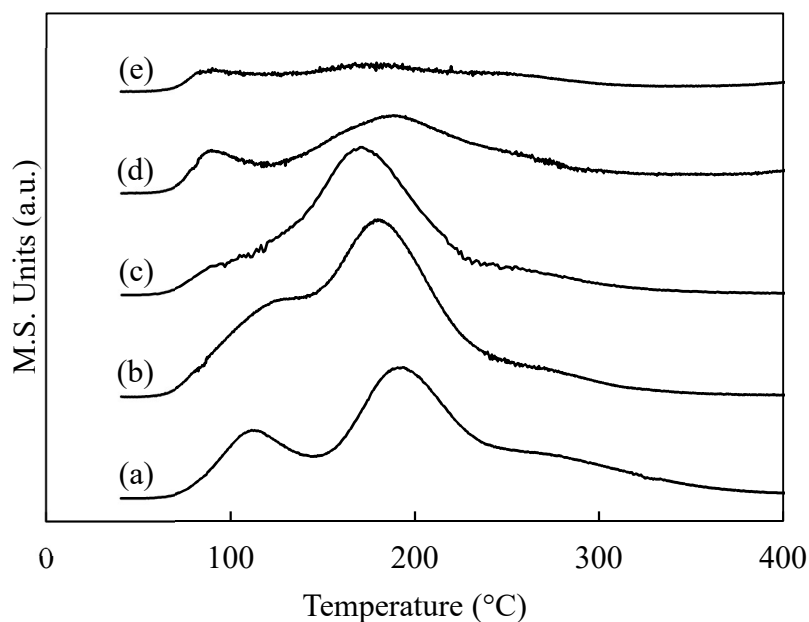


Figure 5.5. CO₂-TPD profiles of (a) Mo₂C, (b) Fe(0.1ML)/Mo₂C, (c) Fe(0.5ML)/Mo₂C Mo₂C (d) Fe(0.7ML)/Mo₂C, and (e) Fe(1.1ML)/Mo₂C catalysts where M.S. signal has been normalized by the surface area of the catalysts.

concentration increases slightly with 0.1ML of Fe, but then decreases with increasing

amounts of Fe up to 0.7ML. However, it appears to continue to decrease with 1.1ML Fe. The overall decrease in base site concentration from Mo₂C to Fe(1.1ML)/Mo₂C is larger than the decrease for acid site concentration.

From the CO₂-TPD profiles, it is clear that the profiles are constructed of multiple distinct peaks, and therefore the TPD profiles were deconvoluted for deeper analysis. The CO₂-TPD spectra were deconvoluted into peaks that were 30% Lorentzian and 70% Gaussian with a linear baseline using the peak fitting software CasaXPS, and the deconvolution is shown in Figure 5.7. Three peaks were selected because it was the minimum number necessary to achieve a good fit. First, each peak was fit with three peaks and optimized without constraints using the peak fitting software, and the FWHMs were noted. The full-width-half-maxima (FWHM) of each peak were then constrained so that the FWHM of each peak was constant for all TPD spectra; the FWHM represented the average of the FWHMs of the peaks when they were not constrained. After fitting, the correlation coefficients (r) were determined for each set of peak areas, and all were less than 0.6. Since no one peak's area was well-correlated with another peak's area, the three peaks were each considered independent adsorption sites. The first, second, and third peaks will be referred to as weak, medium, and strong base sites, respectively. The peak position for each peak was identified as the temperature of the maximum of that peak and are displayed in Table 5.2. The site concentrations are presented in Table 5.3 and plotted in Figure 5.6.

Table 5.2. Peak location (°C) of deconvoluted peaks for Fe/Mo₂C catalysts, and the correlation coefficient of the peak locations and the ML of Fe.

	Weak Base	Medium Base	Strong Base
Mo ₂ C	113	200	299
Fe(0.1ML)/Mo ₂ C	112	182	274
Fe(0.5ML)/Mo ₂ C	98	171	267
Fe(0.7ML)/Mo ₂ C	97	181	239
Fe(1.1ML)/Mo ₂ C	94	160	229
R ²	0.87	0.73	0.89

Table 5.3. Site concentrations of the deconvoluted base site types for the Fe/Mo₂C catalysts.

Catalyst	Site Concentration (10 ¹⁴ molecules cm ⁻²)				
	Weak Base [%]	Medium Base [%]	Strong Base [%]	Total Base	Total Acid
Mo ₂ C	0.07 [18]	0.24 [59]	0.09 [23]	0.41	0.31
Fe(0.1ML)/Mo ₂ C	0.08 [17]	0.34 [72]	0.05 [11]	0.47	0.45
Fe(0.5ML)/Mo ₂ C	0.02 [7]	0.28 [81]	0.04 [13]	0.35	0.33
Fe(0.7ML)/Mo ₂ C	0.04 [17]	0.11 [51]	0.07 [32]	0.23	0.19
Fe(1.1ML)/Mo ₂ C	0.03 [20]	0.06 [45]	0.04 [35]	0.12	0.18

The medium-strength base sites account for the majority (69%) of the Mo₂C base site concentration and changes in the medium-strength base site concentration are the main driver of the changes to the total base site concentration; in contrast, the weak and strong base site concentrations are relatively invariant with Fe loading. The peak location of all

three peaks do not monotonically decrease with Fe promotion, but the peak locations do mostly decrease with Fe promotion, and there is good correlation (all $R^2 > 0.70$) between peak location and nominal Fe loading for all three peaks. Consequently, Fe is shown to typically lead to a decrease in the peak location temperature for all three peaks. The strong base sites were found to have the largest change in peak location with Fe loading, and therefore the three peaks all desorbed within a smaller range with increasing Fe promotion. Decreasing desorption temperature is indicative of decreasing strength of the sites, suggesting that all three sites were weakened with Fe loading, that the strong base sites experienced the most change in site strength with Fe loading, and that the strengths of all three base site types became more similar in strength with Fe loading.

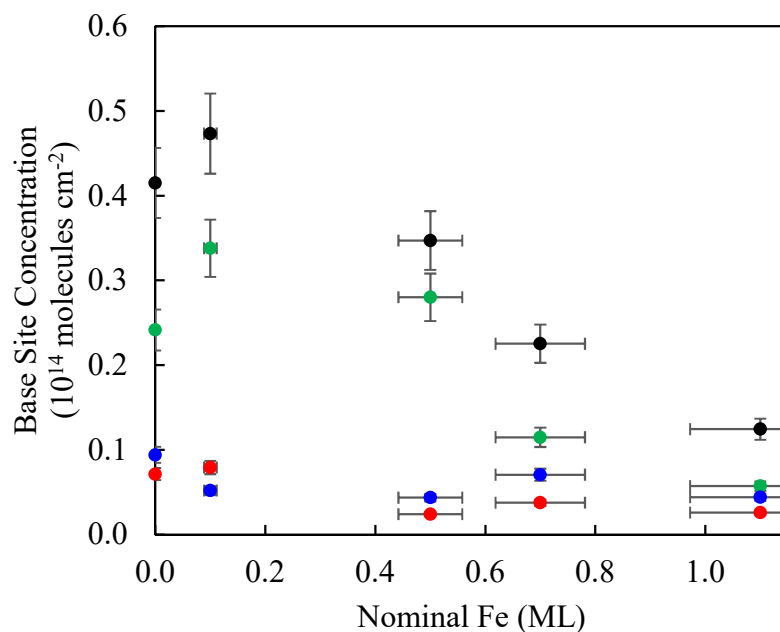


Figure 5.6. Site concentrations of weak (•), medium (•), strong (•), and total (•) base sites on the surface of Mo₂C catalysts with increasing Fe coverage. Error bars represent 95% confidence interval.

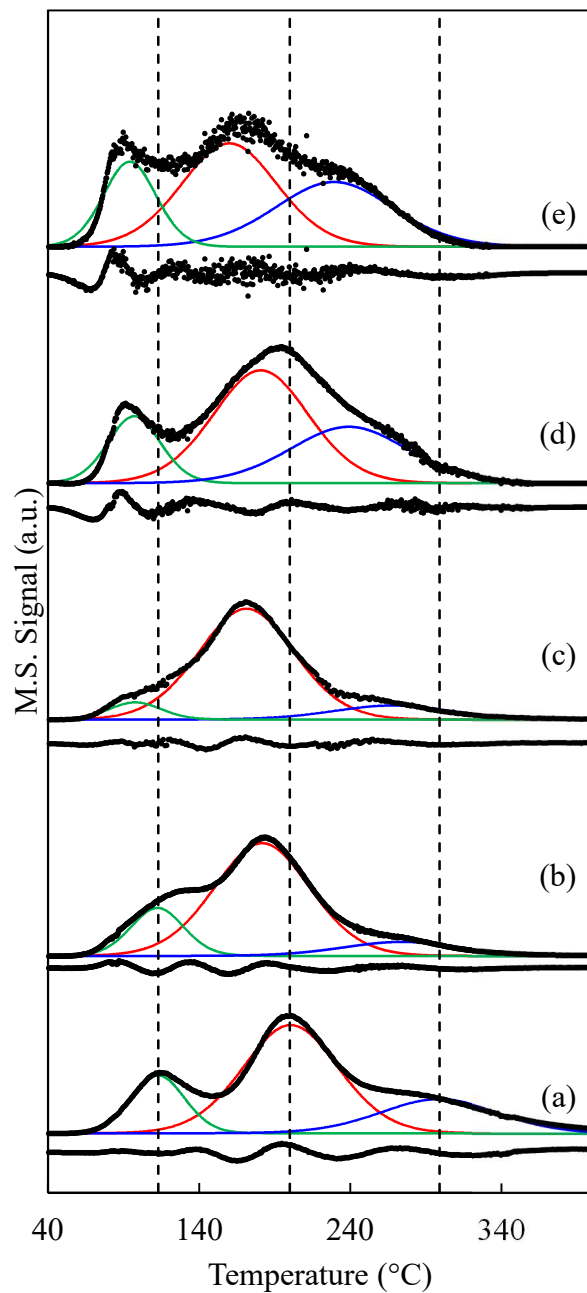


Figure 5.7. Deconvoluted CO₂-TPD profiles of (a) Mo₂C, (b) Fe(0.1ML)/Mo₂C, (c) Fe(0.5ML)/Mo₂C (d) Fe(0.7ML)/Mo₂C, and (e) Fe(1.1ML)/Mo₂C catalysts. Deconvoluted peaks are shown in green, red, and blue, and residuals (difference between raw spectrum and fit) are displayed below each TPD. The M.S. signals have been scaled so that the profiles are of the same height for ease of viewing. Dashed lines represent the peak maxima of Mo₂C).

5.3.3 Activity

Catalyst deactivation was analyzed for 9 hr TOS at 350 °C. Normalized activity profiles for each catalyst were compared where:

$$a(t) = \frac{\text{rate}(t)}{\text{maximum rate}}$$

Catalyst deactivation profiles are shown in Figure 5.8. Each profile was fit to several known deactivation models in order to determine the applicability of various deactivation models including linear, exponential, hyperbolic, and reciprocal models. The forms of these models are given in Chapter 2, and R^2_{adj} and the fitted parameters are shown in Table 5.4. Here, k_d is the specific decay constant and t is the time on stream. The best fit for all catalysts ($R^2_{\text{adj}} > 0.98$) was the reciprocal model, which is consistent with deactivation by carbon deposition, or coking [14,15].

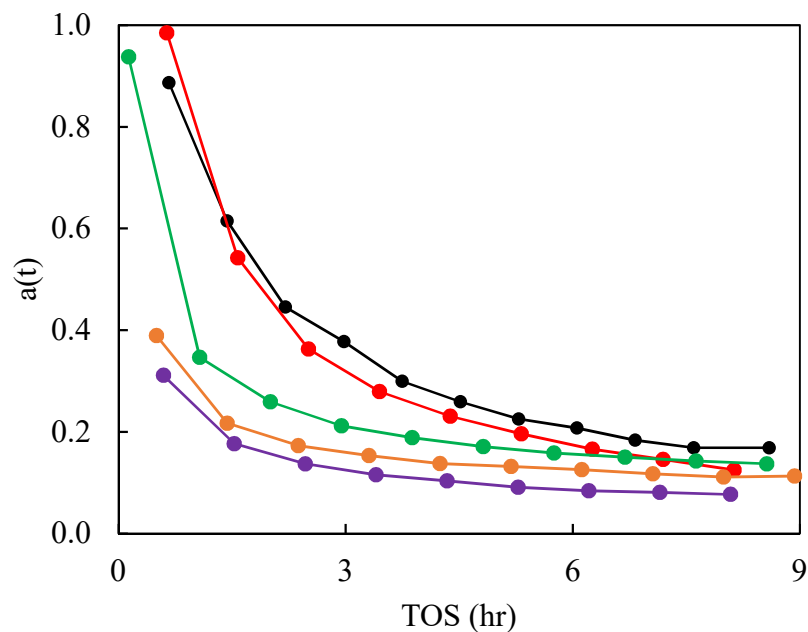


Figure 5.8. Catalyst deactivation profiles for Mo_2C (–), $\text{Fe}(0.1\text{ML})/\text{Mo}_2\text{C}$ (–), $\text{Fe}(0.5\text{ML})/\text{Mo}_2\text{C}$ (–), $\text{Fe}(0.7\text{ML})/\text{Mo}_2\text{C}$ (–), and $\text{Fe}(1.1\text{ML})/\text{Mo}_2\text{C}$ (–).

Table 5.4. Results from nonlinear regression of activity data to four empirical decay rate laws.

	Linear		Exponential		Hyperbolic		Reciprocal		
	R^2_{adj}	k_d (hr^{-1})	R^2_{adj}	k_d (hr^{-1})	R^2_{adj}	k_d (hr^{-1})	R^2_{adj}	k_d (hr^{-1})	A_0
Mo_2C	0.70	0.08	0.92	0.28	0.92	0.54	0.98	0.64	0.71
$\text{Mo}_2\text{C}/(0.1\text{ML})$	0.62	0.09	0.89	0.33	0.82	0.59	0.99	0.75	0.71
$\text{Mo}_2\text{C}/(0.5\text{ML})$	0.35	0.06	0.73	0.45	0.94	1.21	1.00	0.47	0.36
$\text{Mo}_2\text{C}/(0.7\text{ML})$	0.49	0.02	0.68	0.18	0.88	0.53	0.98	0.46	0.28
$\text{Mo}_2\text{C}/(1.1\text{ML})$	0.58	0.02	0.80	0.24	0.96	0.79	1.00	0.55	0.23

Activity and conversion measurements for the catalysts are shown in Table 5.5, and show a reduction in the crotonaldehyde consumption rate of up to ca. 60% with 1.1ML of Fe promotion on Mo_2C from the parent Mo_2C material. The trend is not monotonic, and the rate decreases with 0.1ML Fe promotion but increases with 0.5ML Fe promotion,

though the rate is still less than that for the parent Mo₂C catalyst. The Fe(0.1ML)/Mo₂C activity results were repeated and showed good agreement between the two runs (crotonaldehyde consumption rate \pm 3%), and the average results are reported.

Table 5.5. Crotonaldehyde consumption rate and conversions for the Mo₂C and Fe/Mo₂C catalysts after 9 hr TOS at 350 °C.

	Crotonaldehyde Consumption Rate ($\mu\text{mol sec}^{-1} \text{ m}^{-2}$)	Conversion (%)
Mo ₂ C	1.09	16.2
Fe(0.1ML)/Mo ₂ C	0.71	13.2
Fe(0.5ML)/Mo ₂ C	0.91	14.0
Fe(0.7ML)/Mo ₂ C	0.68	11.2
Fe(1.1ML)/Mo ₂ C	0.46	7.9

5.3.4 Selectivity

For Fe/Mo₂C catalysts, eight distinct product groups were detected. As in previous chapters, butadiene, butene, 3-butenal, and butyraldehyde were detected. In addition, products with GC higher retention times were identified that constituted up to ca. 30% of the carbon selectivity. These higher retention time products were separated into four product groupings and identified by their retention times, such that higher retention times indicated larger molecular weight and polarity; these product groups are P24, P26, P28, and P35. These product groups are likely C₈ and C₁₂ products that arise from coupling of crotonaldehyde or C₄ products. Formation of C₈s from crotonaldehyde hydrogenation has been previously reported to form compounds such as 2,4,6-octatrienal and has been suggested to occur via dimerization, polymerization, condensation, and aldol condensation [16–19].

Productivity results are displayed in Figure 5.10. The Fe(0.1ML)/Mo₂C activity results were repeated and showed good agreement between the two runs (carbon selectivity $\pm 3\%$), and the average results are reported. Butadiene, butene, and butyraldehyde productivity decreased with Fe promotion, and an exponential model gave good fits ($R^2 = 0.96$, 0.98 , and 0.99 , respectively). The productivities of these three products correlated strongly with another; Butadiene productivity correlated with butyraldehyde and butene productivity ($R^2 = 0.98$ and 0.98 , respectively). P24, P26, and P28 productivities also decreased significantly with 0.1ML promotion, but these did not fit well to a linear or exponential decay model. 3-Butenal productivity was slightly decreased with 0.1ML of Fe promotion but returned to values similar to that on the native Mo₂C for $>.1$ ML Fe promotion. P35 was not observed to form on the parent Mo₂C, increased productivity with slight Fe promotion and reached a maximum for .5ML, and then decreased upon further Fe

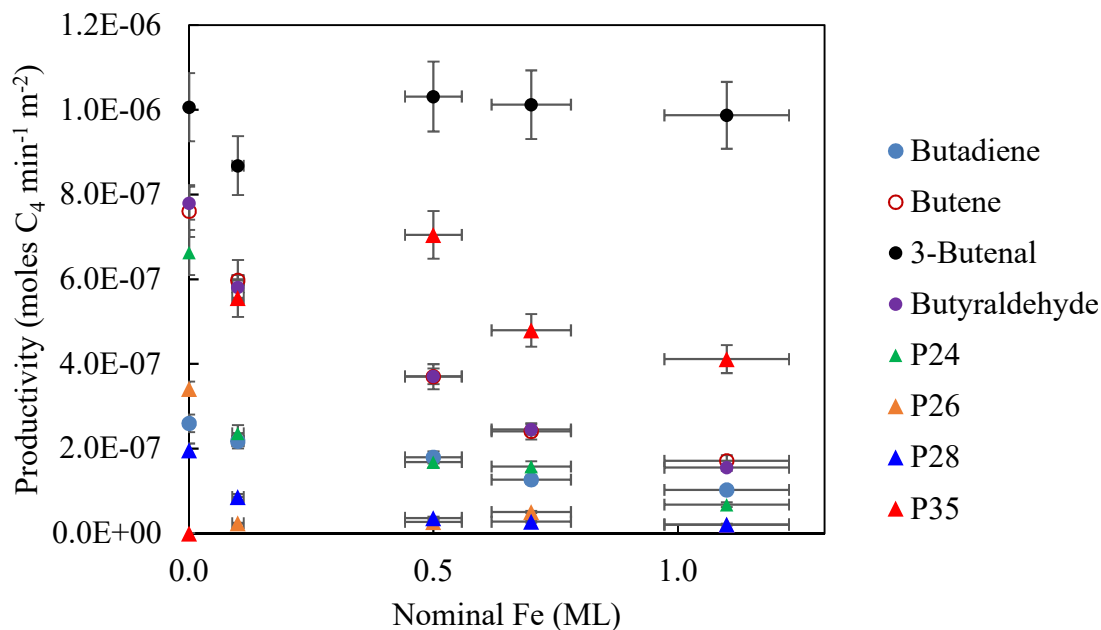


Figure 5.9. Carbon productivity for Mo₂C and Fe/Mo₂C catalysts at 350 °C after 9 hr TOS.

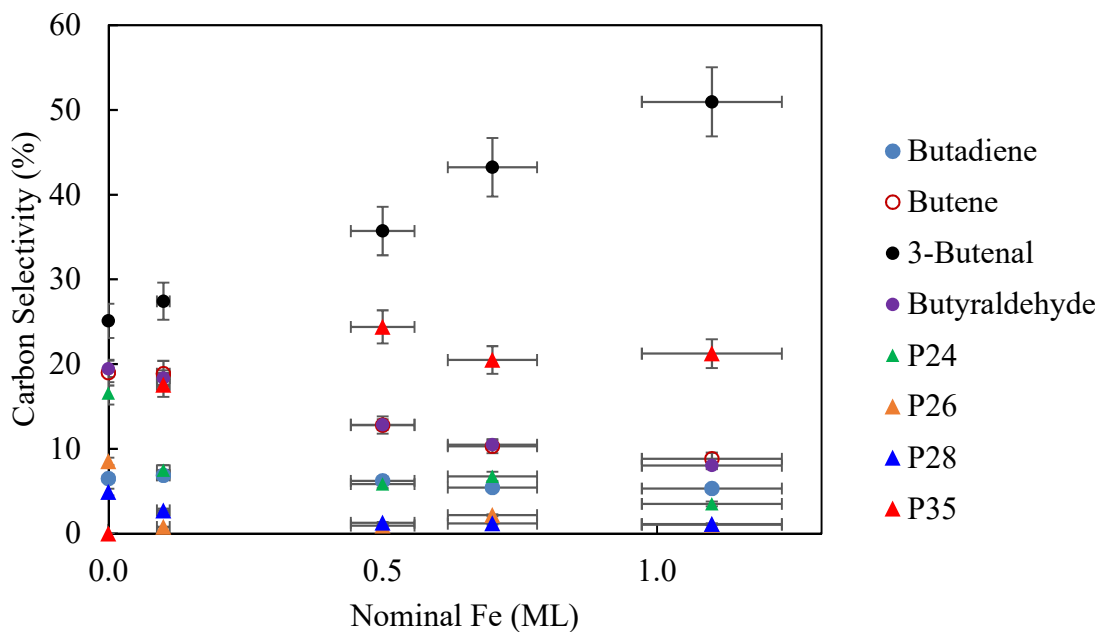


Figure 5.10. Carbon selectivity for Mo₂C and Fe/Mo₂C catalysts at 350 °C after 9 hr TOS.

promotion.

Carbon selectivity results are reported in Figure 5.9. Butadiene selectivity was relatively constant for all catalysts. Butene and butyraldehyde selectivity decreased linearly ($R^2 = 0.94$ and 0.97 , respectively) with Fe promotion. The correlation coefficient of the butene and butyraldehyde selectivities was 0.995 . 3-Butenal selectivity increased linearly ($R^2 = 0.99$) with Fe promotion; P26 and P28 selectivities were virtually eliminated with Fe promotion. P24 selectivity decreased with small amounts of Fe promotion but was otherwise insensitive to Fe promotion. P35 selectivity was greatly enhanced with Fe promotion but was otherwise insensitive to Fe promotion.

5.3.5 Linking Active Sites and Productivity

First, changes in active site concentration were compared to changes in the overall crotonaldehyde consumption rate. While the acid and base site concentrations both reach a maximum at 0.1ML Fe, the rate decreases with 0.1ML Fe, then has a slight rebound in rate for .5ML before being further depressed with more Fe promotion. The site concentrations and overall consumption rates do not trend together, and therefore there is not a constant turnover frequency of crotonaldehyde on the total active site concentration, or on the individual (acid and base) site concentrations.

Next, individual product productivity and measurements of active site measurements are considered. It is clear that some of these pairings of parameters follow similar trends. For Fe/Mo₂C catalysts, all active site types generally decrease with Fe promotion, and the productivity of butadiene, butene, butyraldehyde, P24, P26, and P28 followed a similar trend. However, this cursory analysis does not allow for particular products to be attributed to particular active site types. For a given product, the productivity was plotted as a function of a given active site concentration, and the correlation coefficient (R^2) was determined for that pairing.

These plots are shown in Figure 5.11, Figure 5.12, Figure 5.13, and Figure 5.14, and the R^2 results are given in Table 5.6. As discussed in Chapter 4, the R^2 quantifies the linearity of the turnover frequency; if the productivity change was perfectly proportional to the change in site concentration, the R^2 would be 1. Colloquially, the R^2 represents the percentage of the change in productivity that can be attributed to the site concentration. Here, $R^2 > 0.70$ are taken to be significant, in the sense that the given site type is worthy of further investigation as playing a significant role in that product's productivity.

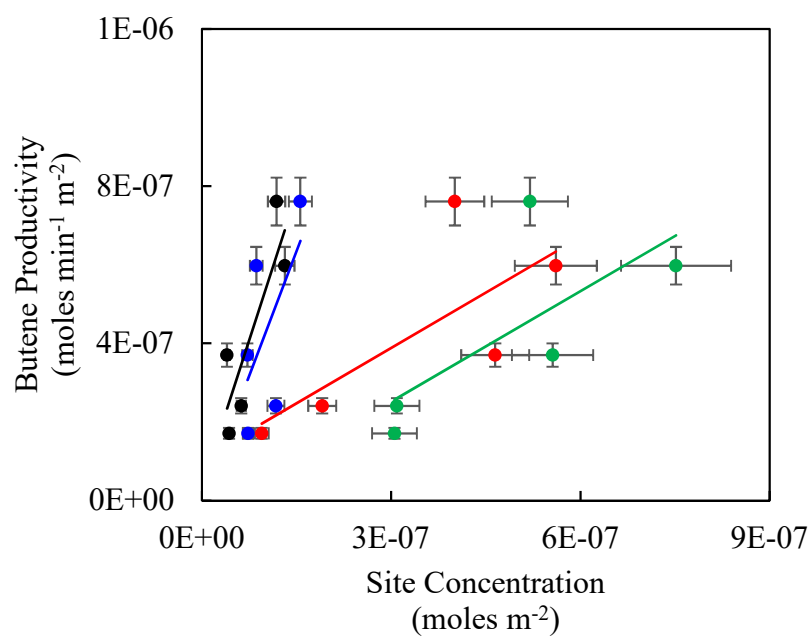
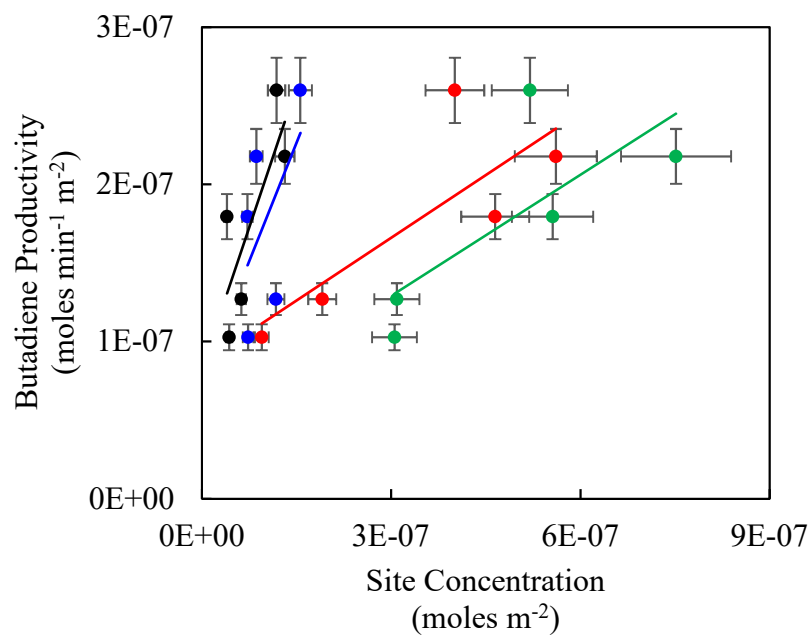


Figure 5.11. Correlation plot between product productivity and weak, medium-strength, strong base sites and acid sites over Mo₂C and Fe/Mo₂C catalysts.

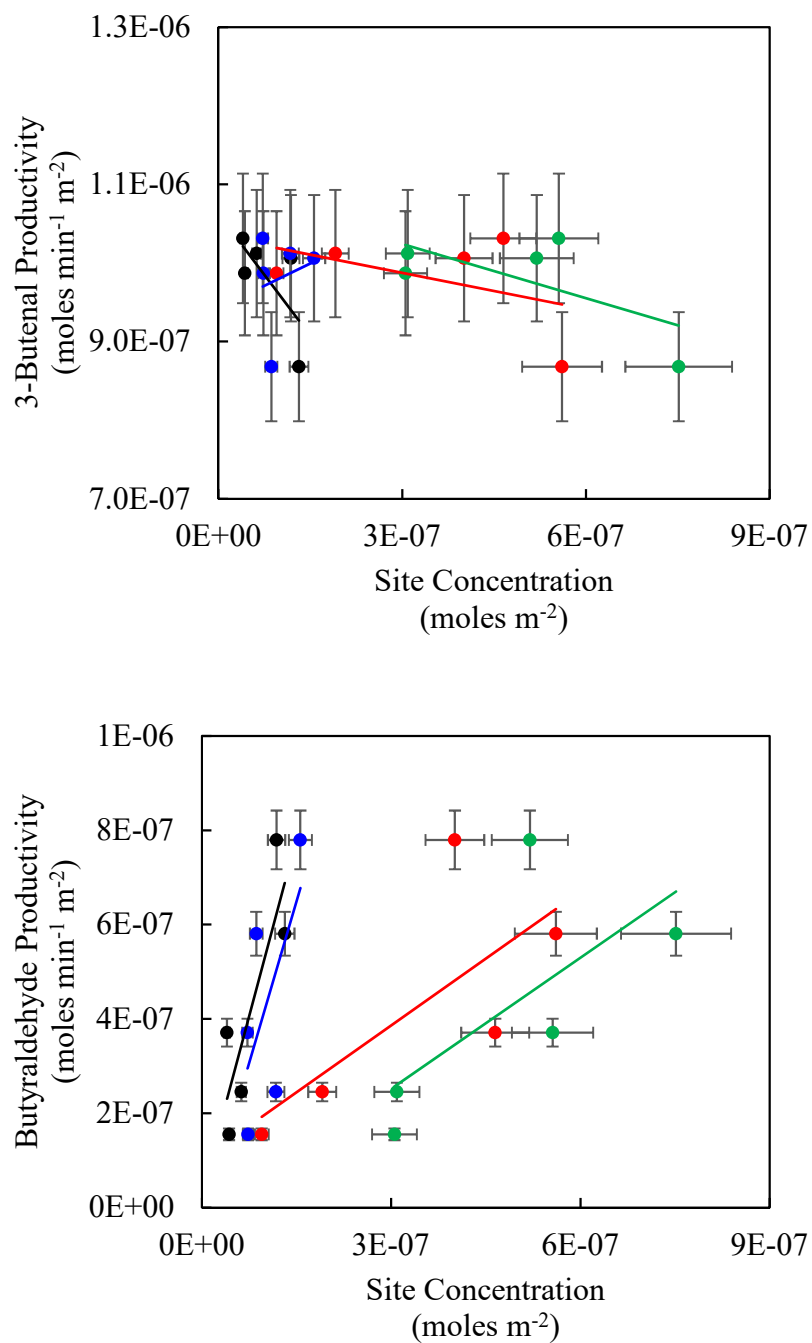


Figure 5.12. Correlation plot between product productivity and weak, medium-strength, strong base sites and acid sites over Mo₂C and Fe/Mo₂C catalysts.

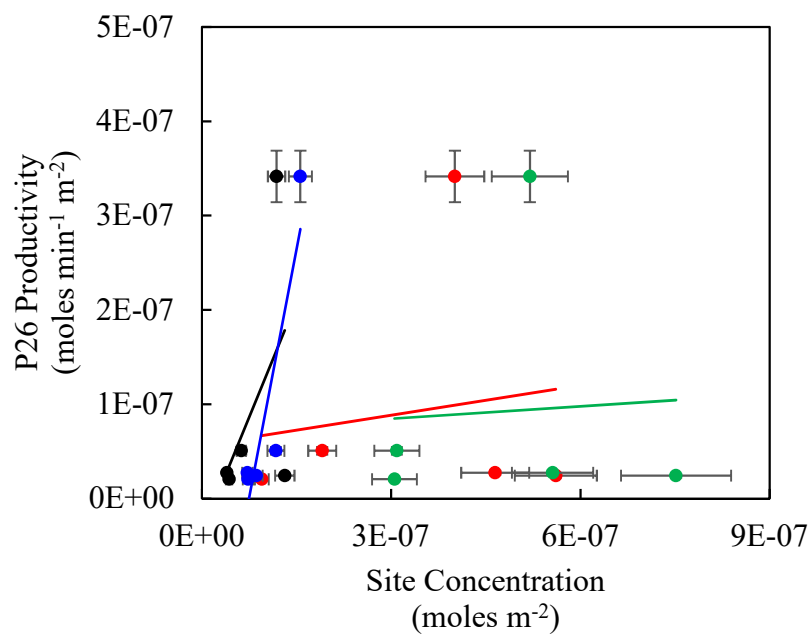
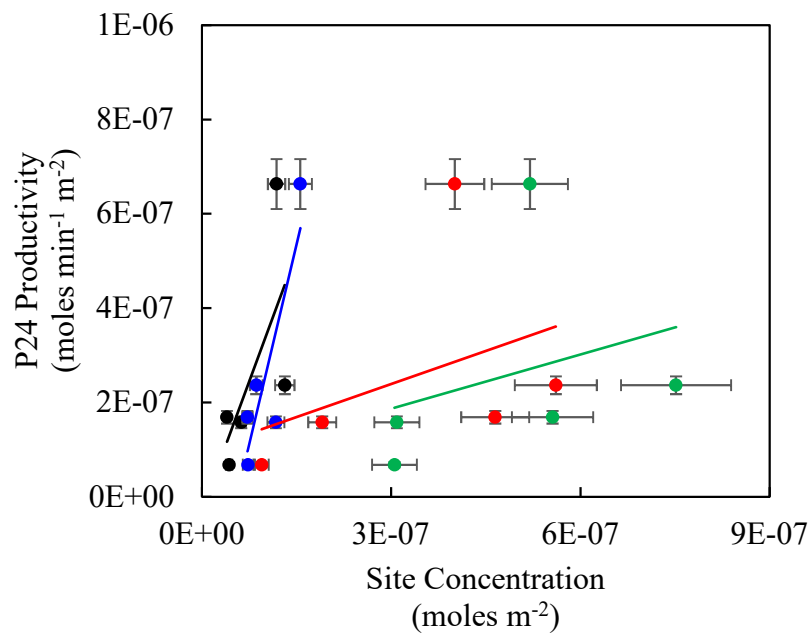


Figure 5.13. Correlation plot between product productivity and weak, medium-strength, strong base sites and acid sites over Mo₂C and Fe/Mo₂C catalysts.

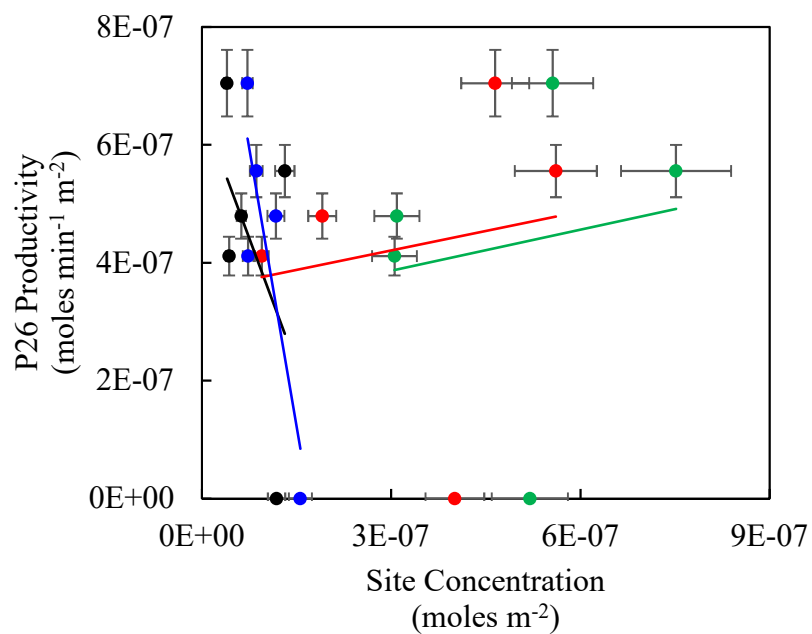
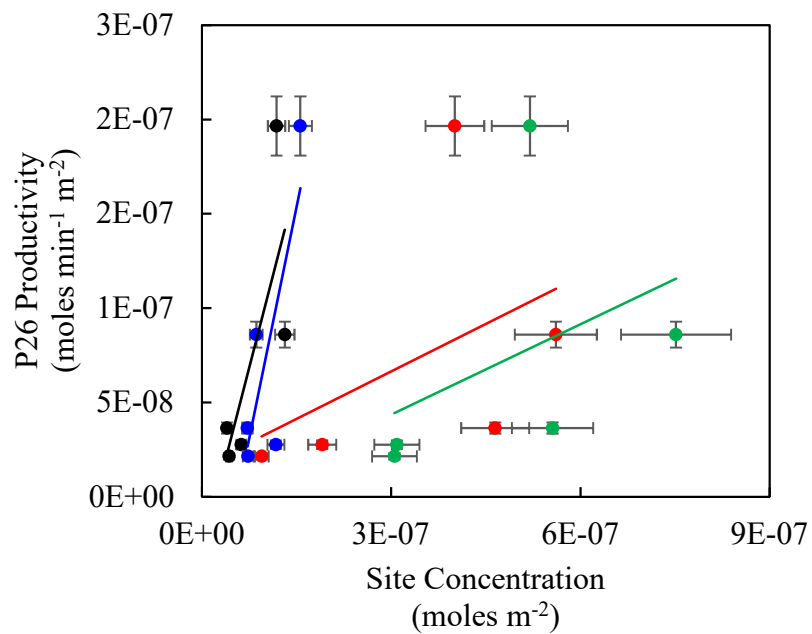


Figure 5.14. Correlation plot between product productivity and weak, medium-strength, strong base sites and acid sites over Mo₂C and Fe/Mo₂C catalysts.

Table 5.6. Correlations between rate of productivity of each product and site concentrations for Mo₂C and Fe/Mo₂C catalysts.

	Total Acid Sites	Weak Base Sites	Medium Base Sites	Strong Base Sites	Total Base Sites
Butadiene	0.56	0.63	0.64	0.31	0.84
Butene	0.51	0.74	0.54	0.37	0.78
3-Butenal	0.44	0.47	0.21	0.04	0.23
Butyraldehyde	0.47	0.71	0.52	0.41	0.76
P24	0.09	0.44	0.15	0.74	0.36
P26	0.00	0.25	0.02	0.81	0.14
P28	0.17	0.58	0.20	0.63	0.43
P35	0.03	0.22	0.03	0.72	0.01

Eight product and site couplings were found to have $R^2 > 0.70$. Only weak base, strong base, and total base sites were found to have significant correlations, suggesting that acid and medium base sites were not monofunctional sites for any of the products. Six of the eight detected product groups (Butadiene, butene, butyraldehyde, P24, P26, and P35) were found to have significant correlations with a site concentration, suggesting that 3-butenal and P28 are either formed on a site type that was not measured, or are formed bifunctionally on multiple site types whose concentrations change independent of one another. For butene, butyraldehyde, and butadiene, the correlation with total base site concentration were each stronger than that for weak base site concentration. At this point, it is inconclusive whether the weak base site is the specific active site for the butene, butyraldehyde, and butadiene production, or whether all base sites play a role in their formation.

5.4. Discussion

Small amounts (.1ML) Fe promotion of Mo₂C reduced surface area of Mo₂C, but higher amounts of Fe did not further reduce the surface area of Mo₂C. In addition, the reduction in surface area was found to be attributed to a proportional reduction in micropore and mesopore surface area. This is a different trend than that observed for K promotion in Chapter 3, in which K specifically reduced the micropore surface area of the Mo₂C; Fe did not appear to preferentially reduce the micropore structure, but instead unselectively reduced the micropore and mesopore structures. Since Fe crystallites were not observed in XRD, the Fe is likely well-dispersed on the surface. Since the reduction in surface area is approximately equal across all Fe loadings, it is unlikely that Fe is physically blocking pores; if this were true, surface area should decrease further with additional promotion. Instead, Fe could be inducing a structural change in the catalyst during reduction – perhaps an increase in crystallite size – that reduces surface area but is not sensitive to amount of promotion.

Total acid and base site concentrations were found to trend together with Fe promotion (correlation = 0.85); both site concentrations increased with .1ML of Fe and reached a maximum, but then decreased upon further Fe promotion. However, the base site concentration of the parent Mo₂C is not statistically different from that of the Fe(0.1ML)/Mo₂C and Fe(0.5ML)/Mo₂C catalysts. Therefore, the base site concentration remained essentially constant with up to 0.5ML Fe promotion but decreased with 0.7ML and 1.1ML Fe promotion. Still, the concentration of the medium-strength base site of Fe(0.1ML)/Mo₂C was significantly different (higher) than that of the parent Mo₂C, and then decreased with further Fe promotion. The medium-strength base sites accounted for

most of the total base sites, so this trend was important. At low and medium loadings, Fe preferentially deposited on and/or block medium-strength base sites. In one report on the effect of Fe promotion on acid and base properties, Kurokawa et. al. found that 3 wt % Fe promotion of MgO catalyst slightly reduced base site concentration and created acidic domains while also shifting selectivity of dehydrogenation and dehydration of isopropyl alcohol [20]. Since the authors did not report results for different Fe loadings, it is difficult to compare the trends found for Fe promotion on Mo₂C.

The acid site concentrations of Mo₂C and Fe(0.5ML)/Mo₂C were statistically equal, while the acid concentration of Fe(0.1ML)/Mo₂C was higher. Kurokawa suggested that the Fe ion sitting on the surface may itself be the location of the acid site [20]. Reports of the acidity of Fe supported on SiO₂, an amphoteric support, are conflicting though; Yu et. al reported Fe/SiO₂ (0.1 wt%) had no measurable acidity by NH₃ TPD [21], while Ates found the amount of NH₃ desorbed during TPD increased with Fe up to 0.90 wt% for Fe/SiO₂ [22]; if Fe domains on the Mo₂C surface are the acid site location, it may take on this property from its electronic interaction with the support.

Through non-linear regression of the activity during initial TOS, Fe/Mo₂C catalysts were found to match well to the reciprocal deactivation model, which is known to indicate deactivation by carbon deposition, or coking. This contrasts with findings in Chapter 2 for Fe(0.1ML)/Mo₂C catalyst prepared by incipient wetness, which was found to match best to the exponential model of decay, which is associated with deactivation by poisoning. The implication is that the impregnation method of Fe on Mo₂C affects the deactivation mechanism. Comparing thermogravimetric analysis (TGA) results of post-reaction samples of Fe/Mo₂C prepared by wet impregnation and incipient wetness could be used to

confirm the degree to which coking contributes to deactivation of each.

Except for 0.1 ML of Fe promotion, crotonaldehyde consumption rate decreased linearly with Fe promotion. With 0.1ML of Fe, the crotonaldehyde consumption rate fell between that of Fe(0.5ML)/Mo₂C and Fe(0.7ML)/Mo₂C. As mentioned, the 0.1ML measurements were repeated and good agreement was found between runs. This dip in activity can be attributed to a dip in productivity of 3-butenal, as shown in Figure 5.9. In addition, Fe(0.1ML)/Mo₂C also falls in a transition region where P35 productivity is increasing with Fe promotion, and butene, butyraldehyde, P24, P26, and P28 productivity is decreasing. The rate of P35 productivity increase is not outweighed by the rate of productivity decrease of the other products, and this discrepancy further contributes to the suppressed crotonaldehyde consumption rate at 0.1ML.

Butene, butadiene, and butyraldehyde, all hydrogenated C₄ products, were highly correlated in their productivity (and selectivity). It follows that they are all formed on the same active site, or that they form as secondary products of one another, such that changes in the productivity of the primary product directly affect the productivity of the secondary product(s). In Chapter 4, butene was proposed to form from butadiene, which formed from butyraldehyde for K/Mo₂C catalysts. Productivity of all products except 3-butenal and P35 was observed to decrease with Fe promotion. Butyraldehyde, butadiene, and butene productivity was observed to decrease exponentially with Fe promotion ($R^2 > 0.89$). In another report, CO hydrogenation activity on Ni/SiO₂ was found to decrease exponentially with K promotion, but the authors did not comment on the significance of the decay model [23]. Exponential decay does offer an interesting clue as to the mechanism of productivity decrease. Small additions of Fe reduce productivity much more than medium and large

additions of Fe, which rules out the possibility that Fe geometrically blocking individual active sites linearly proportional to the amount of Fe addition. A possibility arises: Small additions of Fe disperse well on the surface and block active sites, but at higher loadings, Fe did not disperse as well and instead of creating more Fe domains, the size of the Fe domains increased. Then, the marginal decrease to surface (hydrogenation active sites) coverage decreased with medium and high Fe loadings, but more height was added to the Fe domains.

A remaining question though, is how Fe creates changes in the catalyst surface to induce these changes in productivity and selectivity, and which are the relevant active site(s). Through correlating active site concentrations with productivity, weak base sites and strong base sites were found to correlate with the productivity of one or more product. This is a non-obvious finding; total acid, total base, and medium-strength base site concentrations were more affected by Fe promotion on an absolute site concentration basis and the changes in concentration seemed to clearly be a function of Fe promotion. However, the range in percent change in site concentration between the parent Mo₂C and Fe-promoted catalysts was similar for all site types. For example, medium-strength base site concentration changed by up to 76% with Fe promotion (1.1ML), and weak base concentration changed by up to 66% (0.1ML). Consequently, there was a wide and consistent range of site concentrations for the correlations. Site concentrations were more valuable if they were well-distributed within the range; an even distribution of concentrations combined with a strong correlation strengthens the conclusion that the site type and product are related. The following statistic was used to quantify the “evenness of spread”:

$$spread = \frac{\sigma_d}{\mu_d}$$

where d is the set of values that consists of the differences in site concentration when they are sorted in ascending order, σ_d is the standard deviation of that set, and μ_s is the mean value of that set. A higher value indicates unevenness in spread, and a lower value indicates more evenly spaced data. Weak base sites and strong base sites had high spreads. Ideally, catalysts would be synthesized that fell in the “middle” region, with weak base site concentration between 0.04 and 0.07×10^{14} molecules cm^{-2} , and strong base site concentration between 0.05 and 0.07×10^{14} molecules cm^{-2} to further confirm the high correlation between these active site types and productivity.

Table 5.7 Spread of active site type concentrations.

	Spread
Total Acid Sites	0.96
Weak Base Sites	1.01
Medium Base Sites	0.55
Strong Base Sites	0.82
Total Base Sites	0.34

However, with the range of weak base site concentrations that were measured in this set of catalysts, weak base sites were found to correlate with butene and butyraldehyde, which also were found to have exponentially decreasing productivity with Fe promotion. As theorized above, the exponential decrease could be related to an exponential change in active sites due to changing dispersion with Fe loading. Those active sites are proposed to be the weak base sites.

5.5. Summary

A series of Fe/Mo₂C catalysts were evaluated for their activity and selectivity in crotonaldehyde conversion and compared to the performance of Mo₂C. All catalysts were found to have deactivation profiles that matched best to a reciprocal model, which was indicative of coking. Fe promotion decreased the per-surface area rate, though the decrease was not a monotonic function of Fe promotion. Total base site concentration was intransient with Fe up to 0.5ML, and then decreased upon further promotion. Acid site concentration increased with 0.1ML Fe, but then decreased with further promotion. Productivity decreased exponentially with Fe promotion for butadiene, butenes, and butyraldehyde, which was proposed to be a consequence of changing Fe dispersion and particle size with Fe promotion. Through correlations between site concentrations and productivity, weak base and strong base sites were identified as active sites responsible for changing selectivity on Fe/Mo₂C catalysts.

5.6. References

- [1] V. Ponec, On the Role of Promoters in Hydrogenations on Metals; α , β -Unsaturated Aldehydes and Ketones, *Applied Catalysis A: General* 149 (1997) 27–48.
- [2] T. B. L. W. Marinelli, S. Nabuurs, V. Ponec, Activity and Selectivity in the Reactions of Substituted α , β -Unsaturated Aldehydes, *Journal of Catalysis* 151 (1995) 431–438.
- [3] D. Goupil, P. Fouilloux, R. Maurel, Activity and Selectivity of Pt–Fe/C Alloys for the Liquid Phase Hydrogenation of Cinnamaldehyde to Cinnamyl Alcohol, *Reaction Kinetics and Catalysis Letters* 35 (1987) 185–193. doi:10.1007/BF02062155.
- [4] S. Sitthisa, W. An, D. E. Resasco, Selective Conversion of Furfural to Methylfuran over Silica-Supported NiFe Bimetallic Catalysts, *Journal of Catalysis* 284 (2011) 90–101. doi:10.1016/j.jcat.2011.09.005.

- [5] R. Olcese, M. M. Bettahar, B. Malaman, J. Ghanbaja, L. Tibavizco, D. Petitjean, A. Dufour, Gas-Phase Hydrodeoxygenation of Guaiacol over Iron-Based Catalysts. Effect of Gases Composition, Iron Load and Supports (Silica and Activated Carbon), *Applied Catalysis B: Environmental* 129 (2013) 528–538. doi:10.1016/j.apcatb.2012.09.043.
- [6] J. Sun, A. M. Karim, H. Zhang, L. Kovarik, X. S. Li, A. J. Hensley, J.-S. McEwen, Y. Wang, Carbon-Supported Bimetallic Pd–Fe Catalysts for Vapor-Phase Hydrodeoxygenation of Guaiacol, *Journal of Catalysis* 306 (2013) 47–57. doi:10.1016/j.jcat.2013.05.020.
- [7] E. C. Sikabwe, R. L. White, Effects of Iron Promoter on Reactions of 1-Butene Adsorbed on Sulfated Zirconias, *Catalysis Letters* 44 (1997) 177–183.
- [8] W.-H. Chen, H.-H. Ko, A. Sakthivel, S.-J. Huang, S.-H. Liu, A.-Y. Lo, T.-C. Tsai, S.-B. Liu, A Solid-State NMR, FT-IR and TPD Study on Acid Properties of Sulfated and Metal-Promoted Zirconia: Influence of Promoter and Sulfation Treatment, *Catalysis Today* 116 (2006) 111–120. doi:10.1016/j.cattod.2006.01.025.
- [9] J. Li, J. Liu, H. Zhou, Y. Fu, Catalytic Transfer Hydrogenation of Furfural to Furfuryl Alcohol over Nitrogen-Doped Carbon-Supported Iron Catalysts, *ChemSusChem* 9 (2016) 1339–1347. doi:10.1002/cssc.201600089.
- [10] B. Shen, T. Liu, N. Zhao, X. Yang, L. Deng, Iron-Doped Mn-Ce/TiO₂ Catalyst for Low Temperature Selective Catalytic Reduction of NO with NH₃, *Journal of Environmental Sciences* 22 (2010) 1447–1454. doi:10.1016/S1001-0742(09)60274-6.
- [11] J. Noh, J.-S. Chang, J.-N. Park, K. Y. Lee, S.-E. Park, CO₂ Utilization for the Formation of Styrene from Ethylbenzene over Zirconia-Supported Iron Oxide Catalysts, *Applied Organometallic Chemistry* 14 (2000) 815–818. doi:10.1002/1099-0739(200012)14:12<815::AID-AOC92>3.0.CO;2-Y.
- [12] J. A. Schaidle, N. M. Schweitzer, O. T. Ajenifujah, L. T. Thompson, On the Preparation of Molybdenum Carbide-Supported Metal Catalysts, *Journal of Catalysis* 289 (2012) 210–217. doi:10.1016/j.jcat.2012.02.012.
- [13] C. N. Satterfield, Heterogeneous catalysis in industrial practice, 2nd ed, McGraw-Hill, New York, 1991.
- [14] C. G. Rudershausen, C. C. Watson, Variables Affecting Activity of Molybdena-Alumina Hydroforming Catalyst in Aromatization of Cyclohexane, *Chemical Engineering Science* 3 (1954) 110–121. doi:10.1016/0009-2509(54)80016-9.
- [15] A. Voorhies, Carbon Formation in Catalytic Cracking, *Industrial & Engineering Chemistry* 37 (1945) 318–322. doi:10.1021/ie50424a010.
- [16] X. Hong, B. Li, Y. Wang, J. Lu, G. Hu, M. Luo, Stable Ir/SiO₂ Catalyst for Selective Hydrogenation of Crotonaldehyde, *Applied Surface Science* 270 (2013) 388–394.

doi:10.1016/j.apsusc.2013.01.035.

- [17] P. Chen, J. Lu, G. Xie, L. Zhu, M. Luo, Characterizations of Ir/TiO₂ Catalysts with Different Ir Contents for Selective Hydrogenation of Crotonaldehyde, *Reaction Kinetics, Mechanisms and Catalysis* 106 (2012) 419–434. doi:10.1007/s11144-012-0435-3.
- [18] B. Campo, G. Santori, C. Petit, M. Volpe, Liquid Phase Hydrogenation of Crotonaldehyde over Au/CeO₂ Catalysts, *Applied Catalysis A: General* 359 (2009) 79–83. doi:10.1016/j.apcata.2009.03.001.
- [19] M. Englisch, A. Jentys, J. A. Lercher, Structure Sensitivity of the Hydrogenation of Crotonaldehyde over Pt/SiO₂ and Pt/TiO₂, *Journal of Catalysis* 166 (1997) 25–35. doi:10.1006/jcat.1997.1494.
- [20] H. Kurokawa, T. Kato, T. Kuwabara, W. Ueda, Y. Morikawa, Y. Moro-Oka, T. Ikawa, Solid Base-Catalyzed Reaction of Nitriles with Methanol to Form α,β -Unsaturated Nitriles, *Journal of Catalysis* 126 (1990) 208–218.
- [21] J. Yu, D. Mao, L. Han, Q. Guo, G. Lu, CO Hydrogenation over Fe-Promoted Rh–Mn–Li/SiO₂ Catalyst: The Effect of Sequences for Introducing the Fe Promoter, *Fuel Processing Technology* 112 (2013) 100–105. doi:10.1016/j.fuproc.2013.03.004.
- [22] A. Ates, C. Hardacre, A. Goguet, Oxidative Dehydrogenation of Propane with N₂O over Fe-ZSM-5 and Fe–SiO₂: Influence of the Iron Species and Acid Sites, *Applied Catalysis A: General* 441–442 (2012) 30–41. doi:10.1016/j.apcata.2012.06.038.
- [23] G.-Y. Chai, J. L. Falconer, Alkali Promoters on Supported Nickel: Effect of Support, Preparation, and Alkali Concentration, *Journal of Catalysis* 93 (1985) 152–160. doi:10.1016/0021-9517(85)90158-7.

CHAPTER 6

Summary and Future Work

6.1. Summary and Conclusions

This dissertation investigated Mo₂C and Mo₂C-supported catalysts for use in upgrading reactions with bio-oil model compounds. The metal promoters on Mo₂C were examined as a method of controlling the activity and selectivity of the conversion of the model compounds in the presence of H₂. The main goal was to identify metal promoters that could be used to control the activity and selectivity of upgrading reactions, to identify the catalyst properties that were predicative of the activity and selectivity, and then to develop relationships between the properties and catalyst performance. By developing such a relationship, the work in this dissertation could be used to design highly selective catalysts for bio-oil upgrading.

Fe, Co, Ni, Cu, Rh, Pd, and K were investigated as promoters of Mo₂C for their activity and selectivity in crotonaldehyde conversion. Rh, Pd, and Co did not significantly affect catalyst selectivity, but Ni, Cu, and K increased the selectivity to the isomerization product, while Fe increased the selectivity to the HDO products. The period 5 promoter metals (Rh and Pd) experienced less reduction in crotonaldehyde consumption rate than the smaller promoter metals. K/Mo₂C and Fe/Mo₂C gave very low selectivity for butyraldehyde, suggesting that they have an affinity for hydrogenation of the C=O bond.

The largest increase in isomerization selectivity was observed with the K-promoted

Mo₂C. While isomerization is not typically a desirable catalyst in bio-oil upgrading, controlling (reducing) its selectivity is desirable. Both acetic acid and crotonaldehyde were used as model compounds, and K promotion up to 0.5ML was found to increase selectivity to the ketonization and isomerization products, respectively. With additional K promotion, the increase in selectivity was incremental acetic acid conversion, and slight reversed for crotonaldehyde conversion, respectively. The change in effect with K promotion beyond 0.5ML may have been due to the changes in K dispersion on the catalyst surface at high loadings compared to low loadings.

Catalyst characteristics that may be the driver of catalyst performance were investigated for K/Mo₂C catalysts. Base, acid, and H* site concentrations were measured via TPD of CO₂, NH₃, and H₂ probe molecules. Base sites increased with K promotion, while acid and H* sites decreased with K promotion. The TPD spectra were deconvoluted to quantify the relative contribution of weak and strong sites for acid and base sites. The active site concentrations were correlated to the productivity of each product to determine whether a site type's concentration was a predictor of productivity for a particular product. Strong correlations (high R²) suggested that site type was responsible for the formation of that product. Through this correlation, base sites were identified as the active site for the dominant product at high K loadings (acetone for acetic acid conversion; 3-butenal for crotonaldehyde conversion).

Catalyst characteristics were then compared with the catalyst performance of Fe/Mo₂C catalysts. Fe was added to Mo₂C in amounts up to 1.1ML via incipient wetness, which was found to decrease overall catalyst activity and shift selectivity.

6.2. Future Work in Current Research Areas

Based on the conclusions of this dissertation, there are three directions in which to follow up on this work. The first would be to apply more extensive characterization to the active site types on Mo₂C-supported catalysts. The second would be to perform upgrading in more realistic conditions. And third, investigate differences in performance between catalysts prepared by wet impregnation versus incipient wetness.

In this work, active site types were quantified via TPD of probe molecules after the catalyst was pre-treated in the same manner as before activity and selectivity measurements. However, additional characterization techniques for active site types could be applied to further describe the sites. These techniques can be divided into *ex situ* and *in situ* techniques. *Ex situ* techniques are applied in non-reactive environments; TPD of probe molecules is an *ex situ* technique. For example, TPD of n-propylamine and ethylamine could be used to differentiate between Lewis and Brønsted acid site concentrations [1,2]. Fourier-transform infrared spectroscopy (FTIR) with probe molecules, including pyridine, can also be used to distinguish Lewis and Brønsted acidity [3]. *In situ* techniques are applied in a reactive environment, while the upgrading reaction takes place. Site poisons could be fed to the reactor such that a particular site type is selectively titrated, similar to experiments performed by Sullivan et. al. [4]. The productivity of products that are formed on that site type will decrease to zero. Additional kinetic information can be gleaned from this type of experiment, including more precise turnover frequencies. Both *in situ* and *ex situ* characterization should be combined with density functional theory (DFT) modeling to conclusively identify the identity of the acid and base sites on modified Mo₂C surfaces.

Another area this research could take would be to determine the applicability of this work's findings in more realistic upgrading conditions. First, model compounds or a mixture thereof could be mixed with other molecules present in bio-oil, especially water. As described in Chapter 1, bio-oil vapor contains a high percentage of water. Mo₂C has mostly been found to be unstable in hydrated reactive environments, deactivating after short TOS [5]. Theoretical work has suggested this may be due to water preferentially and reversibly binding to Mo surface sites [6]. It would be useful to study whether promoters can be used to prevent deactivation in hydrated upgrading environments. Second, the work could be applied to whole bio-oils. As described in Chapter 1, there are experimental challenges to studying whole bio-oil upgrading studies that result in model compounds being very attractive for study. However, since this research project was undertaken, there have been advancements in developing and commercializing lab-scale pyrolysis reactors to generate bio-oil vapors. For example, Frontier Lab produces a tandem microreactor (Rx-3050TR) and CDS Analytical makes the CDS 5200 HPR, can send effluent gases directly to a GC-MS [7,8]. The findings of this work could be broadened by studying the effect of promoted Mo₂C catalysts on whole bio-oil vapors instead of just model compounds.

One more area to pursue would be follow up on observed differences between promoted Mo₂C catalysts prepared by wet impregnation versus incipient wetness. Research undertaken in Chapter 5 was inspired by findings in Chapter 2 that suggested Fe promotion of Mo₂C via wet impregnation increased HDO activity. However, Fe/Mo₂C prepared by incipient wetness was found to have very different selectivity. Previous work in our group has compared catalytic performance of wet impregnation on the native versus the passivated Mo₂C [9], but has not directly compared catalysts prepared with wet

impregnation and incipient wetness at similar loadings. Very good dispersion is achieved with wet impregnation that is likely not matched with incipient wetness techniques, and could be the source of the difference [10,11]. Another possible difference is that the promoter metal interacts with the surface differently in wet impregnation versus incipient wetness. X-ray photoelectron spectroscopy (XPS) of the could help elucidate this difference. It would be best to compare the wet impregnation and incipient wetness catalysts before reduction, after reduction, and after passivation

6.3. Research Thrusts in New Areas

A significant barrier to the replacement of gasoline or jet fuel with biofuel as a carbon-reduction strategy is that bio-oil upgrading typically requires the addition of H₂. And currently, commercial biofuel upgrading processes often employ H₂ derived from natural gas because it is much cheaper than sustainably-sourced H₂ [12]. A 2005 report from the National Energy Technology Laboratory applied lifecycle analysis (LCA) to estimate that H₂ produced from liquid natural gas (with carbon capture and sequestration) had a global warming potential of 62.5 CO_{2e}/MJ (32.8 CO_{2e}/MJ) [13]. Replacing H₂ from natural gas with H₂ from sustainable sources is one possible opportunity to reduce the carbon emission from bio-oil upgrading. H₂ can be produced from water electrolysis, or even via steam reforming of pyrolysis bio-oil [14,15]. With an eye toward minimizing the overall carbon emissions from biofuel production, the focus of catalytic upgrading studies should shift focus to methods that minimize or eliminate the consumption of H₂.

One example of an upgrading method that minimizes H₂ consumption is electrocatalytic hydrogenation

6.4. References

- [1] X. Liu, K. J. Smith, Acidity and Deactivation of Mo₂C/HY Catalysts Used for the Hydrogenation and Ring Opening of Naphthalene, *Applied Catalysis A: General* 335 (2008) 230–240. doi:10.1016/j.apcata.2007.11.028.
- [2] V. Schwartz, V. T. da Silva, S. T. Oyama, Push–Pull Mechanism of Hydrodenitrogenation over Carbide and Sulfide Catalysts, *Journal of Molecular Catalysis A: Chemical* 163 (2000) 251–268. doi:10.1016/S1381-1169(00)00390-3.
- [3] L. Óvári, F. Solymosi, Determination of Acidic Centers on Supported Mo₂C Catalysts, *Journal of Molecular Catalysis A: Chemical* 207 (2004) 35–40. doi:10.1016/S1381-1169(03)00469-2.
- [4] M. M. Sullivan, J. T. Held, A. Bhan, Structure and Site Evolution of Molybdenum Carbide Catalysts upon Exposure to Oxygen, *Journal of Catalysis* 326 (2015) 82–91. doi:10.1016/j.jcat.2015.03.011.
- [5] P. M. Mortensen, H. W. P. de Carvalho, J.-D. Grunwaldt, P. A. Jensen, A. D. Jensen, Activity and Stability of Mo₂C/ZrO₂ as Catalyst for Hydrodeoxygenation of Mixtures of Phenol and 1-Octanol, *Journal of Catalysis* 328 (2015) 208–215. doi:10.1016/j.jcat.2015.02.002.
- [6] J. Engelhardt, P. Lyu, P. Nachtigall, F. Schüth, Á. M. García, The Influence of Water on the Performance of Molybdenum Carbide Catalysts in Hydrodeoxygenation Reactions: A Combined Theoretical and Experimental Study, *ChemCatChem* 9 (2017) 1985–1991. doi:10.1002/cctc.201700181.
- [7] Tandem M-Reactor “Rx-3050TR,” *Frontier Lab* (n.d.). http://www.frontier-lab.com/catalog/en/Rx-3050TR_Flier_E.pdf.
- [8] CDS 5200 HPR, *CDS Analytical* (n.d.). <https://www.cdsanalytical.com/pyrolysis-hpr>.
- [9] B. M. Wyvratt, J. R. Gaudet, L. T. Thompson, Effects of Passivation on Synthesis, Structure and Composition of Molybdenum Carbide Supported Platinum Water–Gas Shift Catalysts, *Journal of Catalysis* 330 (2015) 280–287. doi:10.1016/j.jcat.2015.07.023.
- [10] N. M. Schweitzer, J. A. Schaidle, O. K. Ezekoye, X. Pan, S. Linic, L. T. Thompson, High Activity Carbide Supported Catalysts for Water Gas Shift, *Journal of the American Chemical Society* 133 (2011) 2378–2381. doi:10.1021/ja110705a.
- [11] J. A. Schaidle, N. M. Schweitzer, O. T. Ajenifujah, L. T. Thompson, On the Preparation of Molybdenum Carbide-Supported Metal Catalysts, *Journal of Catalysis*

289 (2012) 210–217. doi:10.1016/j.jcat.2012.02.012.

- [12] The Hydrogen Problem, *BiofuelsDigest* (n.d.).
<http://www.biofuelsdigest.com/bdigest/2013/04/02/the-hydrogen-problem/>.
- [13] J. Ruether, M. Ramezan, E. Grol, Life-cycle analysis of greenhouse gas emissions for hydrogen fuel production in the United States from LNG and Coal, National Energy Technology Laboratory, 2005.
- [14] S. Czernik, R. Evans, R. French, Hydrogen from Biomass-Production by Steam Reforming of Biomass Pyrolysis Oil☆, *Catalysis Today* 129 (2007) 265–268.
doi:10.1016/j.cattod.2006.08.071.
- [15] A. Arregi, G. Lopez, M. Amutio, I. Barbarias, J. Bilbao, M. Olazar, Hydrogen Production from Biomass by Continuous Fast Pyrolysis and In-Line Steam Reforming, *RSC Advances* 6 (2016) 25975–25985. doi:10.1039/C6RA01657J.